HOCHSCHULE FRESENIUS
UNIVERSITY OF APPLIED SCIENCES

Department of Chemistry & Biology
Master Bioanalytical Chemistry and Pharmaceutical Analysis
Idstein

Triggered Disassembly of Peptide Nanofibers in Solution and on Surfaces

Approved MASTER THESIS
for the achievement of an academic degree as
Master of Science

Lara Alix Kaczmarek, B. Sc.
born in Frankfurt/Main

Matriculation number: 400051655

1st Reviewer: Prof. Dr. Thorsten Hofe
2nd Reviewer: Prof. Dr. Erwin Metzmann

August 18, 2020

This Thesis was written between 01.02.2020 and 18.08.2020 at the Max Planck Institute for Polymer Research in the group of Prof. Dr. Tanja Weil under supervision of Dr. Christopher Synatschke.

Acknowledgements

I would first like to thank Prof. Dr. Tanja Weil for offering the opportunity to work on this thesis at the Max Planck Institute for Polymer Research. Furthermore I would like to thank Dr. Christopher Synatschke for his continuous feedback and proofreading. I would especially like to thank Adriana Sobota for excellent supervision, frequent advice in discussions, proofreading and for conducting the cell experiments during this work. Furthermore I would like to thank Luisa Wiechmann for recording CD spectra with me, Ali Rouhanipour and Darijan Schüler for the LC-MS measurements and Pia Winterwerber for AFM measurements. I would also like to express my thanks to Christoph Sieber for TEM imaging and Dr. Gönül Kizilsavas for the conducted NMR study. Additionally, I would like to thank Kübra Kaygisiz for provision of a compound as well as her previous work that created a foundation for this work. My sincere thanks goes to the entire research group for a pleasant working atmosphere and immediate help with any kind of issues. Furthermore I would like to thank Prof. Dr. Thorsten Hofe for his suggestions and review of this thesis and would also like to acknowledge Prof. Dr. Erwin Metzmann as the second reviewer. Finally, I would like to thank my family and friends who always have been and always will be there to support me.

Contents

Abbreviations

A549 cells	Adenocarcinomic human alveolar basal epithelial cells
ACN	Acetonitrile
AFM	Atomic force microscopy
ATR	Attenuated total reflexion
Aβ	Amyloid β peptide
CD	Circular dichroism
DCM	Dichloromethane
DIC	*N,N'*-Diisopropylcarbodiimide
DLS	Dynamic light scattering
DMAP	4-(Dimethylamino)pyridine
DMF	*N,N'*-Dimethylformamide
DMSO	Dimethyl sulfoxide
DPBS	Dulbecco's phosphate buffered saline
DPTS	1,4-Dimethylpyridinium *p*-toluenesulfonate
DTT	Dithiothreitol
ECM	Extracellular matrix
ESI-MS	Electrospray ionisation–mass spectrometry
FA	Formic acid
Fmoc	Fluorenylmethyloxycarbonyl
FTIR	Fourier-transform infrared
HIV	Human immunodeficiency virus
HPLC	High performance liquid chromatography
ISA	International Society of Amyloidosis
LC-MS	Liquid chromatography – mass spectrometry
m/z	Mass-to-charge ratio
MALDI-TOF-MS	Matrix-assisted laser desorption ionisation – time of flight mass spectrometry
NMR	Nuclear magnetic resonance
Oxyma	Ethyl cyano(hydroxyimino)acetate
PES	Polyether sulfone
PNF	Peptide nanofiber
PS	Polystyrene
S/N	Signal-to-noise ratio
SAP	Self-assembling peptide
SEM	Scanning electron microscopy
SPPS	Solid phase peptide synthesis
TEM	Transmission electron microscopy
TFA	Trifluoroacetic acid
ThT	Thioflavin T

TIPS	Triisopropyl silane
TLC	Thin layer chromatography

List of Figures

List of Schemes

List of Tables

1 Introduction

Molecular self-assembly is a process ubiquitous in nature. One of the most prominent representatives for higher-order structures are proteins: Various intra- and intermolecular forces are involved in the formation of secondary, tertiary and even quarternary structures. Additionally, they have been found to assemble into a variety of superstructures such as micelles, sheets, tubes or fibers. A lot of naturally occuring structures make use of this variability in the form of stimulus responsiveness or structural stability and mimicking these naturally occuring motifs has been the focus of various scientific tasks in the past. For example, peptides that assemble into nanofibers may create a network resembling the fibrous framework of the extracellular matrix, thus providing artificial scaffolds for cells in e. g. tissue engineering. The advantages of self-assembling peptides in this field include good biocompatibility as well as comparably facile design and tuning of the desired systems on nanoscopic scales. However, translation onto larger length scales still poses various challenges.

This work will focus on such a self-assembling peptide system. More precisely, the degradation of fibrous structures upon a defined trigger will be investigated. In the following, an overview over currently employed systems with respect to the targeted functionalities will be given.

2 Theory

Proteins are biopolymers that can be found everywhere in nature. Based on differences in their amino acid sequence, they appear in various forms and perform a broad diversity of tasks of mechanical, physical or chemical nature. For instance, they may catalise metabolic reactions, transport molecules, or respond to various stimuli in their surrounding environment. Additionally, many proteins self-assemble into mesoscopic higher-order structures like fibrils, e. g. creating networks that provide structural stability to a variety of tissues. A fibrous network of actin for example serves eukariotic cells as major component of the cytoskeleton, while other fibril-forming proteins may serve differing purposes. One of these fibrillar aggregates that has been extensively studied are amyloid fibrils. While they are mostly associated with neurodegenerative diseases like Alzheimer's or Parkinson's diasease, where they appear as insoluble plaques, amyloids exhibit mechanical properties very similar to silk which makes them promising tools for a variety of applications. For instance, they have been used as drug-delivery systems [1], scaffolds in tissue engineering [2] and even in molecular electronics [3].

2.1 Self-assembly

The spontaneous development of highly ordered and stable structures in thermodynamic equilibrium is termed self-assembly. [4] This equilibrium may as well be a metastable state, in which the respective product is kinetically trapped. [5] According to their structural characteristics, proteins and peptides may assemble into a variety of shapes which are stabilised by non-covalent interactions such as hydrogen bonds, hydrophobic interactions and π-π-stacking. Depending on the interactions of their structural monomers, proteins and peptides adopt different highly ordered nanostructures such as spheres, tubes or fibers that may exhibit particular properties in certain environments. [6] However, a distinction should be made between proteins and peptides: While protein monomers may already demonstrate functionality based on their tertiary structure, peptide monomers seldomly form functional structures on their own. The assembly of multiple units (i. e. quarternary structure) into higher-order structures is usually required for peptides to exhibit e. g. structural stability.

The foundation of such nanostructures are e. g. typical secondary structures like α-helices and β-sheets which are as well stabilised by non-colavent interactions. The naturally occuring amino acids can be grouped according to their physicochemical properties which in turn influence their form of interaction. Acidic (e. g. aspartic acid) or basic (e. g. lysine) monomers can induce electrostatic interactions, non-polar (e. g. alanine) or aromatic (e. g. phenylalanine) side-chains promote hydrophobic effects and polar residues (e. g. glutamine) favour hydrogen bonding. Conformationally constrained (proline) or flexible (glycine) amino acids may induce turns in the primary structure, resulting in β-hairpin or helical structures (see Table 1). [6] However, not only the residues themselves but also their order (i. e. the primary structure) influences the overall conformation. For example, the number of residues per α-helical turn is typically 3.6. Thus, occurence of similar amino acids every three or four residues provides stability for such structures. Another example are β-sheet structures: The

general β-sheet structure (whether parallel or antiparallel) is stabilised by hydrogen bonds between the amide bonds in the peptide's backbone. The residual groups of the amino acids extend from the backbone in alternating directions. [7] Therefore, sequences that alternate polar and non-polar residues have been found to promote formation of higher-order structures like nanofibers. [8]

Table 1: Side-chain interactions of amino acids [6]

Form of Interaction	Dependence	Strength	Amino Acids
Electrostatic	pH Ionic Strength	0.5-4 kJ/mol per bond	Aspartic Acid Glutamic Acid Histidine Lysine Arginine Serine, Threonine (de-/phosphorylation)
Hydrogen Bonding	Solvent Temperature	4-12 kJ/mol per bond	Serine Threonine Asparagine Glutamine
Hydrophobic Effects	Solvent Ionic Strength Temperature	4-8 kJ/mol per residue	Alanine Valine Leucine Isoleucine Methionine Phenylalanine Tyrosine Tryptophane
Strand Direction	Electrochemical (Disulfide Bridge) Temperature	- -	Cysteine Proline Glycine

2.1.1 Amyloid Nanofibrils

Nanofibrils may form from a variety of naturally occuring and synthetic proteins and peptides. They are defined by their morphology and mechanical characteristics rather than distinct amino acid sequences. Fibrils, as is the case for all ordered nanostructures, pose an energetically favourable state for the peptide or protein compared to the unfolded state; stabilisation *via* non-covalent interactions is involved in the formation and retention of these states. Formation of amyloid fibrils occurs from unstructured precursors in a first nucleation phase and a following elongation phase. In nature, misfolded monomers aggregate to form oligomers which are further on associated into higher-order protofibrils. These may intertwine to create stable and unsoluble fibrils (see Figure 1). [9] While the underlying non-covalent interactions may not exhibit strong binding energies on their own (see Table 1), collectively they can form a stable aggregate with remarkable robustness towards physical forces, changes in temperature, or denaturing agents. [3]

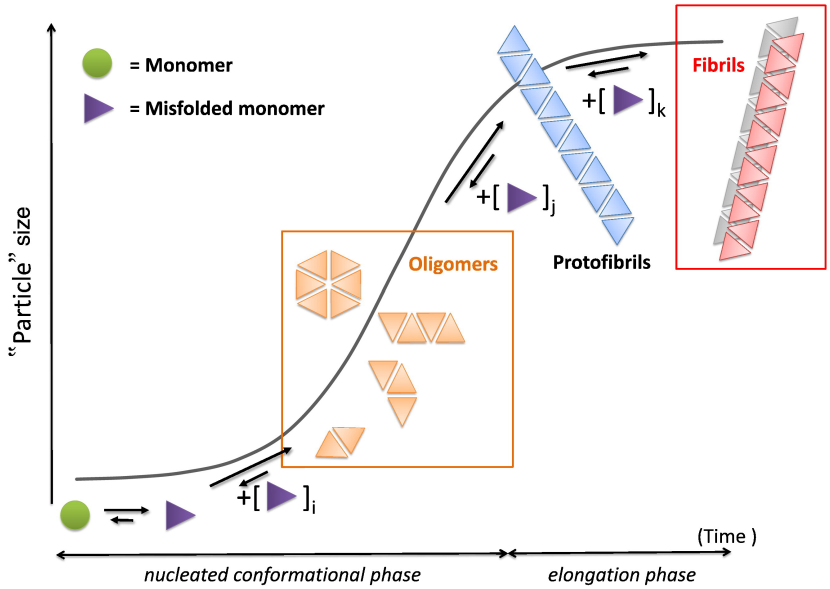

Figure 1: Schematic representation of fibril formation. Figure reprinted from a publication by Sarroukh *et al.* [9]

Per definition by the International Society of Amyloidosis (ISA) in 2014, amyloid fibrils are characterised by three main properties: (1) the formation of insoluble fibrils that are mainly deposited in extracellular matrices (ECMs) and tissues; (2) occurence as non-branching fibrils that interact with Congo red dye to exhibit green, yellow or orange birefringence; and (3) an observable cross-β-diffraction pattern in X-ray diffraction analysis. Additionally, only proteins characterised unambiguously by protein sequence analysis can be included in the official ISA Amyloid Fibril Protein Nomenclature List. [10]

A structural trait shared among amyloid nanofibers is a secondary structure rich in β-sheets. More precisely, a so-called cross-β structure is formed upon polymerisation. In this structural pattern, the β-strands form stacks with a 4.8 Å spacing running perpendicularly to the fibril axis. Research has shown that especially amphiphilic sequences alternating between hydrophilic and hydrophobic residues are prone to fibrillation [11, 12]. Herein, the side-chains of two such stacks interdigitate with a spacing of 9 Å–11 Å to create a dry interface between the sheets and a wet interface to the outside of the protofibril in aqueous solution (see Figure 2). This characteristic is termed *steric zipper*. [13, 14] Furthermore, two or more of these protofibrils may twist around each other to form mature amyloid nanofibers. Depending on the protein or peptide, these fibrils show a periodical twist that can be observed in electron microscopy. [15] While antiparallel β-sheet core structures seem to be the thermodynamically favoured constitution in the cross β amyloid motif, investigations by Zanjani *et al.* revealed that in fibers of small peptides (e. g. six residues) at long length scales parallel structures may dominate. They hypothesised that at short length scales (protofibrils) the more optimal hydrogen bonding pattern in antiparallel sheets renders them the preferred orientation while for long scales (mature fibrils) the smoother side surface of parallel sheets may promote a more favourable orientation for steric zipper formation by the side-chains. [16] A similar shift from antiparallel to parallel orientation has already been investigated by Cerf *et al.* . [17]

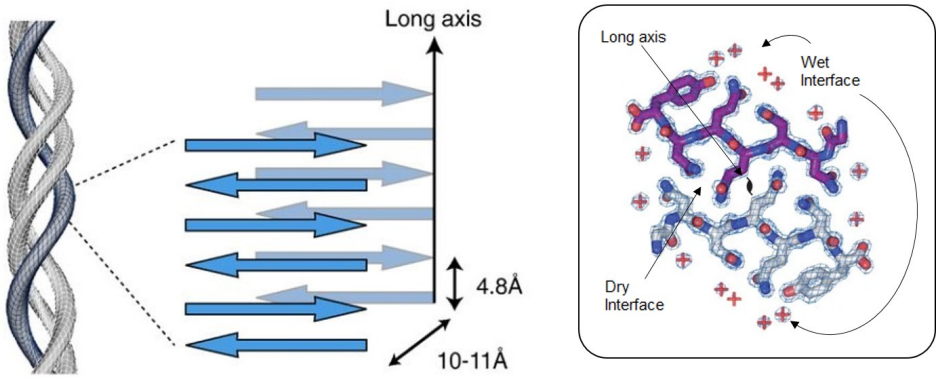

Figure 2: Exemplary cross-β-structure of amyloid fibrils (left) and steric zipper of peptide sequence GNNQQNY (right). Figures adapted from publications by Biancalana *et al.* [18] and Nelson *et al.* [13].

2.2 Mimicking Existing Structures with Peptides as a Simpler Model

As already stated in the beginning of this chapter, proteins and peptides may also react to changes in their environment. One of these environments may be the ECM, where a variety of proteins and polysaccharides excreted by the surrounding cells create a complex communication network. The ECM is highly tissue-specific and may change its composition upon physical or chemical damage to promote healing processes by stimulus-responsive proteins. The importance and uniqueness of this matrix is demonstrated even more when defective alterations due to a variety of diaseases occur. For example, a misfolding of amyloid β peptide (Aβ) into fibrous structures is associated with Alzheimer's Disease. However, fibrous structures are not necessarily linked to defects but may provide structural stability, making research on these matrices important not only for diseases but other medical applications like tissue engineering or drug delivery. [19]

Due to the complexity of living tissues the development of ECM-mimicking materials that stimulate host cells to initiate repair mechanisms is a more facile approach than to recreate such tissues. However, it is not precisely known which structural or biochemical informations in the ECM trigger certain functions. Thus, ECM-mimicking materials with known structures and characteristics, such as peptides, are designed to shed light on these dependencies.

Since the self-assembly is influenced by certain amino acid patterns, synthetic peptide sequences can be engineered to mimick structures already existent in nature in a more facile way. For example, peptide nanofibers (PNFs) can mimick the ECM by formation of networks to serve as artificial scaffolds that promote cellular adhesion and growth while being biologically degradable. [20] In the group of Prof. Dr. Tanja Weil a library of self-assembling peptides (SAPs) based on the naturally occuring sequence QCKIKQIINMWQ from the glycoprotein $GP120_{417\text{-}428}$ of human immunodeficiency virus (HIV) has been characterised regarding their ability to stimulate adhesion and growth of peripheral neuronal cells in mice. Glycoprotein $GP120_{417\text{-}428}$ of HIV produces fibrils that are known to enhance cellular uptake of virions. [21] Their study found a correlation between the induced neuronal activity and the tendency to form fibers based on alternating patterns of hydrophobic and positively charged side-chains. Due to this pattern, the peptides have an overall positive net charge, which in turn facilitates interaction with negatively charged cell membranes. Additionaly, a higher intermolecular

β-sheet content and larger cross-sectional diameter in atomic force microscopy (AFM) analysis of single fibers was observed for highly active peptides. [12] One of these SAPs with both a high conversion rate to PNFs (95 % after 24 h incubation in Dulbecco's phosphate buffered saline (DPBS)) and a strong neurite growth activity is the 7-mer peptide **CKFKFQF**. It consists of a sequence with alternating polarities, thus promoting fibrillation (see Figure 3).

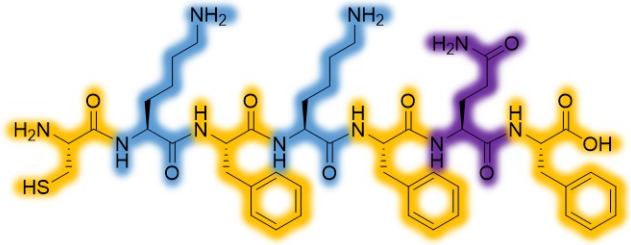

Figure 3: Side-chain polarities of CKFKFQF. Yellow: hydrophobic, violet: hydrophilic, blue: positively charged at neutral pH.

2.3 Stimulusresponsive Peptides

As already stated above, the natural ECM is a dynamic network of various compounds creating a vast amount of differing stimuli. A simple peptide system such as an amyloidic fibril network on the other hand, is rather static. Control over an artificial system in the form of trigger-responsiveness, especially the triggered degradation of scaffolds, would therefore pose a useful tool for various applications.

Peptides have been designed to respond to a variety of different stimuli, including temperature [22], pH [23, 24], electrochemical potential [25], enzymatic activity [26] and photoirradiation [27]. However, especially in the biological or medicinal field, where living organisms are employed in experiments, constant conditions within a defined range regarding pH, temperature, or salt concentration are crucial. Thus, photoirradiation or the use of enzymes as triggers are among the least invasive methods. While the use of enzymes may be complicated by methods of application, light is an easily accessible stimulus. With regard to possible medical applications, light can penetrate tissue up to a wavelength-dependent depth (e. g. UV (350 nm): 0.5 mm, red (650 nm): 6 mm). [28] While higher wavelengths can penetrate deeper into tissue, not many concepts employ compounds that are labile in the visible spectrum. Synthesis of such compounds may be increasingly complicated due to constantly required shielding from light. Furthermore, in many cases such systems are also thermally labile. Therefore, photolability in the UV range is a much more commonly used tool to trigger certain effects. However, a disadvantage of the UV range is its cytotoxicity.

Previous work in the group of Prof. Dr. Weil by Pieszka *et al.* included a redox-sensitive peptide. The sequence KIKISQINM, which is known to form fibrilar nanostructures in aqueous solution, was modified to incorporate an ester bond at the serine moiety. The serine's free amine group was protected by a boronic acid carbamate group. This ester bond in the backbone caused a kink in the threedimensional structure which in turn hindered the formation of ordered cross-β-sheets and fibrillation. Upon hydrolysis of the carbamate an *O*,*N*-acyl shift causes linearisation of the backbone and nanofibrils can form. Subsequent disassembly was observed upon oxidation of methionine with

H_2O_2. [23] Further work on the same peptide sequence included a photocleavable cageing group to replace the boronic acid carbamate group. Linearisation and subsequent fibrillation of the sequence upon exposure to UV light was confirmed in this case as well. [29]
Diving further into photochemistry, another sequence known to form PNFs in aqueous media established among the group (CKFKFQF) was equipped with a photocleavable linker in varying positions by Kübra Kaygisiz. Additionally, the biologically active sequence RGD was incorporated to promote cellular interaction and binding. [30]

A class of photocleavable linkers that has been thoroughly studied are nitrobenzyl-based compounds. During this work, such a compound was used to induce fibril decomposition upon exposure to UV-light (365 nm). The linker **PCL-VII** (see Scheme 1) has previously been synthesised and used in peptide synthesis by Sur *et al.* . [31] The cleavage follows the Norrish type-II mechanism which will be described in more detail in the following.

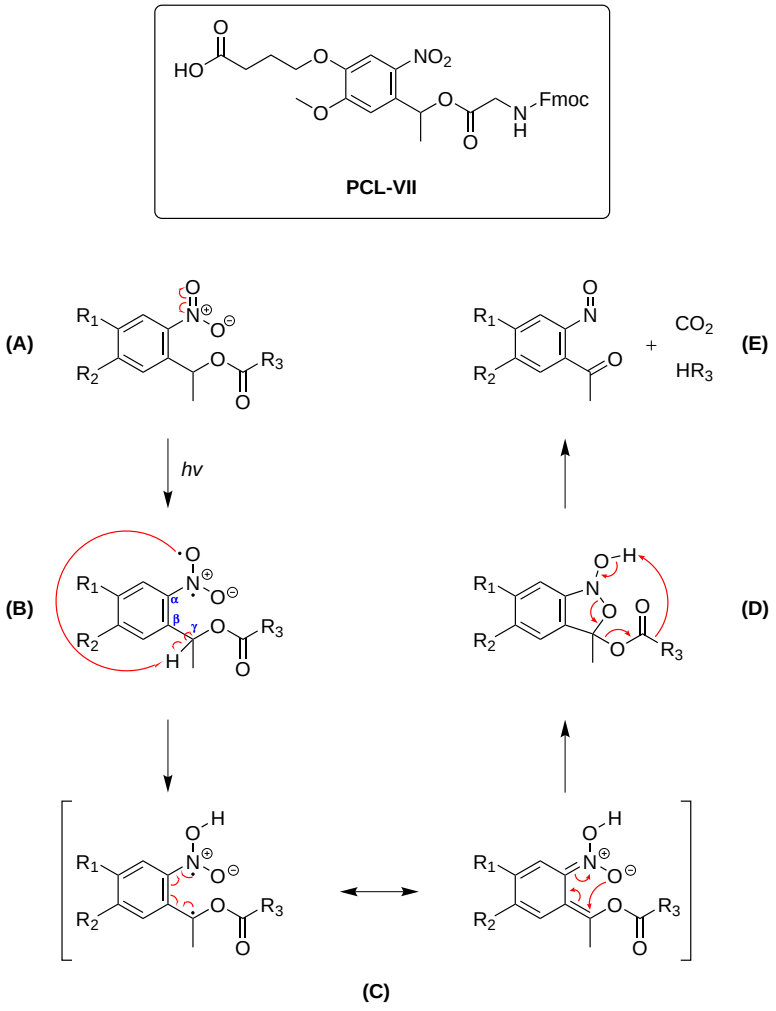

Scheme 1: Proposed Norrish type II reaction mechanism for the cleavage of a photolabile peptide [32]

Scheme 1 illustrates the cleavage mechanism of the nitrobenzyl photolinker. Upon excitation with UV-light a double bond in the nitro group is split homolytically to produce biradical species **A**. Abstraction of a γ-hydrogen by the electron-deficient oxygen creates 1,4-biradical intermediate **B** which will undergo intramolecular electron migration (**C**) to form an *aci*-nitro intermediate. Depending on

substitution, solvent and pH, the decay rate of this intermediate may vary. The following irreversible cyclisation to produce five-membered ring intermediate **D** will lead to release of the ligand R_3 in the last step. 2-Nitrosobenzaldehyde **E** and CO_2 are produced as side products. [32, 33]

Photocleavable linker **PCL-VII** was incorporated in the PNF-generating peptide sequence CKFK-FQF. Upon photoirradiation, CKFK-PCL-FQF produces fragments CKFKG and PCL*-FQF as outlined in Scheme 2. Further degradation of the cleavage products may occur. Barth *et al.* found

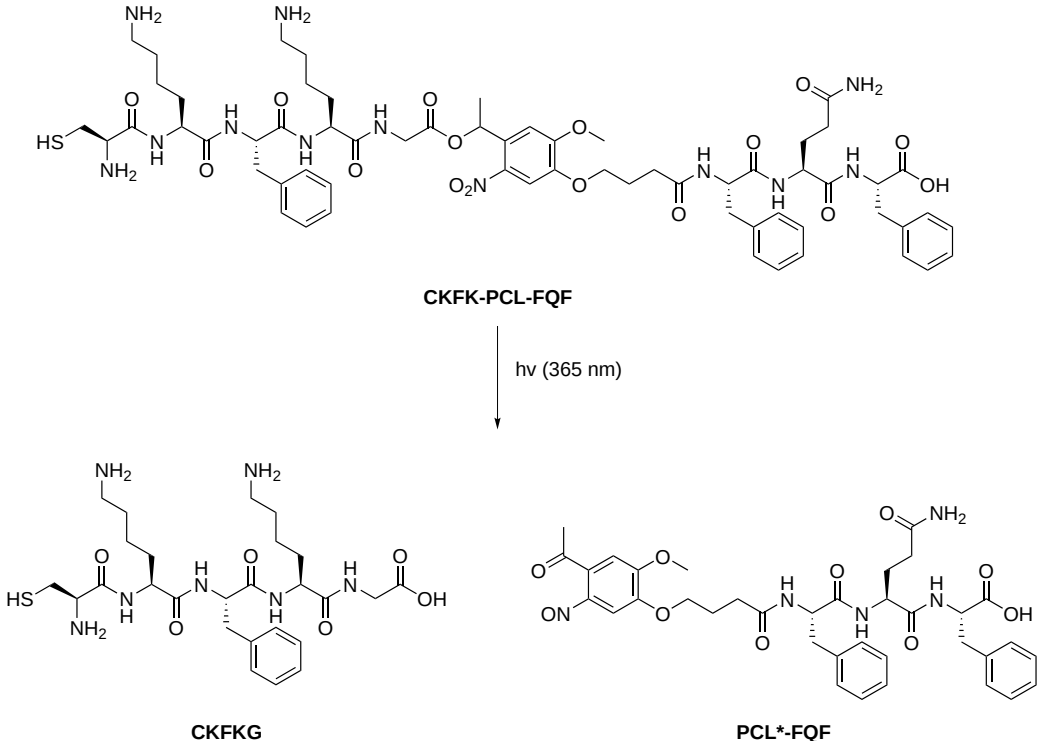

Scheme 2: Intact photolabile peptide CKFK-PCL-FQF and fragments produced upon photocleavage

that Norrish Type II nitroso products can undergo further reaction with thiol groups as outlined in Scheme 3. [34]

2.4 Analysis Methods

General functionalities as well as expected signals for the used analysis methods will be shortly summarised in the following.

2.4.1 ThT Assay

Thioflavin T (ThT) (see Figure 4) is a fluorescent dye used in the detection of amyloid fibrils. Normally, when excited at 336 nm, the dye shows only weak fluorescence. Upon binding to amyloid fibrils, intermolecular interactions cause a red shift of excitation (approx. 450 nm) and emission (approx. 482 nm) maxima with high intensity. [35] It is assumed that this shift is caused by the immobilisation of the C-C bond rotation between the aniline and benzothiazole rings. [36] The energy barrier for the rotation around this bond is not very high, thus providing a rapid way of emission-free

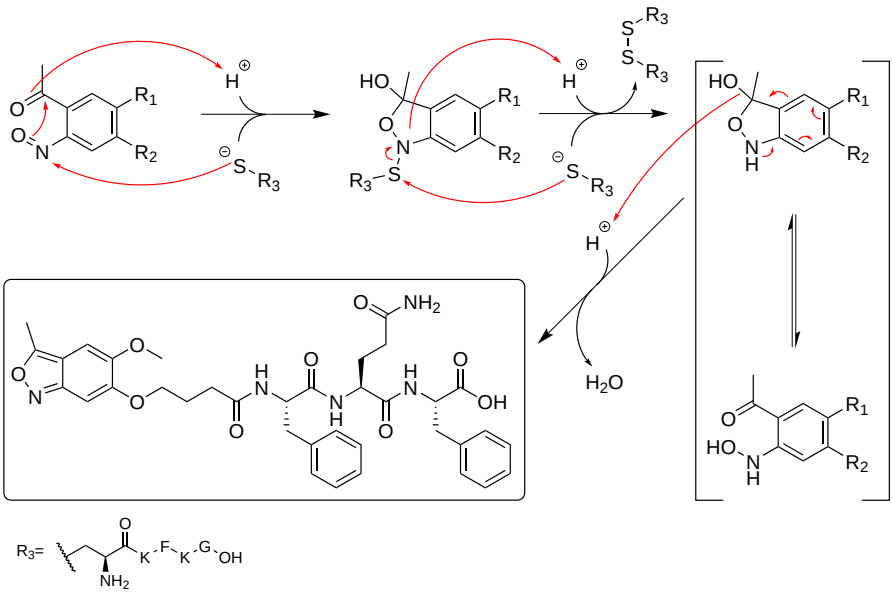

Scheme 3: Side-reaction of nitroso compounds with thiols as described by Barth *et al.* adapted for cleavage fragments PCL*-FQF and CKFKG. [34]

relaxation. Immobilisation of this bond results in a longer halflife of the excited state, resulting in a higher quantum yield for fluorescence. [37]

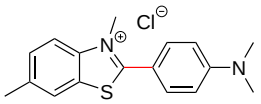

Thioflavin T (ThT)

Figure 4: Structure of Thioflavin T (4-(3,6-dimethyl-1,3-benzothiazol-3-ium-2-yl)-*N,N*-dimethylaniline chloride). The immobilised bond during amyloid intercalation ist highlighted in red.

ThT binds to various amyloidic sequences which all share the typical cross-β-sheet structure. It is therefore assumed that ThT interacts with this type of structure. In these cross-β-sheet arrangements, amino acid chains align in a way that creates grooves between the surface side chains that run parallel to the fibril axis (see Figure 5). [13] Krebs et al. [38] were able to determine the orientation of the dye relative to the fibril axis by confocal microscopy using polarised light. According to their research, ThT most likely intercalates with its long axis parallel to the fibril axis in between the side chain residues, as illustrated in Figure 5. Computational simulations of ThT-binding to fibrils of A$\beta_{16\text{-}22}$ peptide conducted by Wu *et al.* [39] strongly supported these assumptions. Their research revealed two preferred binding sites, the side chain grooves being the more abundant one compared to the second at the steric zippers at the ends of the β-sheets. Furthermore, their computations indicated a binding preference towards channels created by aromatic residues. By incubation of a sample containing preformed amyloid fibrils in a ThT solution, the dye should intercalate in the fibers and create the characteristic fluorescence.

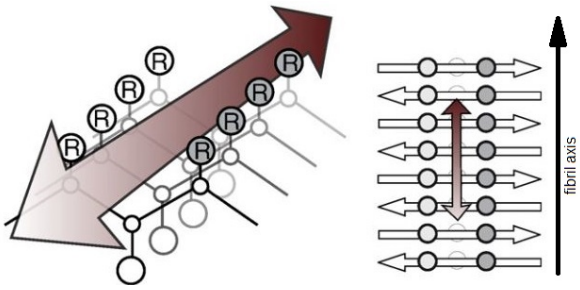

Figure 5: ThT intercalation into grooves created by side-chain orientation. Figure reprinted from a publication by Biancalana *et al.* and edited. [18]

2.4.2 CD Spectroscopy

In circular dichroism (CD) spectroscopy, circular polarised light is passed through a sample. Depending on its chirality, the sample may absorb differing wavelengths of the incoming left or right hand polarised light to different extents. For two enantiomers of the same molecule the resulting spectra are mirrored, while more complex molecules such as peptides even allow for determination of secondary structures in far-UV wavelengths (170 nm–250 nm). Especially changes in secondary structures depending on e. g. time or temperature can easily be observed, providing thermodynamic information on a system. The most significant signals in the far-UV range are produced by α-helical structures, while β-sheets produce less distinct signals. Typical spectra for pure α-helical, β-sheet and random coil conformation are shown in Figure 6. Spectra can be deconvulated by programs to calculate the relative content of secondary structures. Additionally, near-UV measurements can be used to gain insight on tertiary structures of proteins based on environments of aromatic side-chains. [40]

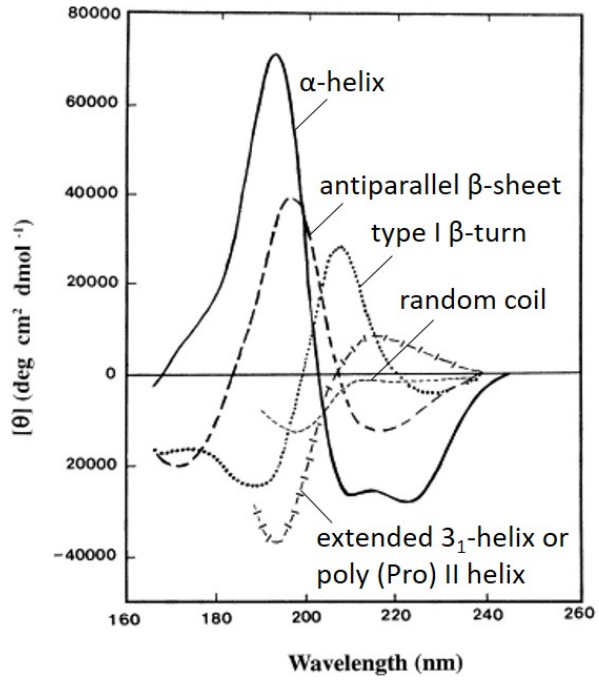

Figure 6: Typical CD spectra for various forms of secondary structures. Reprinted from a publication by Kelly *et al.* and edited. [40]

2.4.3 ATR FT-IR Spectroscopy

Fourier-transform infrared (FTIR) represents a useful tool for analysis of secondary structures of proteins and peptides. Measurements using an attenuated total reflexion (ATR) crystal are based on total reflection of an incoming electromagnetic wave and its displacement at the interface between the crystal and the sample. The incoming waves only penetrate the sample up to a few micrometers, making layer thickness irrelevant for this type of measurement. Additinoally, little to no sample preparation is required for the measurements. However, inhomogenous coverage of the crystal e. g. caused by irregularly shaped sample crystals or contaminations can influence the spectra. [41]
Signals in the amide I region (1600 cm^{-1}–1700 cm^{-1}) show mainly contributions from the C=O stretching of the peptide bond and is therefore directly related to the conformation of the backbone. [42] Here, β-sheet contribution shows the highest absorption coefficients compared to other secondary structures, making FTIR an ideal tool for the analysis of structures rich in β-sheet content, such as amyloids. Typically, the amyloidic cross-β-sheet conformation shows a strong, narrow absorption band in the region of 1611 cm^{-1}–1630 cm^{-1}. Native proteins on the other hand show broader β-signals at slightly higher wavenumbers (1630 cm^{-1}–1643 cm^{-1}), based on differing sheet and strand lengths as well as planarity of the sheets. [9] Additionally, in amyloid fibers, the twist of β-sheets (i. e. the twist of the produced fibers) correlates with location of the maxima in the amide I region: larger twist angles produce maxima at higher wavenumbers and *vice versa*. [43] Furthermore, antiparallel and parallel β-sheets may be distinguished by an additional high frequency band at around 1690 cm^{-1} for antiparallel alignment. [44] For example, Aβ1–42 oligomers exhibit a low frequency band at 1626 cm^{-1} and a high frequency band at 1695 cm^{-1}, indicating antiparallel alignment during the nucleation phase. Aβ1–42 fibrils on the other hand show a low frequency band at 1630 cm^{-1} and no high frequency band, indicating a parallel core structure dominating the elongation. [17] Figure 7 shows ATR-FTIR spectra of Aβ1–42 in antiparallel (oligomers) and parallel (fibrils) conformation with characteristic peaks in the amide I region. For α-helical structures, maxima are typically located at 1650 cm^{-1}–1660 cm^{-1} [42], which might as well present a β-turn structure for proteins. [9]
The amide II region (1500 cm^{-1}–1600 cm^{-1}) is dominated by N–H in-plane bending and C–N stretching vibration for secondary amides. For β-sheets, typical maxima appear at 1520 cm^{-1}–1525 cm^{-1}, while α-helical forms are located at higher wavenumbers (1540 cm^{-1}–1550 cm^{-1}). [42]

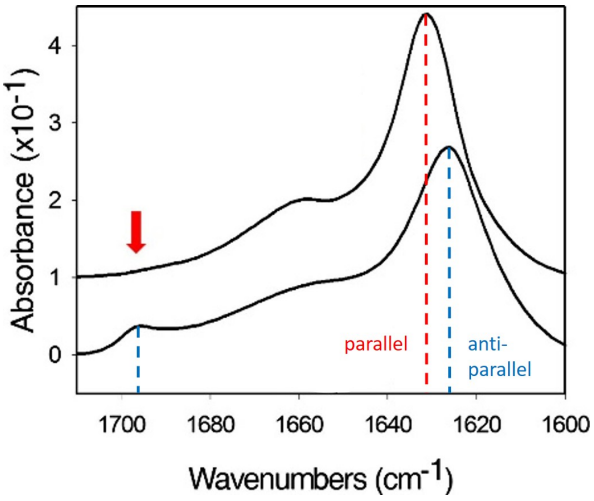

Figure 7: ATR-FTIR spectra of Aβ1–42 in antiparallel (oligomers) and parallel (fibrils) conformation with characteristic peaks in the amide I region. Figure reprinted from a publication by Sarroukh *et al.* and edited. [9]

2.4.4 Transmission Electron Microscopy

When an electron hits an object, e. g. a sample, a variety of events can happen, some of which are illustrated in Figure 8. The electron can for example be deflected, absorbed or pass through. In transmission electron microscopy (TEM) the forward scattered electrons passing through the sample are used for imaging which is why respective samples have to be very thin, ideally only one layer of atoms. The information for imaging is gained from inelasticly scattered electrons and can be displayed as image or diffraction pattern depending on adjustment of the optical aperture. In high vacuum, electrons are emitted from a tungsten filament and guided towards a condenser lens system. These lenses direct the electron beam to create uniform density and energy distribution within the beam as it hits the specimen. Electrons passing through the specimen undergo diffraction and/or scattering events and are subsequently focused onto an imaging plate creating fluorescence or phosphorescence upon impact (see Figure 9). Based on the impact pattern on the screen behind the specimen, a contrast image is produced that represents density differences. Even chemical compositions can be derived from observed scattering patterns since heavier atoms cause stronger electron scattering. [45, 46]

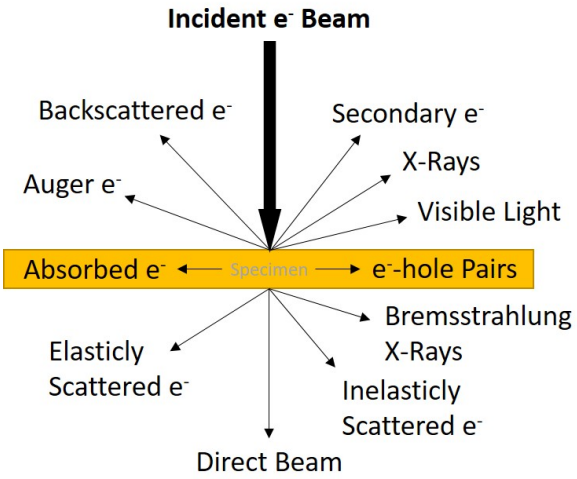

Figure 8: Possible events when an electron beam hits a sample. Recreated from *Transmission Electron Microscopy* by Williams and Carter. [45]

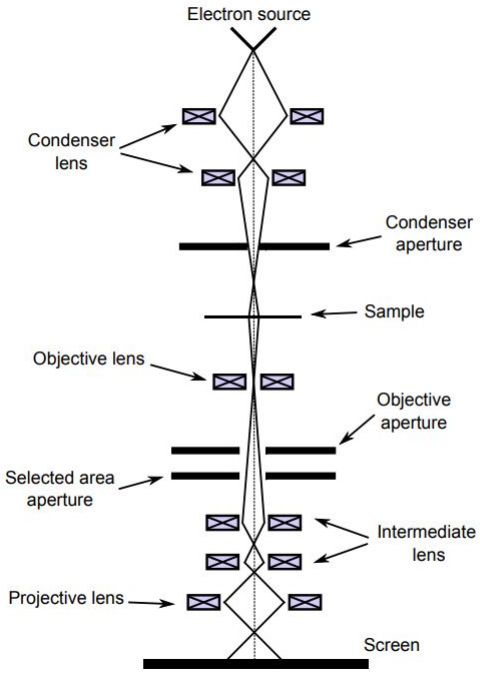

Figure 9: General setup of a transmission electron microscope. Figure reprinted from dissertation of N. Marturi. [46]

2.4.5 Atomic Force Microscopy

In AFM, surfaces are sampled mechanically with a needle attached to a cantilever to obtain the surface profile. The displacement of the cantilever caused by atomic forces during scanning is monitored by a photodiode measuring the light reflected on the cantilever (see Figure 10). No current is applied between needle and surface, which allows for measurements of non-conducting samples. The device may be operated in different modes depending on nature of the sample and the desired information. In contact mode the needle is in direct contact with the surface, which might damage sample and/or needle and is mostly used for smooth and hard surfaces. Repulsive forces between

needle and sample cause displacement of the cantilever. A feedback loop constantly adjusts the z-position of the cantilever according to surface topology. In contactless mode, the cantilever is oscillated by an external force. Depending on attractive forces, the resonance frequency of the cantilever and therefore its oscillation changes, providing information on the surface profile. This mode provides the highest resolution in vacuum up to single atoms and molecules and preserves sample and needle. Intermittent mode is another dynamic measurement mode. Here, the cantilever is oscillated at a fixed frequency close to the resonance frequency and touches the sample at maximum oscillation.[47]

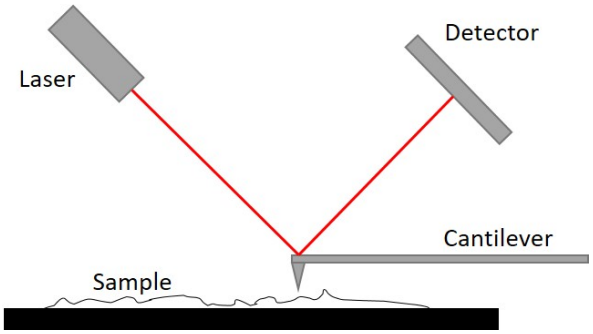

Figure 10: Schematic measurement setup of an atomic force microscope

2.5 Aim and Outline of the Project

As previously determined, peptides show great potential for applications where substitutes of naturally occuring structures are required. Fibrous nanostructures may mimick the ECM in such fashion, that its inherent ability to guide cellular growth can be copied. Moreover, control over assembly and disassembly of such artificial scaffolds may aid in manipulation of cells e. g. for tissue engineering. While assembly of nanostructures has been extensively studied, e. g. by depsipeptide switches, not many concepts on triggered degradation exist. Thus, this work will focus on the triggered disassembly of already formed fibrils in aqueous media. Modified CKFKFQF sequences containing a photosensitive linker will be investigated with regard to the stability of their nanofibers in solution and on surfaces as outlined in Figure 11. The respective parameters and materials will be characterised. Further work may include the alignment of peptide nanofibers in such systems using external stimuli and their potential to direct cellular growth along the fibers.

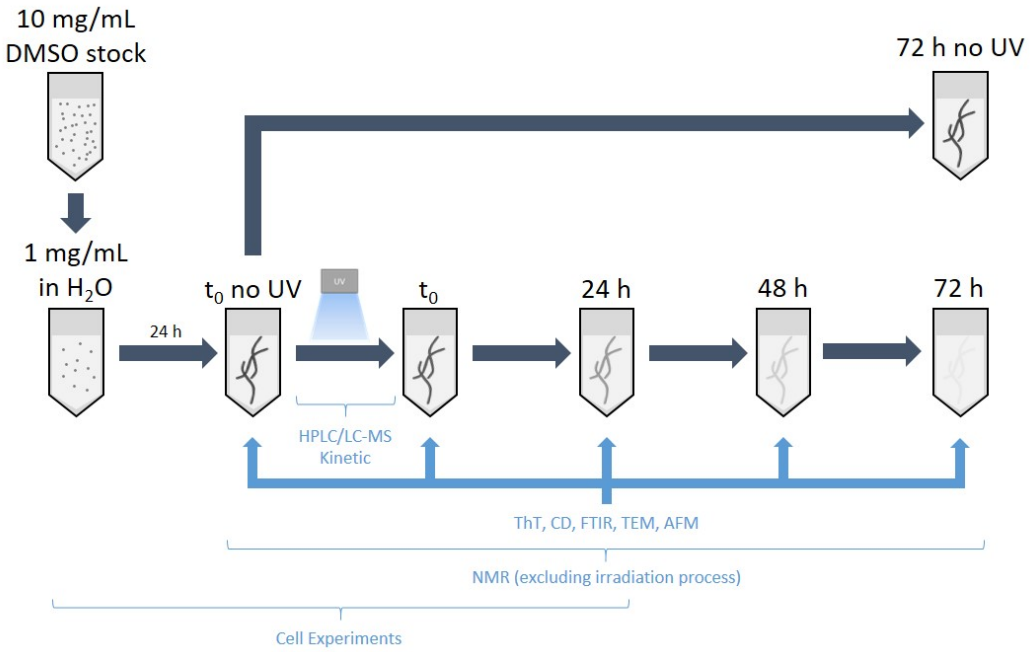

Figure 11: General setup of the morphology studies and observed ranges and measuring points of the methods used

2.5.1 Materials

The materials needed for this work include a modified CKFKFQF sequence, as already mentioned above. Based on the already established synthesis and fibrillation behaviour during previous work by Kübra Kaygisiz, a photosensitive peptide (CKFK-PCL-FQF, Figure 12) will be used for the study. Due to its commercial availability and abundance among other work in the group, the native CKFKFQF (see Figure 12) will be used as control peptide. Fibrillation of the peptides will be conducted as already established among the group (see subsection 4.2.1).

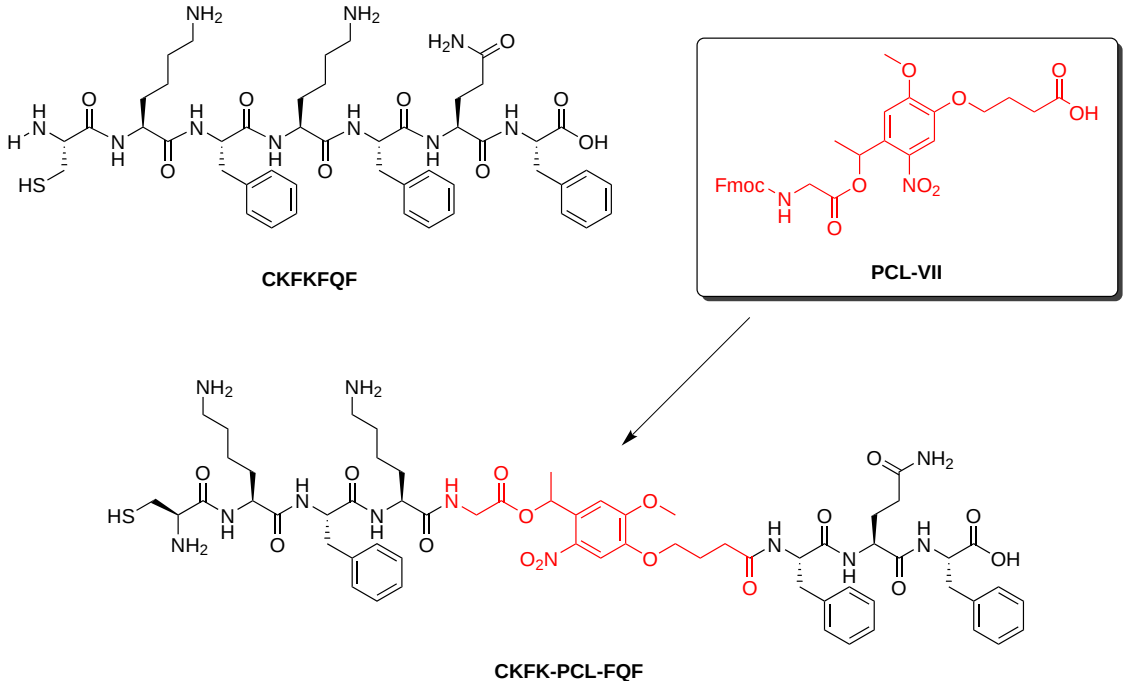

Figure 12: Native CKFKFQF, photocleavable peptide CKFK-PCL-FQF and photolabile linker PCL-VII. The linker was prepared according to a procedure by Sur *et al.* and used in peptide synthesis.

The photosensitive linker will be prepared according to a publication by Sur *et al.* [31] (see Scheme 4). Synthesis of the photolabile peptide will be conducted in 3 steps: 1) synthesis of FQF in the automated peptide synthesiser, 2) coupling of PCL-VII to FQF (on resin), 3) coupling and synthesis of CKFK to PCL-FQF in the automated peptide synthesiser.

2.5.2 Disassembly as Desired Outcome

So far, the UV-induced de-fibrillation behaviour of CKFK-PCL-FQF has only been analysed in organic solvents. Previous work has shown that, as opposed to the intact peptide, the fragments produced via photocleavage are not capable of forming fibrils in organic media [30]. To study interactions with cells, aqueous media are required, which is why water was chosen as the solvent during this work. Additionally, even though no new fibrils can be built, pre-formed fibrils may be kinetically trapped and stay intact even after irradiation. Alternatively, the fibrils will decompose on an unknown time scale in which case temperature treatment may aid in increasing mobility of the fragments thus causing the fibril to disintegrate (see Figure 19). This change in morphology will be evaluated by ThT assays, FTIR, CD and nuclear magnetic resonance (NMR) spectroscopy and TEM and AFM imaging.

The following step after analysis of the system in aqueous solution will be to investigate its behaviour after non-covalent attachment to surfaces (e. g. agarose-coated slides). Again, the question to be answered will be whether the fibrous nanostructures will break apart upon exposure to light, or if stabilising forces can aid in keeping the structure intact. In this case, the movement of the nanostructures might be too restricted by the surface scaffold compared to solution experiments to promote dissociation of the fibrils. Coating of the surfaces with the peptide fibrils will be conducted *via* spray coating. Additional cell attachment studies will determine whether CKFK-PCL-FQF and its

fragments provide suitable attachment points for cells. An additional toxicity test will give first hints on the suitability of the peptide for biologically relevant applications.

3 Results and Discussion

3.1 Synthesis of Photocleavable Linker PCL-VII

The photocleavable linker **PCL-VII** was synthesised following a procedure by Sur *et al.* [31] (see Scheme 4). In the first step, acetovanillone was etherified with ethyl 4-bromobutyrate in a Williamson ether synthesis reaction to produce ether **PCL-I**. The reaction follows a nucleophilic substitution mechanism and may compete with elimination reactions. **PCL-II** was reacted with *in situ* generated acetyl nitrate for nitration following an electrophilic substitution mechanism. Depending on guiding effects of substitutents on the aromatic ring, the nitro group may be located differently or multiple nitrated products may be possible, thus producing lower reaction yields for the desired constitution. Compared to the literature procedure (4 min), a significantly increased reaction time (30 min) was needed for full conversion of the starting material. Due to long storage times after the date of opening, this was attributed to the chemicals used and their probably increased water content. Ester hydrolysis in basic conditions was used to deprotect the carboxylic acid located on the aliphatic side-chain (**PCL-III**). Subsequent protection of the carboxylic acid with base-stable di-*tert*-butyl dicarbonate (**PCL-IV**) was necessary before reduction of the ketone (**PCL-V**) to prevent undesired side-reactions. Alcohol **PCL-V** was then reacted with Fmoc-protected glycine to obtain ester **PCL-VI**. The significantly lowered yield in this step (32 %) when compared to the literature (82 %) might have been a result of the use of 4-(dimethylamino)pyridine (DMAP) instead of 1,4-Dimethylpyridinium *p*-toluenesulfonate (DPTS) as well as the conducted column chromatography. In the literature procedure, the product was only purified by a silica plug. Since thin layer chromatography (TLC) of the synthesised product showed multiple impurities and **PCL-VI** was expected to be more facilely purified on normal phase chromatography than **PCL-VII** with its free carboxylic acid, further purification was conducted in this step. Lastly, deprotection of the carboxylic acid on the aliphatic side-chain was conducted with trifluoroacetic acid (TFA) to obtain **PCL-VII** in 13 % yield over the entire procedure.

Figure 13 shows the NMR spectrum of **PCL-VII** with assignment of the peaks. The spectrum agreed with literature values, though small impurities were still detected, but deemed irrelevant for use in peptide synthesis. Additionally, multiplicities of the peaks differed from literature (multiplets instead of triplets or quartets) most likely due to decreased resolution at 300 MHz compared to the literature spectra (500 MHz). Liquid chromatography – mass spectrometry (LC-MS) analysis was used to further determine purity of the compound (see Figure 14). Product **PCL-VII** eluted after a retention time of 7.66 min as well as slight impurities already observed in NMR analysis. In positive mode, the Na^+ and $NH_4{}^+$ adducts were detected. The deprotonated dimer was observed in negative ionisation mode.

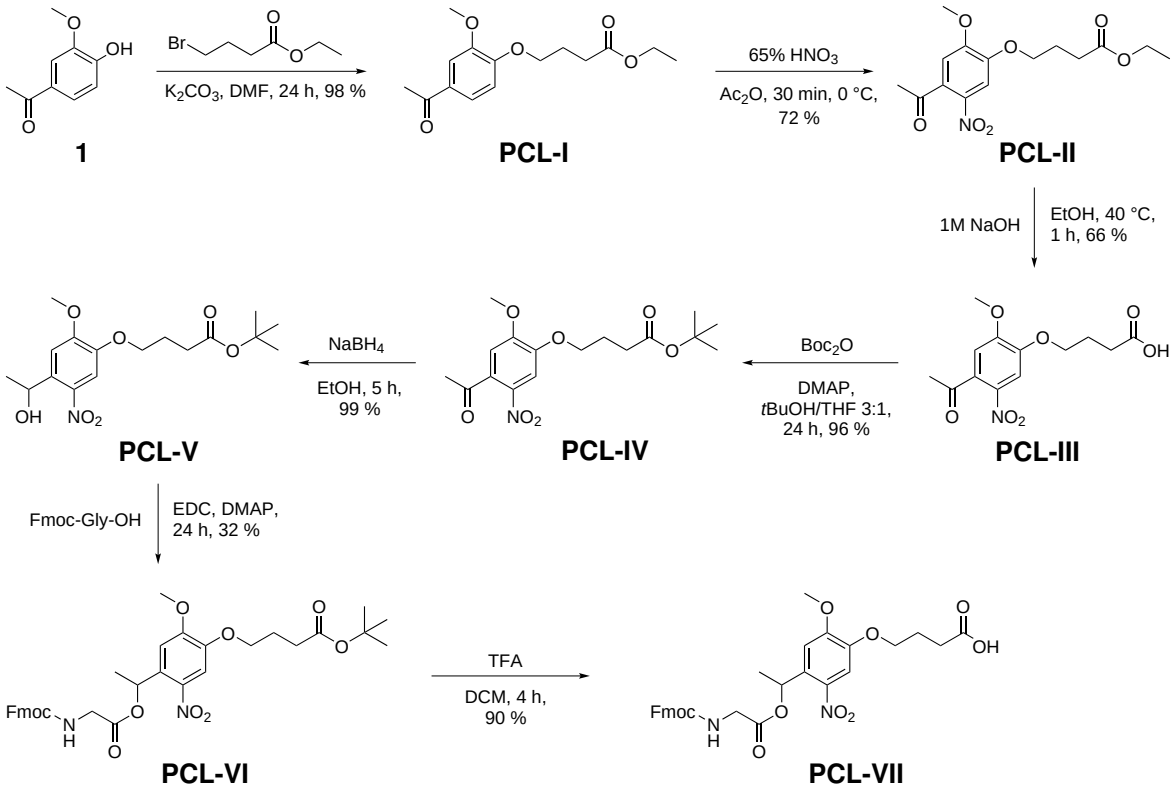

Scheme 4: Synthesis of photolabile linker PCL-VII following a procedure by Sur et. al [31]

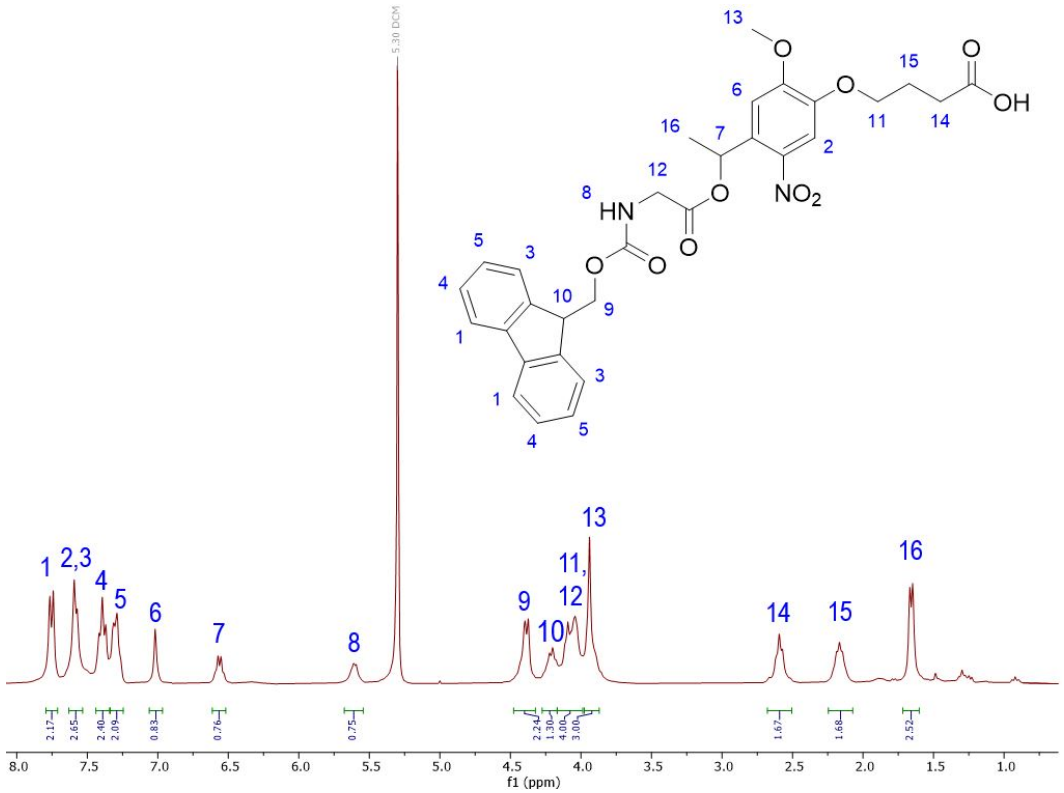

Figure 13: ^{1}H-NMR of **PCL-VII** (300 MHz, $CDCl_3$): δ 7.75 (d, J=7.3 Hz, 2H), 7.63–7.53 (m, 3H), 7.39 (t, J=6.9 Hz, 2H), 7.35–7.22 (m, 2H), 7.02 (s, 1H), 6.62–6.51 (m, 1H), 5.60 (d, J=5.1 Hz, 1H), 4.39 (d, J=6.8 Hz, 2H), 4.26–4.16 (m, 1H), 4.13–4.00 (m, 4H), 3.94 (s, 3H), 2.69–2.49 (m, 2H), 2.25–2.06 (m, 2H), 1.66 ppm (d, J=5.9 Hz, 3H).

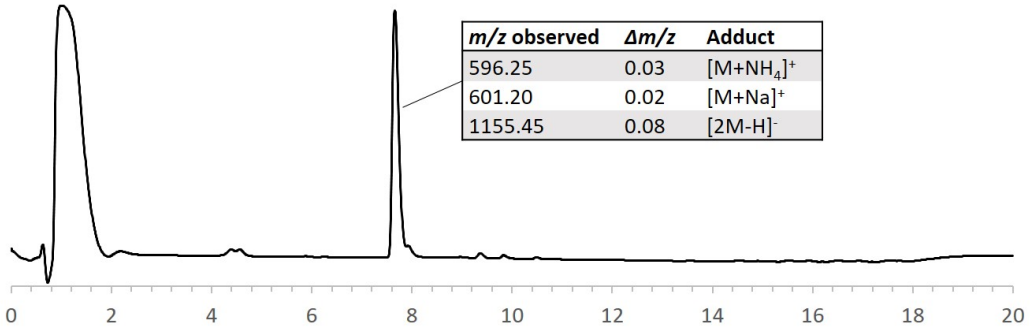

Figure 14: LC-MS analysis (detection at 214 nm) of **PCL-VII** and detected *m/z* (exact mass: 578.19 g mol^{-1}) for t_{ret} = 7.66 min

3.2 Synthesis of Photocleavable Peptide CKFK-PCL-FQF

Synthesis of the photolabile peptide was divided in 3 main steps: 1) Synthesis of FQF in the automated peptide synthesiser, 2) coupling of **PCL-VII** to the FQF resin and 3) Successive coupling of CKFK to the PCL-FQF resin in the automated peptide synthesiser. Solid phase peptide synthesis (SPPS) was conducted following the protocol by Merrifield. Syntheses were conducted from C to N terminus with Fmoc-protected *L*-amino acids. Deprotection of the side-chains as well as cleavage from the resin occured simultaneously in an acidic cleavage cocktail (see Scheme 5). The compound was further purified on preparative scale reversed-phase high performance liquid chromatography (HPLC) and characterised *via* matrix-assisted laser desorption ionisation – time of flight mass spectrometry (MALDI-TOF-MS) (see Table 2). Protonated, sodium and potassium adducts were detected as well as one of the photocleavage products (CKFKG). Since MALDI-TOF-MS measurements employed a 337 nm laser for ionisation, photocleavage products may have been produced in the source. This has already been observed for photocleavable peptides based on nitrobenzoyl linkers used among the group.

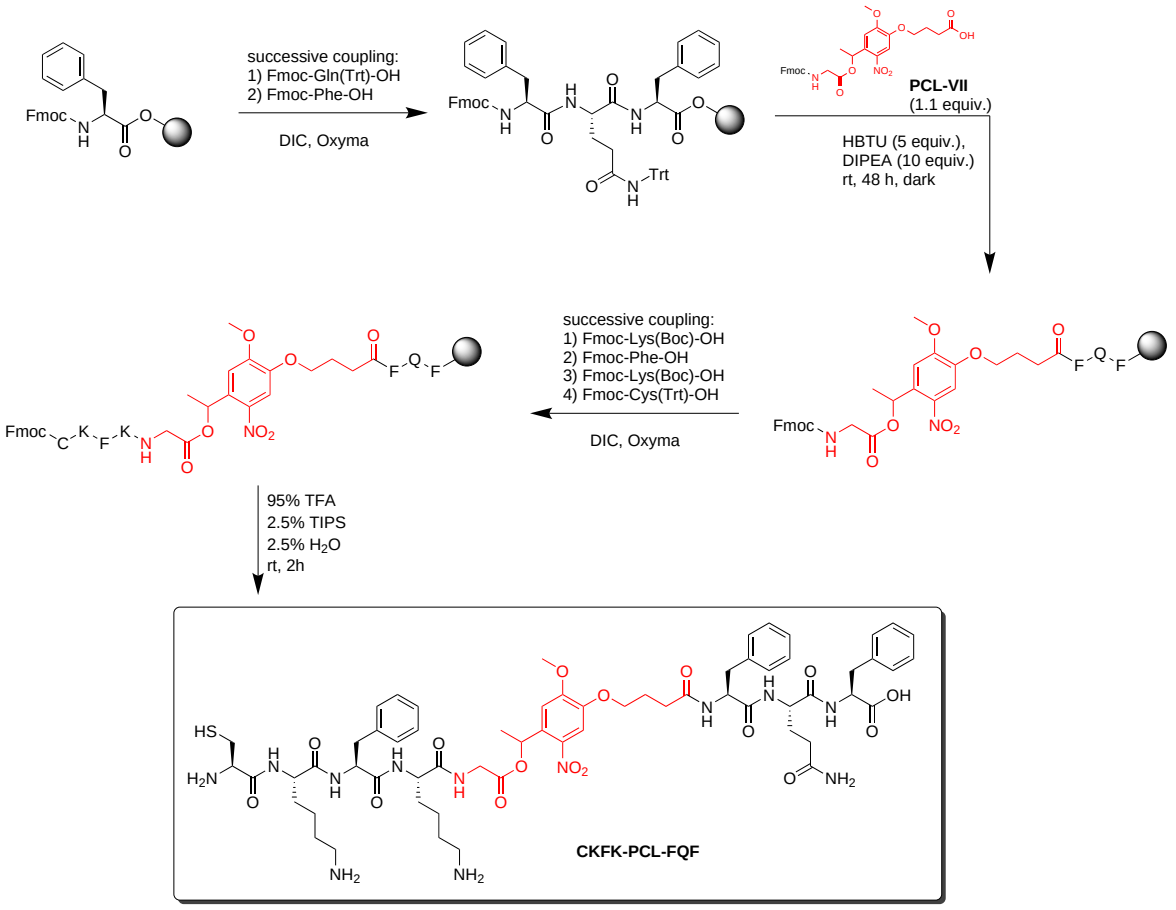

Scheme 5: Synthesis of photocleavable peptide CKFK-PCL-FQF

Table 2: Detected *m/z* in MALDI-TOF-MS analysis for photocleavable peptide CKFK-PCL-FQF after HPLC purification

m/z observed	Δm/z	Adduct
582.0468	-0.2600	[CKFKG+H]+
1285.6202	0.0210	[M+H]+
1307.6017	0.0276	[M+Na]+
1323.5779	0.0298	[M+K]+

3.3 Kinetics of Photocleavage

Prior to any morphology analyses, the triggermechanism of the peptide had to be investigated not only to validate full cleavage of the peptide, but also to adjust irradiation times to a reasonable value. Previous work with the linker **PCL-VII** by Sur *et al.* revealed a half-life of $t_{1/2}$ = 1.9 min when incorporated into the base-sequence $C_{16}V_3A_3K_3G$ (where C_{16} = palmitic acid; V, A, K and G = respective one-letter amino acid codes). Within the first 5 min of irradiation, almost all linkers had been cleaved. Further irradiation from 5 min–10 min showed no significant decrease in intact peptide concentration. [31] Follow-up kinetic experiments of Kübra Kaygisiz with the CKFK-PCL-FQF sequence led to comparable observations for a 10 mg mL^{-1} solution of the peptide in dimethyl sulfoxide (DMSO). Upon irradiation, short-lived intermediates were produced from the intact peptide within 1 min. It has to be noted, that a different lamp (LED at 365 nm, 1 A, 309 mW cm^{-2}) was used which was unavailable during the studies for this work. Instead, a lamp with a wavelength range of 320 nm–400 nm was used (10 500 mW cm^{-1}). Theoretically, an increased intensity would promote a higher cleavage rate of the molecules. However, since the higher intensity is achieved over a broader wavelength range, it cannot be precisely stated how intense the desired wavelength is. During Kübra Kaygisiz' work, the final cleavage products were present after 10 min. [30] Based on these findings a kinetic study of CKFK-PCL-FQF with 9 measuring points was set up: t_0 and 72 h without irradiation and 15 s, 30 s and 60 s, 5 min, 6 min, 10 min and 20 min of irradiation. Since the analyses during this work focused on the behaviour of already formed fibrils, irradiation was conducted in a 1 mg mL^{-1} *Milli-Q* H_2O solution, as opposed to Kübra Kaygisiz´ work. This concentration was adapted from the standard fibrillisation procedure already established in the group (see subsection 4.2.1). [12, 23] Additionally, LC-MS measurements of the aliquots taken at different irradiation times were conducted to identify the fragments. It has to be noted that in HPLC and LC-MS measurements differing methods (gradients, columns) were used. A direct comparison of the peaks between the methods is thus not possible. Due to the electrospray ionisation–mass spectrometry (ESI-MS) source in the LC-MS device, no DMSO was used during sample preparation (high boiling point). Absence of DMSO may influence the fibrillation behaviour of the peptide. However, effects of the solvent (pure water compared to pure DMSO) were expected to have a higher influence on the kinetics (due to permittivity or absorption) than the fibrillation state of the peptide. A study on the difference between single molecules and fibrils regarding the cleavage kinetics was not conducted within the given timeframe. The samples were irradiated at 320 nm–400 nm (for further information see subsection 4.2.2). The previously colourless solution turned increasingly yellow with increasing irradiation time.

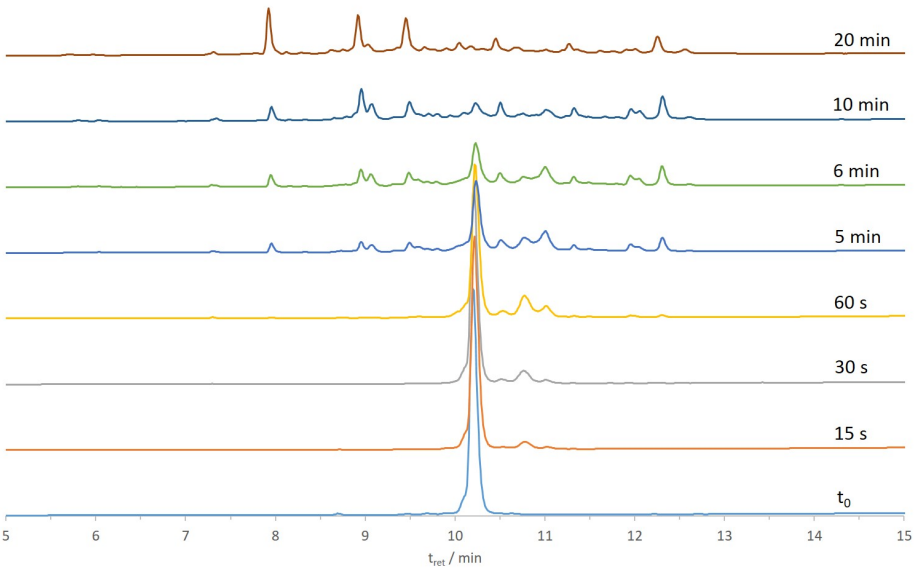

Figure 15: Stacked chromatograms (measured at 254 nm) of the irradiated samples and the non-irradiated t_0 sample on the analytical HPLC. The intact CKFK-PCL-FQF peptide elutes after t_{ret} = 10.2 min

Figure 15 shows the recorded chromatograms of the selected datapoints at 254 nm. The intact CKFK-PCL-FQF peptide elutes after a retention time of t_{ret} = 10.2 min, as observed in the t_0 chromatogram prior to irradiation. LC-MS analysis of the sample showed an mass-to-charge ratio (*m/z*) of 1285.70, matching the protonated $[M+H]^+$ adduct. Starting from 15 s of irradiation, the intact peptide's peak decreased in intensity. Since all samples were taken from the same solution after differing irradiation times, this decrease in intensity can be plotted against the time to give a further insight into the reaction kinetics. Figure 16 shows the respective data points. The intensity value of the sample irradiated for 20 min was not plotted due to its low signal-to-noise ratio (S/N). Fitting of the data points to first-order kinetics revealed a reaction rate constant $k = 0.247\,s^{-1}$ and following calculations according to Equation 3.3 a half-life of $t_{1/2}$ = 2.8 min. Using Equation 3.2, any timespan required for a respective relative intensity (i. e. concentration) can be calculated. For example, to reach a relative intensity of 1 % of the starting value, 18.6 min of irradiation would be required, theoretically. After 10 min of irradiation, less than 10 % of the initial concentration of the intact peptide should be present, which was selected as the irradiation time mostly for comparability to other studies conducted in the group.

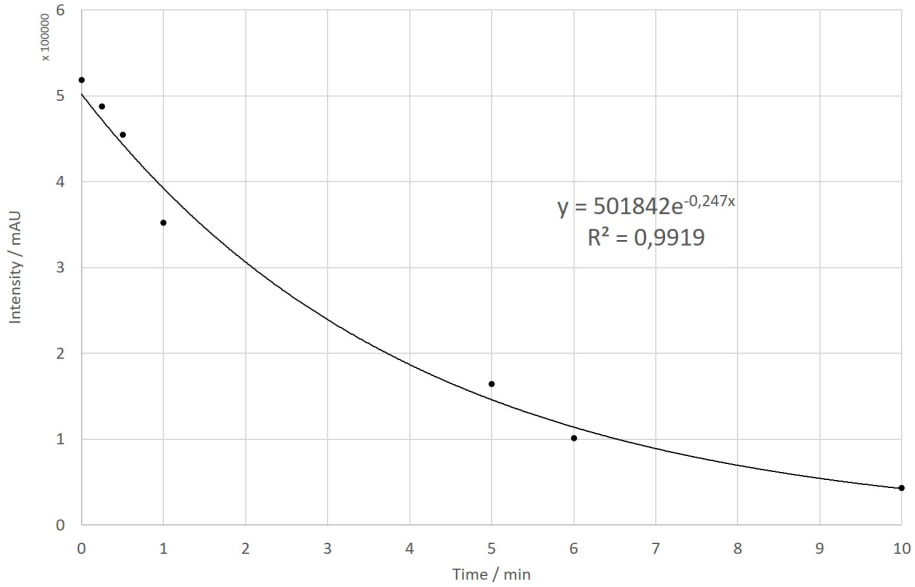

Figure 16: Measured intensities at 254 nm in milli-absorption-units (mAU) of t_{ret} = 10.2 min (CKFK-PCL-FQF) on the analytical HPLC plotted against the respective time of irradiation. The data was fitted to first-order kinetics (excluding data from irradiation time of 20 min due to low S/N).

$$I(t) = I_0 e^{-kt} \tag{3.1}$$

$$t = -\frac{1}{k} \ln \frac{I(t)}{I_0} \tag{3.2}$$

$$t_{1/2} = \frac{\ln 2}{k} \tag{3.3}$$

$I(t)$: Intensity at Time t

I_0 : Starting Intensity

k : Reaction Rate Constant

t : Time

In addition to the decreasing absorbance of CKFK-PCL-FQF, a second peak at t_{ret} = 10.8 min emerged in the 15 s chromatogram, indicating presence of a cleavage product. Until 60 s of irradiation, intensity of this compound increased and decreased again in the following chromatograms. Another peak at t_{ret} = 11.0 min shows a similar decrease after 10 min of irradiation. This indicates that metastable intermediates are formed during the cleavage that further decay on a comparatively large time frame. Upon photocleavage, a five-membered ring intermediate with the same molecular weight as the intact peptide is formed (see Scheme 1, page 7), which might be represented by one of these decaying peaks. Following LC-MS analysis revealed the same *m/z* for 3 of the peaks which will be discussed in the following (see Table 3).

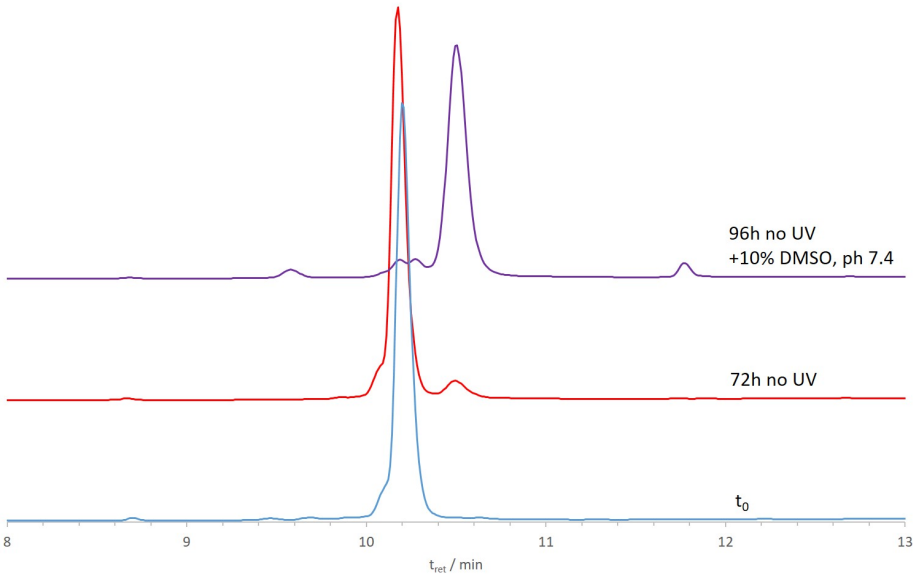

Figure 17: Stacked HPLC chromatograms (measured at 254 nm) of the non-irradiated samples after 0 h, 72 h and 96 h of incubation. The 96 h sample was incubated with 10 % DMSO at pH 7.4. The intact CKFK-PCL-FQF peptide elutes after t_{ret} = 10.2 min, the dimer after t_{ret} = 10.5 min

Additionally, stability of the peptide in solution without irradiation was tested. Immediately after sample preparation, 100 µL of the sample were set aside and incubated in the dark for 72 h before measurement. Figure 17 compares the chromatograms of t_0 and 72 h without irradiation. For the 72 h sample, the intact peptide's peak at 10.2 min is still present with the highest intensity in the chromatogram. However, compared to the t_0 sample, the intensity value decreased by 6 % and a second peak with a retention time of 10.5 min emerged. Previous work by Kübra Kaygisiz found that the cystein residues tend to form disulfide bridges, especially in oxidising environments (i. e. in presence of DMSO). After 24 h in a 10 % DMSO in water solution a significant amount of dimers (approx. 50 %) was formed. [30, 48] LC-MS analysis of the 72 h sample found a matching *m/z* of 1283.00 ($[2M\text{-}2H\text{-}2H]^{2-}$) with a characteristic 0.5 gap compared to the monomer at t_{ret} = 4.6 min. Even though different gradients were used in HPLC and LC-MS, the retention order was not expected to change between the methods. It can therefore be assumed, that the peak following the intact peptide's peak can be assigned to the dimer.

Additionally, another sample that was prepared according to the standard fibrillation procedure (containing 10 % DMSO, see subsection 4.2.1) and incubated for 96 h was measured on the HPLC to confirm retention time of the dimer as well as stability of the peptide in presence of DMSO. The resulting chromatogram is displayed in Figure 17 and the dimer peak at 10.5 min agrees with the retention time observed in the 72 h sample. Apparently, the cystein residues form disulfide bridges even without presence of DMSO, but at a significantly lower rate. Since solutions containing 10 % DMSO were found to promote fibril formation more rapidly than pure H_2O among the group (unpublished data), the findings may also indicate that disulfide bridges aid in fibril formation. Additional peaks at t_{ret} = 9.6 min and 11.8 min might represent the cleavage products CKFKG and PCL*-FQF. Since retention times between analytical HPLC and LC-MS measurements differ due to the methods used, the presence of the two fragments can only be assumed.

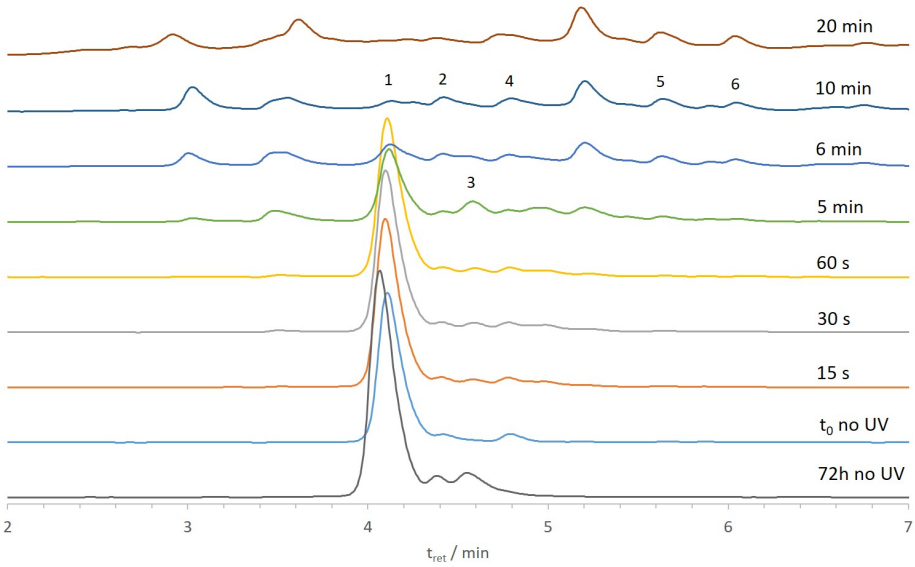

Figure 18: Stacked chromatograms (measured at 254 nm) of the irradiated and non-irradiated samples on the LC-MS system. The intact CKFK-PCL-FQF peptide elutes after t_{ret} = 4.1 min (1).

Figure 18 shows the recorded chromatograms during the LC-MS runs of the samples previously analysed in HPLC. The samples were further diluted to 50 µg L^{-1} with 0.1 % formic acid in *Milli-Q* H_2O prior to the measurements performed by Darijan Schuler and Ali Rouhanipour. Slight differences in elution time of the sample irradiated for 20 min and the non-irradiated sample after 72 h of incubation in comparison to all other chromatograms might have been caused by differing measurement days (no internal standard was used for referencing).

Six of the peaks observed could be assigned to a structure as shown in Table 3. The intact CKFK-PCL-FQF peptide elutes after 4.1 min (1), a fragment of the photocleavage (CKFKG) after 5.6 min (5). Additionally, the disulfide-bridged dimer of CKFK-PCL-FQF was detected at 4.6 min (3) and a fragment of PCL*-FQF at 4.4 min (2) which agrees with the findings of Kübra Kaygisiz. Furthermore, the *m/z* for the intact peptide's $[M+H]^+$ peak was also found at 4.8 min (4), which might indicate presence of the five-membered cyclic intermediate of the photocleavage (see Scheme 1) as suspected previously during HPLC analysis. However, this assumption cannot be verified by MS analysis alone, but requires a structural analysis method (e. g. NMR). Additionally, Barth *et al.* found that nitroso products of the Norrish Type II cleavage mechanism may undergo further reactions with thiols as outlined for PCL*-FQF in Scheme 3 on page 9. [34] The respective circular product (presumably formed by reaction with cystein residues) was found at t_{ret} = 6.0 min (6).

Table 3: Observed peaks at respective retention times in LC-MS analysis as well as observed *m/z*, deviation from theoretical values ($\Delta m/z$) and formed adducts for positive and negative ionisation mode. M_x for the adduct composition refers to the suggested structures, respectively.

Peak No.	t_{ret} / min	m/z observed	Δm/z	Adduct	Suggested Structure
1	4.1	643.60	0.30	$[M_1+2H]^{2+}$	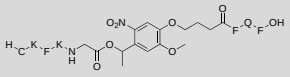
		1285.70	0.10	$[M_1+H]^{+}$	
		1283.65	0.08	$[M_1-H]^{-}$	
2	4.4	549.35	0.12	$[M_2+Na]^{+}$	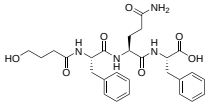
3	4.6	1283.00	0.43	$[M_3-2H]^{2-}$	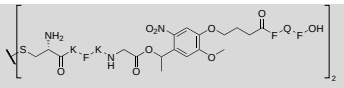
4	4.8	643.45	0.15	$[M_4+2H]^{2+}$	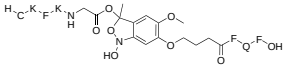
		1285.55	-0.40	$[2M_4+3\,H_2O+2H]^{2+}$	
5	5.6	1190.60	0.02	$[M_5+H]^{+}$	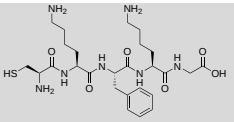
6	6.0	688.35	0.05	$[M_6+H]^{+}$	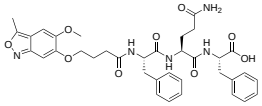
		710.30	0.02	$[M_6+Na]^{+}$	
		686.10	-0.18	$[M_6-H]^{-}$	

3.4 Behaviour of Preformed Fibrils upon Exposure to UV Light

As previously determined, the primary structure of the peptide is mostly (92 %) disrupted within 10 min of irradiation due to cleavage of the photolinker **PCL-VII**. However, since the pre-formed secondary and higher-order structures are mainly stabilised *via* non-covalent bonds such as hydrogen bonding, electrostatic interactions and hydrophobic effects, these assemblies may not necessarily break down immediately. Alternatively – in case the energy barrier for a disassembly is too high – their superstructure may even stay intact after cleavage of the peptide (see Figure 19).

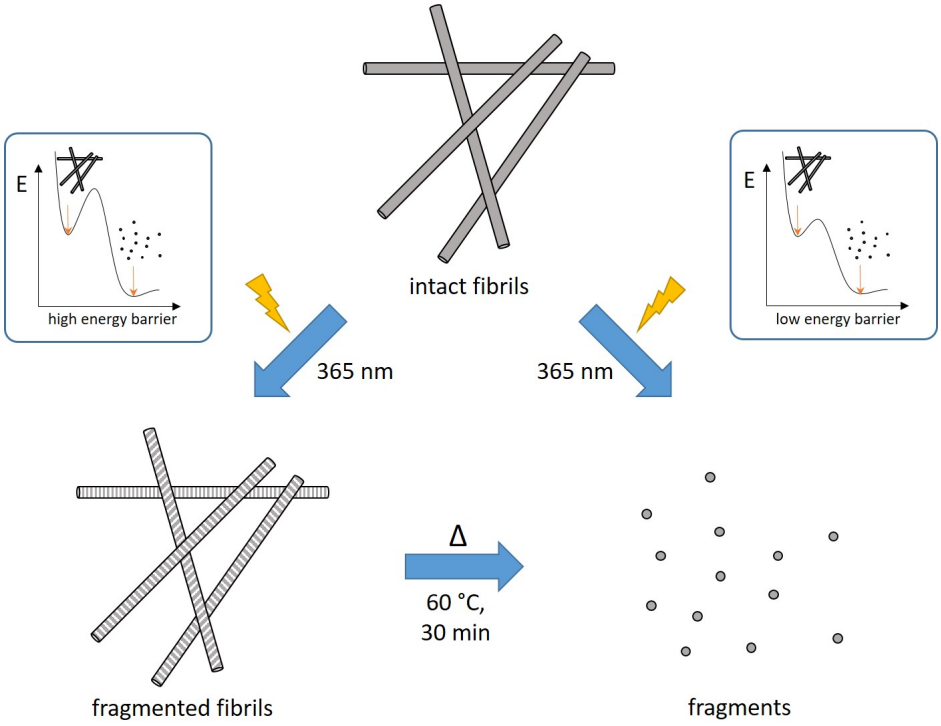

Figure 19: Theoretical events after irradiation of photocleavable peptide CKFK-PCL-FQF depending on the energy barrier between fibrillised and fragmented state

The morphology studies were generally set up as outlined in Figure 20. 10 mg mL^{-1} stock solutions in DMSO were diluted with *Milli-Q* H_2O to a concentration of 1 mg mL^{-1}, adjusted to a pH of 7.4 and incubated for 24 h in the dark to induce fibril formation. Exceptions regarding DMSO stocking were made for methods where the solvent would interfere with the measurements (LC-MS, CD, NMR). Here, the peptide was directly dissolved in water at 1 mg mL^{-1} which can cause decreased or slower fibril formation compared to analyses with DMSO stocking. After the incubation, an aliquot of the sample was set aside and kept in the dark for evaluation of fibril stability (72 h no UV). t_0 samples were prepared immediately before and after irradiation. The samples were further monitored every 24 h for 3 days unless stated otherwise. Conducted deviations from this setup are stated for the respective methods used.

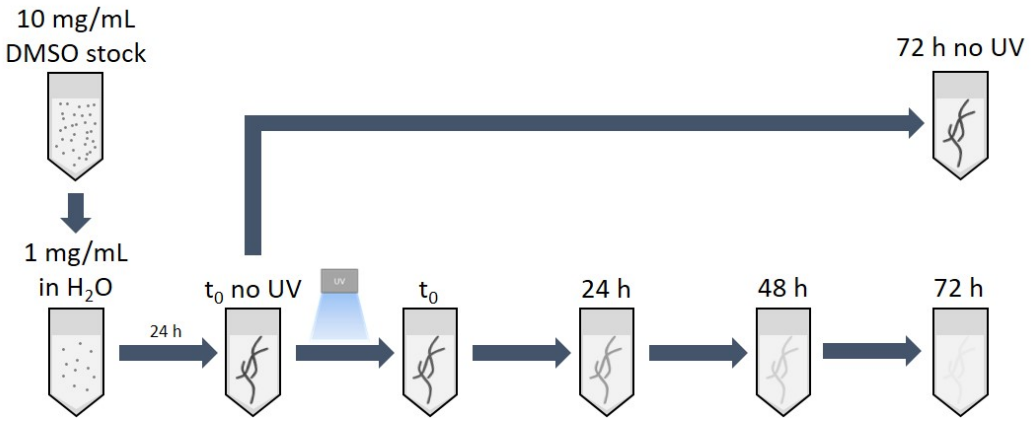

Figure 20: General setup of the morphology studies

3.4.1 Investigation of Disassembly Kinetics on Nanoscopic Scale

To evaluate the changes in the nanoscopic structure of the assembly, ThT, CD, FTIR and NMR studies were conducted. The results will be presented and discussed in the following.

3.4.1.1 ThT Assay

A ThT assay was conducted to gain insight into the amyloidic character of the assembly in a 1 mg mL^{-1} solution at pH 7.4. 2 µL of the sample were incubated in 10 µL of a 50 µM ThT solution for 10 min–15 min and measured immediately after. As measuring points t_0 without irradiation, t_0 after irradiation and 24 h, 48 h and 72 h incubation after the irradiation were selected. Additionally, another measurement after 72 h of incubation without previous irradiation was added to prove stability of the structure in the aqueous solution over the time course of the study. The expected outcome was a high flourescence intensity for the non-irradiated samples and a significant decrease in fluorescence intensity over time for the samples that were irradiated for 10 min at 365 nm.
Native CKFKFQF was used as positive control during the experiment. Sample preparation was conducted similarly to CKFK-PCL-FQF. However, despite its formation of PNFs in aqueous media already demostrated by Schilling *et al.* [12], CKFKFQF did not show the typical increase in fluorescence of ThT after incubation. Since Schilling *et al.* did not conduct ThT assays, it is not known whether the observations were caused by e. g. sample pretreatment, or if CKFKFQF actually produces false negatives. However, other members of the group who conducted experiments with the same peptide sequence found a similar behaviour of CKFKFQF in ThT assays, indicating that the peptide actually produces false negatives. In general, false negatives may occur due to structural differences in the side-chain grooves, such as a tighter twist of the superstructure or the availability of aromatic side-chain grooves, as investigated e. g. by Cloe *et al.* for a mutant of Aβ. [49]

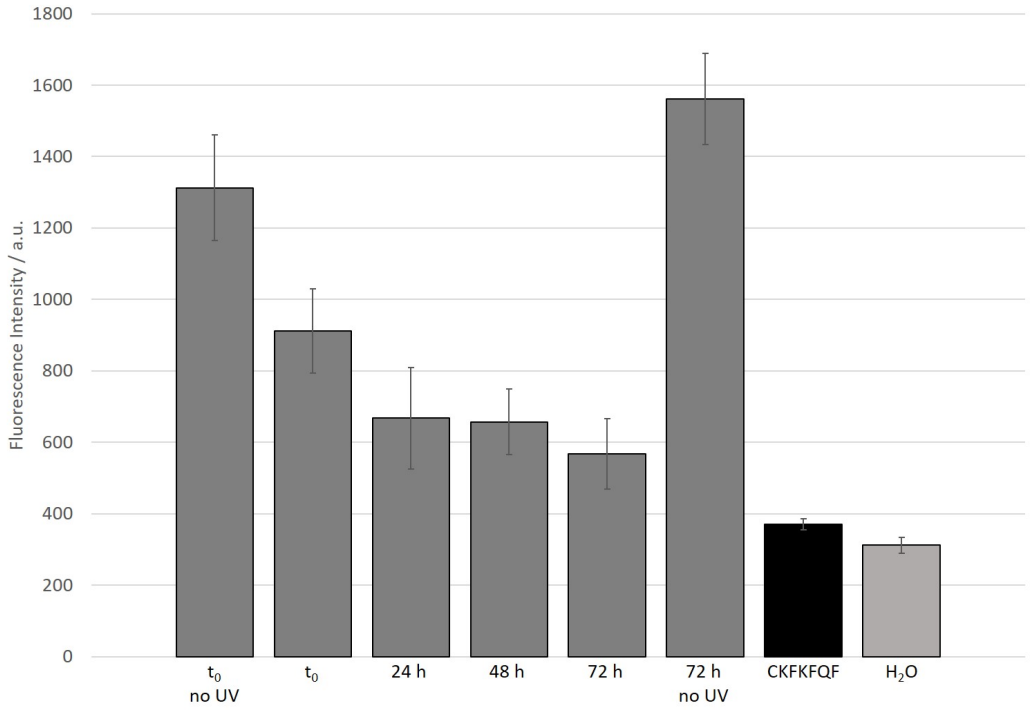

Figure 21: ThT assay of CKFK-PCL-FQF with varying incubation times after irradiation. Samples were measured in triplicate and averaged. Results for CKFKFQF and H_2O (negative control) were averaged over all samples. The negative control was prepared similar to all other samples (2 µL H_2O in 10 µL 50 µM ThT solution).

Figure 21 shows the results of the disassembly study. As expected, the samples that were not exposed to UV light (t_0 no UV, 72 h no UV) showed a 3- to 4-fold higher fluorescence intensity when compared to the negative control (*Milli-Q* H_2O in 50 µM ThT solution). This shows that the formed fibrils are stable in the solution without exposure to UV light.

After irradiation, the fluorescence intensity of $t_{0,UV}$ shows a rapid decrease by about one third of its initial value. This might indicate that the ordered β-sheet structure was already partially disrupted, or that at least the side-chain-grooves were not as accessible for the ThT molecules. Since computations by Wu *et al.* indicated a binding preference of ThT towards grooves created from aromatic residues [39], the molecules might preferably intercalate between residues 3 (F) and 6 (F) as well as 6 and 8 (F) in CKFK-PCL-FQF (counting linker PCL as a single residue). The photoinduced disruption into CKFKG (with a free carboxylic acid group) and PCL*-FQF might alter the hydrophobic interactions in the channels formed by the third and sixth residue, resulting in less molecules intercalating into the amyloid structure and thus a decreased fluorescence intensity. However, since the channel between residues 3 and 6 is significantly larger than the one between the 6th and 8th residue due to the photocleavable linker, it is not known whether ThT actually intercalates here. On one hand, the additional aromatic structure of PCL in the backbone of the peptide might aid ThT binding *via* hydrophobic effects, but on the other, the longer distance between the side-chains creating the groove might cause a weaker hydrophobic interaction with the side-chains in general.

Additionally it should be stated that the concentration of peptide used during the ThT assay was significantly lower (0.2 mg mL^{-1}) than the one used for formation of fibrils and during irradiation (1 mg mL^{-1}) due to the addition of the ThT solution. Even though this low concentration was not reached until 10 min–15 min before the measurement, the decrease in concentration might still pro-

mote mobility of the single molecules in the solution, resulting in a faster disassembly than observed for other analysis methods.

The measuring points at 24 h and 48 h of incubation after irradiation show a visible, but not significant decrease in fluorescence. After 72 h, fluorescence intensity had decreased to less than half of its initial value, with the negative control value still being slightly lower (approx. 55 % of irradiated 72 h). These findings suggest that the amyloidic nanostructure is not entirely disassembled after 72 h. The remaining fluorescence might as well be a result of incomplete cleavage of all photosensitive linkers due to the irradiation time.

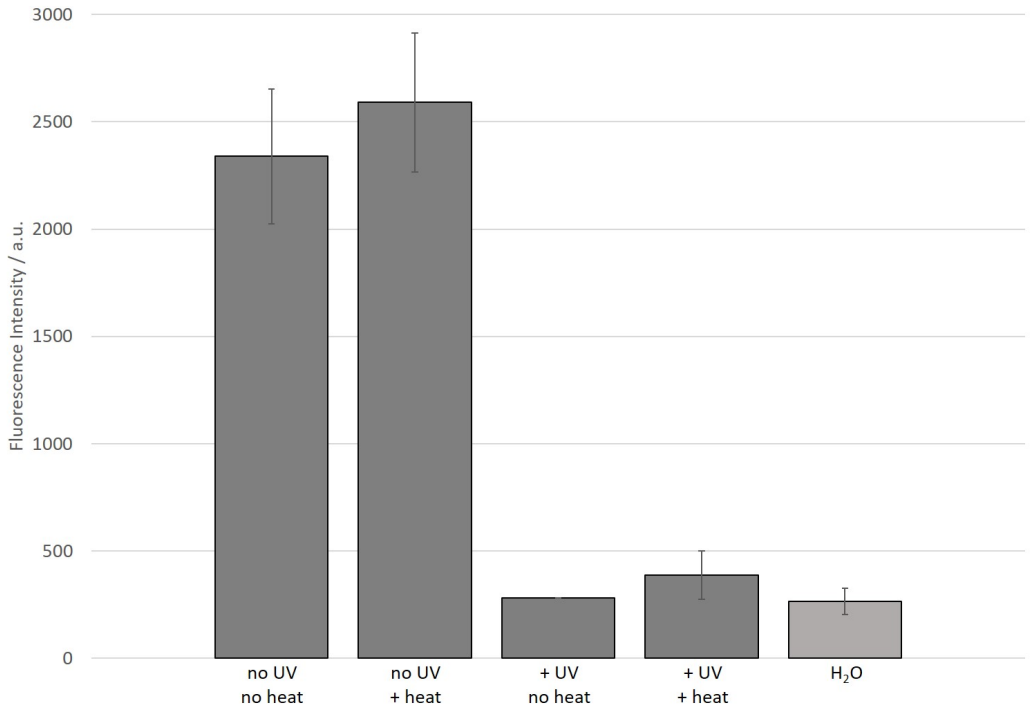

Figure 22: ThT assay of CKFK-PCL-FQF with varying heat and irradiation treatment. Samples were measured in triplicate and averaged. Results H_2O (negative control) were averaged over all samples. The negative control was prepared similar to all other samples (2 µL H_2O in 10 µL 50 µM ThT solution). Sample 4 (+ UV, + heat) was first irradiated, then heated.

Additional measurements involving heating of the samples to 60 °C for 30 min without and after irradiation were conducted to further investigate disassembly kinetics. The results are displayed in Figure 22. No significant difference in fluorescence was observed between the two non-irradiated samples, regardless of heat treatment. This indicates stability of the fibril system towards the selected heat treatment. On the other hand, no further fibrillation seemed to have occured, at least not in a way that would aid ThT intercalation in the structure. Possibly, fibril elongation by connection of shorter fibril segments into longer ones occured. This would however not have yielded higher fluorescence intensities since the number of binding sites for ThT would not have been influenced by this effect.

After irradiation, a rapid drop in fluorescence intensity was observed (similar to negative control), even for the non-heated sample. This contradicts the previous findings, where fluorescence decreased over a much larger timescale after irradiation (see Figure 21). Since the previous measurements were conducted twice with similar results, the low fluorescence during the heat experiments

was most likely caused by external factors such as missing homogenisation of the solution before sample preparation. The measurement could not be repeated during the given timeframe. For the sample that was heated after UV irradiation, very low fluorescence similar to the negative control was observed. These findings strengthened the previous assumption that increased mobility would promote more rapid fibril disassembly after the photocleavage. A high energy barrier seemed to trap the fibrils in the intact state for at least 3 days. By heating to 60 °C for 30 min, the energy provided apparently sufficed for complete fibril disassembly (fluorescence similar to negative control, see Figure 22, +UV +heat).

3.4.1.2 CD Spectroscopy

To evaluate presence of the internal β-sheet structure of the fibrils, a CD spectroscopy study was conducted. Similar to HPLC kinetic studies, samples were prepared without DMSO due to its high absorption in the UV region. A 1 mg mL^{-1} solution in *Milli-Q* H_2O was prepared and the pH was adjusted to 7.4 using aqueous 0.2 M NaOH solution. Irradiation was conducted with the 1 mg mL^{-1} solution. The samples were diluted to 0.2 mg mL^{-1} immediately before the measurements. Molar ellipticity values were calculated after subtraction of a background spectrum (*Milli-Q* H_2O) using Equation 3.4. [40] Since any data point in the recorded spectra always represent a proportionate mix of the secondary structures present and it is not known which influence the photolinker (containing a chiral carbon) and its cleavage had, the spectra were evaluated only qualitatively. Similar to the ThT assay results, control peptide CKFKFQF produced ambiguous results (most likely resembling random coil structures) and will therefore not be further evaluated. These results may however provide an explanation for the low ThT fluorescence, but require additional investigation. All in all, CKFKFQF may not be as suitable as a control peptide for CKFK-PCL-FQF as initially expected.

$$[\theta] = \frac{100 \cdot \theta_{obs}}{d \cdot c} \tag{3.4}$$

$[\theta]$: Molar ellipticity in ° cm^2 dmol^{-1}

θ_{obs} : Observed ellipticity in °

d : Optical path length in cm

c : Molar concentration in mol L^{-1}

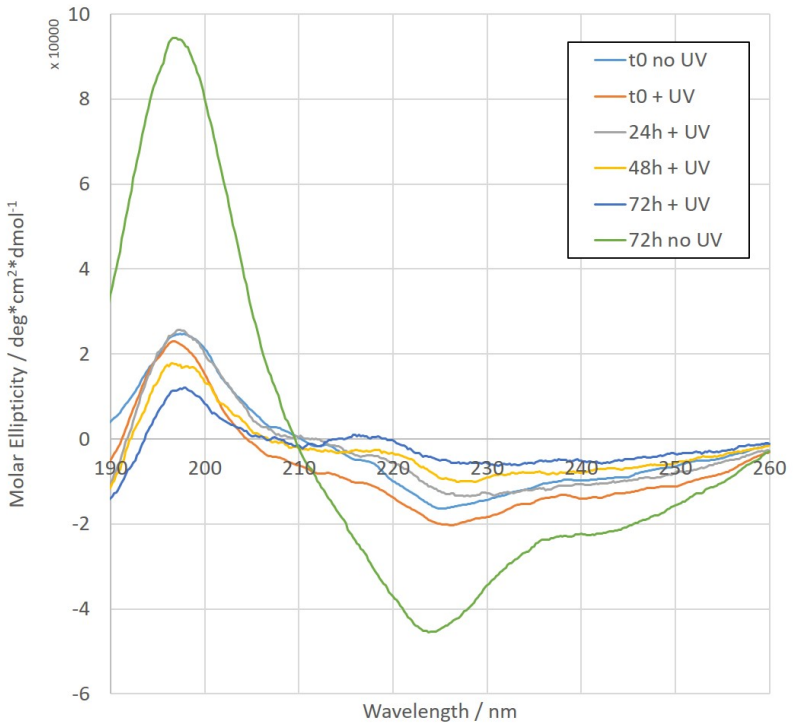

Figure 23: Molar ellipticity data of CKFK-PCL-FQF in the far UV range

Figure 23 shows the collected molar ellipticity data for CKFK-PCL-FQF in the 190 nm–260 nm range. Typically, pure β-sheet structures can be identified by a maximum in the 195 nm–200 nm range and a minimum in the 215 nm–220 nm range. All of the measured samples show a maximum at 197 nm, with decreasing intensity according to the incubation time after irradiation. This could hint at a degradation of β-sheet structures. Furthermore, a minimum in the negative at 225 nm nears zero with increasing incubation time after the irradiation. In this region, random coil structures usually show positive values close to zero which might indicate a morphology shift towards random coils following the photocleavage. Interestingly, the spectrum of the non-irradiated sample after 72 h of incubation shows an about 4-fold increase in molar ellipticity compared to the non-irradiated t_0 sample. This might indicate that formation of fibrils progresses significantly slower in pure water when compared to water with 10 % DMSO, which agrees with previous findings on other peptides among the group (unpublished data).

3.4.1.3 FT-IR Spectroscopy

In parallel with CD spectroscopy measurements, FTIR samples were prepared according to the standard fibrillation procedure (see subsection 4.2.1). 200 µL were freeze-dried at the given time-points (t_0 before and after irradiation, 24 h, 48 h and 72 h after irradiation) and the solids stored in the freezer until measurement. A few crystals of the samples were placed on the ATR crystal for measurement, Figure 24 shows the recorded spectra in the amide I and II region.

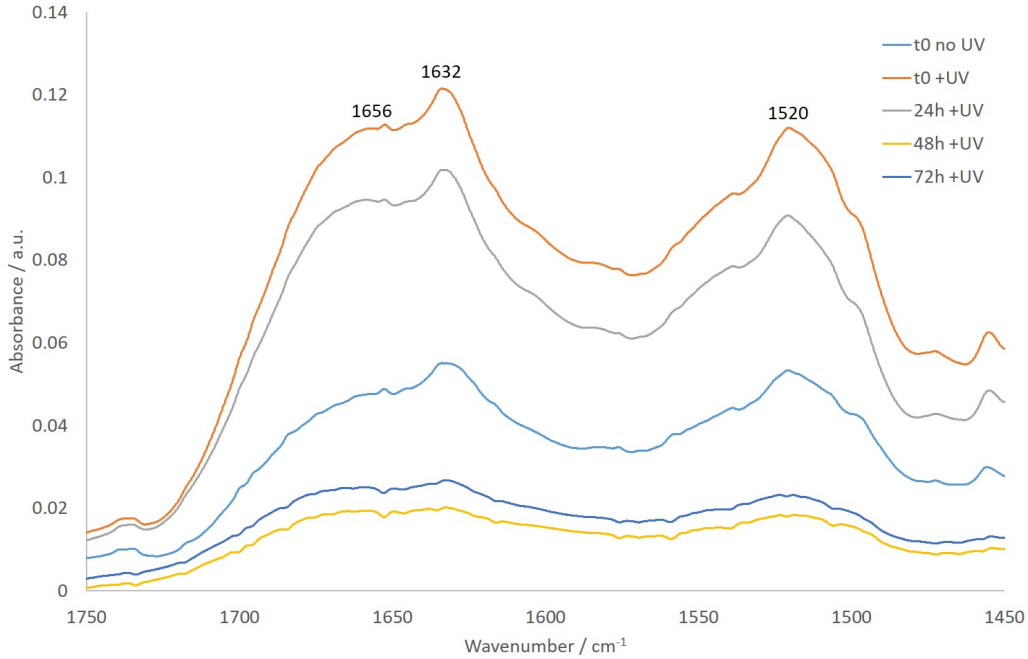

Figure 24: Recorded ATR FTIR spectra of photocleavable peptide CKFK-PCL-FQF before and after irradiation with differing incubation times. Only the amide I and II region are shown and significant peaks are labeled.

Interestingly, absorbance of the samples seemed to increase after irradiation (t_0 +UV, 24 h +UV) and remained at higher values before dropping below the initial values (t_0 no UV) for the 48 h and 72 h samples. This might indicate conformational changes of the preformed fibrils after UV irradiation until collapse of the structure after 48 h. However, since the fragments of the photocleavage reaction (PCL*-FQF and CKFKG) are not able to form fibrils [30], but were only expected to retain intact structures for an unknown amount of time, repetition of the measurements is required. Additionally, the ATR crystal was not entirely covered with sample which might have caused variations in calculated absorbance.

In Figure 24 a maximum is located at 1632 cm^{-1} with a broad shoulder at 1656 cm^{-1}. The sharp signal at 1632 cm^{-1} (major contribution from C=O stretching) might be indicative for the amyloidic structure, even though the wavenumber was slightly above the suggested range for amyloids. Since fibrils were observed during the TEM measurements (discussed in the following), the signal can safely be assigned to the amyloid β-sheet structure. Shifts towards higher wavenumbers may be a result of larger twist angles of the sheets and fibrils compared to average amyloids or a decreased number of strands per β-sheet. [9] The broad shoulder on the other hand shows typical wavenumbers for helical or randomly distributed structures and might be an indicator that fibrillation did not yet reach thermal equilibrium (which agrees with observations from TEM imaging that will be discussed in the following). After 48 h of incubation, the curve had flattened significantly, indicating breakdown of secondary structures. Typically, amyloid bands can be found in the range of 1611 cm^{-1}–1630 cm^{-1}, the combination of amyloid bands with lower wavenumbers and presence of a high frequency band at approx. 1690 cm^{-1} are indicators of antiparallel β-sheet structure. Since the observed amyloid band is shifted towards higher wavenumbers and no high frequency band was observed, the fibrils seem to adopt a rather parallel β-sheet orientation. These findings agree with various studies on fibrils

suggesting that antiparallel β-sheets are the preferred conformation only during the first stages of fibril formation (nucleation) and for later stages (elongation) parallel sheets are preferred. [9, 16]
Additionally, a broad maximum in the amide II region at 1520 cm^{-1} was observed, that also significantly decreased in intensity after 48 h of incubation. It can be assigned to N-H in-plane bending and C-N stretching vibration of the secondary amides. Location of this band can also hint at the respective secondary structure present in the peptide. For β-forms, the band appears at 1520 cm^{-1}–1525 cm^{-1} which agrees with the observations. [42]

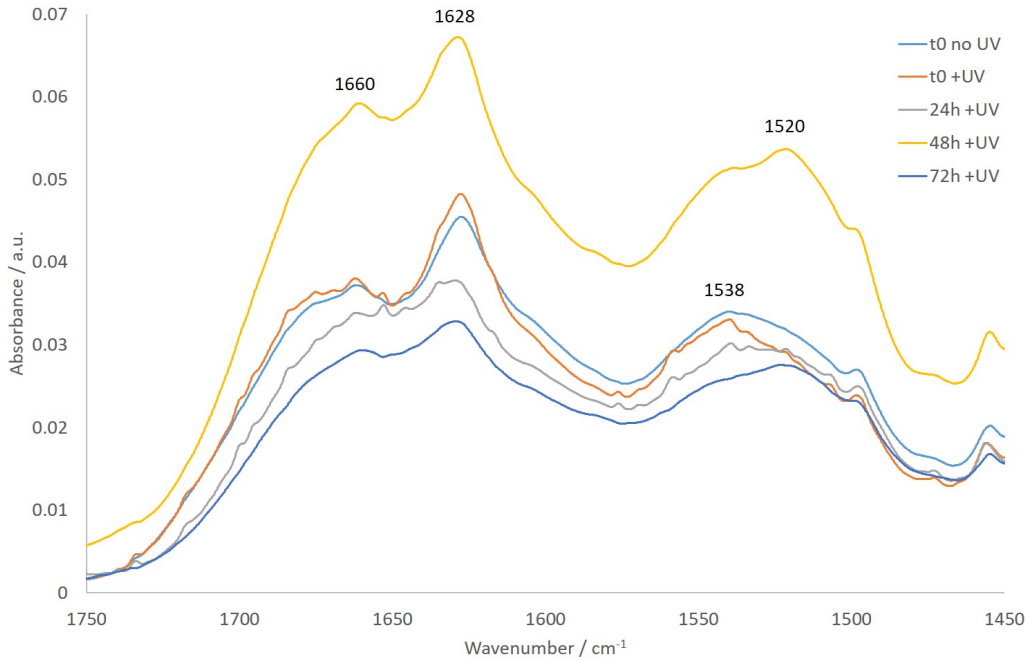

Figure 25: Recorded ATR FTIR spectra of photostable control peptide CKFKFQF before and after irradiation with differing incubation times. Only the amide I and II region are shown and significant peaks are labeled.

For the control peptide CKFKFQF (see Figure 25), the amyloid band appears at 1628 cm^{-1}. Again, no high frequency band was observed, which indicated parallel rather than antiparallel β-sheets. The sharper peak at 1660 cm^{-1} (compared to the shoulder in the spectra of CKFK-PCL-FQF) might indicate presence of α-helical structures. In proteins, a peak at this wavelength can also be an indicator of β-turns. [9, 42] However, due to the comparatively short amino acid sequence of 7 monomers, a β-turn structure is rather unlikely.
In the amide II region, a peak shift from 1538 cm^{-1} in the t_0 and 24 h samples towards 1520 cm^{-1} for 48 h and 72 h might indicate decrease of α- (1540 cm^{-1}–1550 cm^{-1}) and increase of β-form content over time. [42] Similar to the observations on the photocleavable peptide, this indicates that the endpoint of the fibrillation was not yet reached.

3.4.1.4 NMR Spectroscopy

In NMR spectroscopy, width of the observed signals depends on interactions among the magnetic nuclei among other things. Due to an increase in spin-spin-relaxation processes, lines of larger molecules, polymers and proteins are broader when compared to small molecules. The spectra of

hierarchically organised peptides are affected in a similar manner. Therefore, a measurement of pre-formed fibrils was expected to yield very broad proton peaks. Upon irradiation, as fibrils break down and mobility of the cleavage product increases, a rise of sharp signals should be observable. Samples were prepared as 5 mg mL^{-1} *Milli-Q* H_2O solutions (no DMSO). Prior to irradiation, measurements after 24 h of incubation (for fibril formation) and 72 h of incubation were conducted. Since even after 512 scans no signals could be observed for the highly viscous sample, spectra were recorded at elevated temperature (45 °C). Contrary to previous measurements, irradiation was conducted directly in the NMR tube instead of an open *Eppendorf* tube. Since typical NMR tubes are composed of borosilicate glass which has a high transmission at 365 nm (>90 % for 1 mm thickness) and the solution turned yellow during irradiation, it was assumed that cleavage of the photolabile linker occured. It was not evaluated whether the viscosity of the sample changed after irradiation. After irradiation, the sample was monitored every 10 min (128 scans) for 4 days. Start- and endpoints are displayed in Figure 26.

Comparison of the spectra before and after irradiation showed a significant difference of about 0.2 ppm in the chemical shift of almost every peak. Since the samples before irradiation were measured at 45 °C and the samples after irradiation only at room temperature, this shift was most likely caused by the temperature difference. Following this assumption, all spectra were aligned to the peak at 2.850 ppm, to determine differences between the spectra more easily. It should as well be noted that differences in intensities between non-irradiated and irradiated samples are mainly a result of the differences in scan accumulation numbers. Since the aim of this study was to investigate changes in peak shapes after irradiation (a dynamic process), a lower scan number was used to lower the time needed for datapoint creation. Furthermore, slight differences in peak broadening between the measurements at room temperature and 45 °C can be attributed to the decreased mobility of the fibrils at lower temperature.

The non-irradiated samples at t_0 and after 48 h of incubation after fibril formation showed no significant differences, indicating stability of the fibrils in the solution. Data from the CD measurements pointed towards the assumption that fibril formation did not reach equilibrium state after the first 24 h of incubation of the standard fibrillation procedure without the use of DMSO. Due to absence of further peak broadening in the NMR spectra from t_0 to 48 h and the higher concentration used for the measurements, equilibrium might have been reached faster for the NMR measurements. However, this assumption would need further investigation of the fibrillation process.

Comparison of the irradiated samples 15 min and 96 h after irradiation showed no significant differences either. This suggested that either defibrillation was already finished 15 min after the irradiation (which seemed rather unlikely due to findings from other analyses), or that even after 96 h the disassembly process did not proceed on a significant scale. Comparison of non-irradiated and irradiated samples showed no significant changes in the aliphatic region between either one of the samples. The aromatic and amide region however, showed some differences in chemical shifts: a peak in the non-irradiated spectra at 6.791 ppm shifted to 6.894 ppm while surrounding peaks did not shift. The applied for a peak at 7.697 ppm (to 7.820 ppm) and 8.061 ppm/8.189 ppm (to 8.374 ppm). These findings might indicate successful breakage of the photocleavable linker within the peptide. However, since no peak sharpening was observed, it was assumed that no disassembly of the peaks occured.

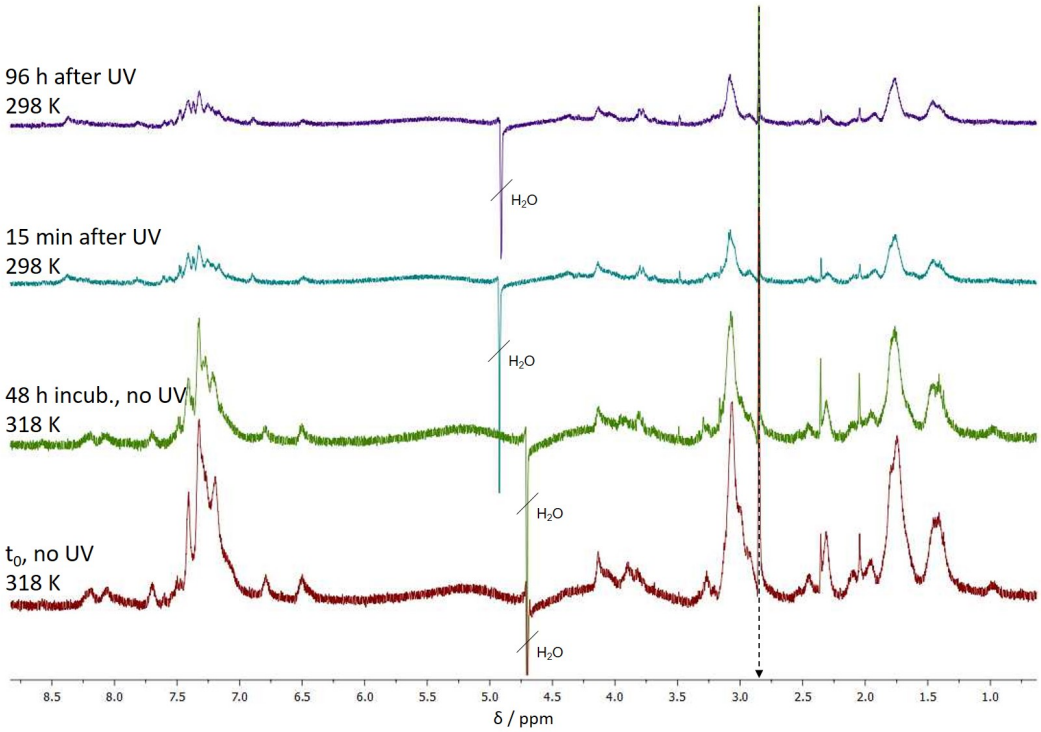

Figure 26: NMR spectra of CKFK-PCL-FQF fibrils before and after irradiation. Spectra were aligned to a significant peak at 2.850 ppm (black arrow). The negative peaks at 4.701 ppm (non-irradiated, 318 K) and 4.922 ppm (irradiated, 298 K) are a result of water suppression.

The reason behind this could have been the high concentration of 5 mg mL^{-1} trapping the fibrils in the intact state despite backbone cleavage. Additionally, the differing setup for irradiation might have caused a decreased intensity and therefore less cleavage reactions and less destabilisation. To further investigate these assumptions, the sample was measured again 1 week after the irradiation at room temperature and 45 °C (see Figure 28). Compared to previous spectra, sharpened peaks in the aromatic and aliphatic area were observed (cut-outs of the spectra) even at room temperature, indicating disassembly of the fibrils to an unknown degree. Additionally, a peak at 2.046 ppm in the non-irradiated sample that showed no shift for other measurements shifted to 2.562 ppm in the 1 week old samples. The findings suggested that – presumably due to the increased concentration – disassembly occurs at a much slower rate when compared to other analyses. However, further investigation of the sample using other methods would be necessary to safely determine the degree of disassembly. Further NMR analyses may as well allow for peak assignment and viscosity monitoring, but were not conducted during the course of this study.

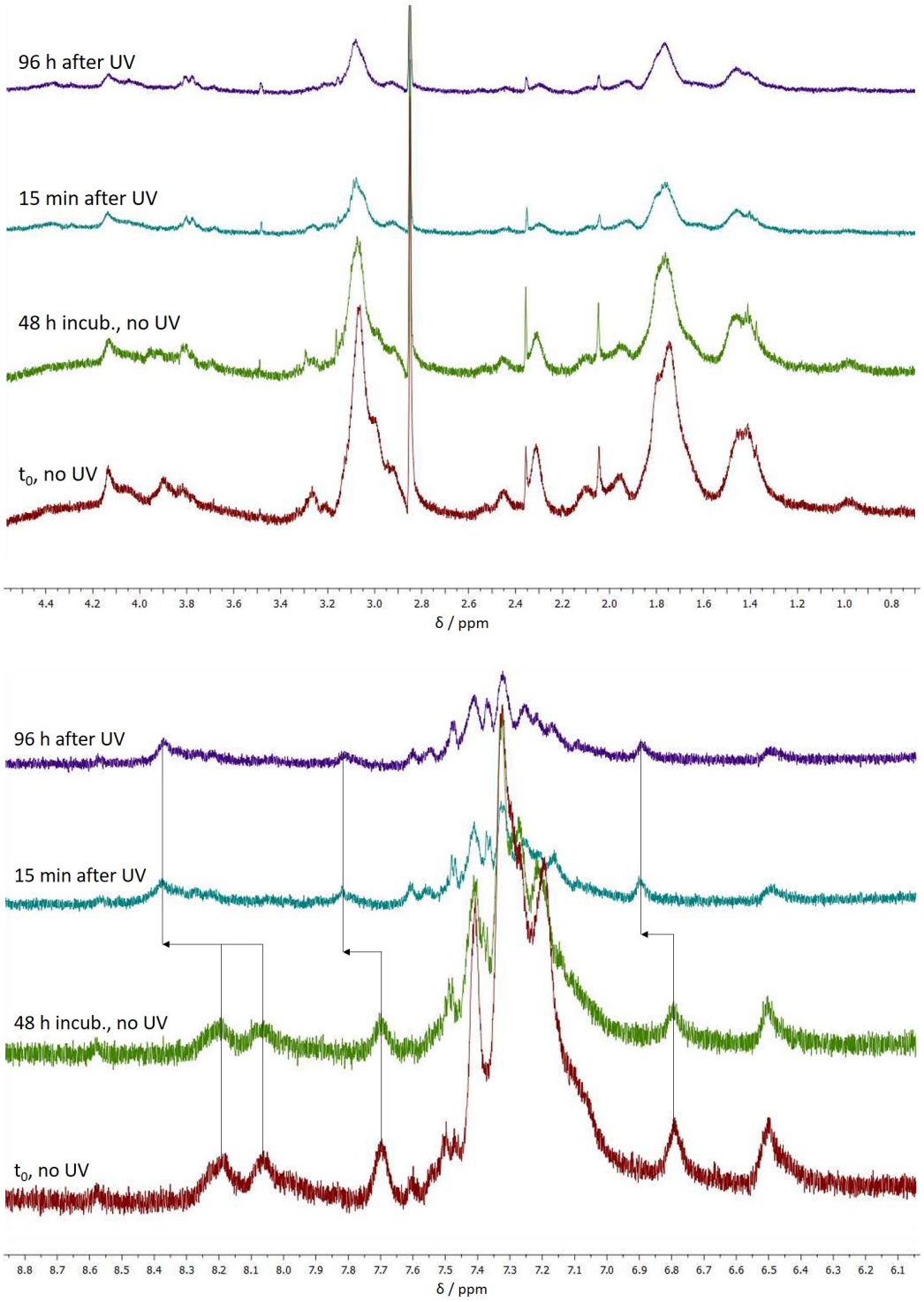

Figure 27: Zoomed sections of NMR spectra of CKFK-PCL-FQF fibrils in aliphatic (top) and aromatic (bottom) areas.

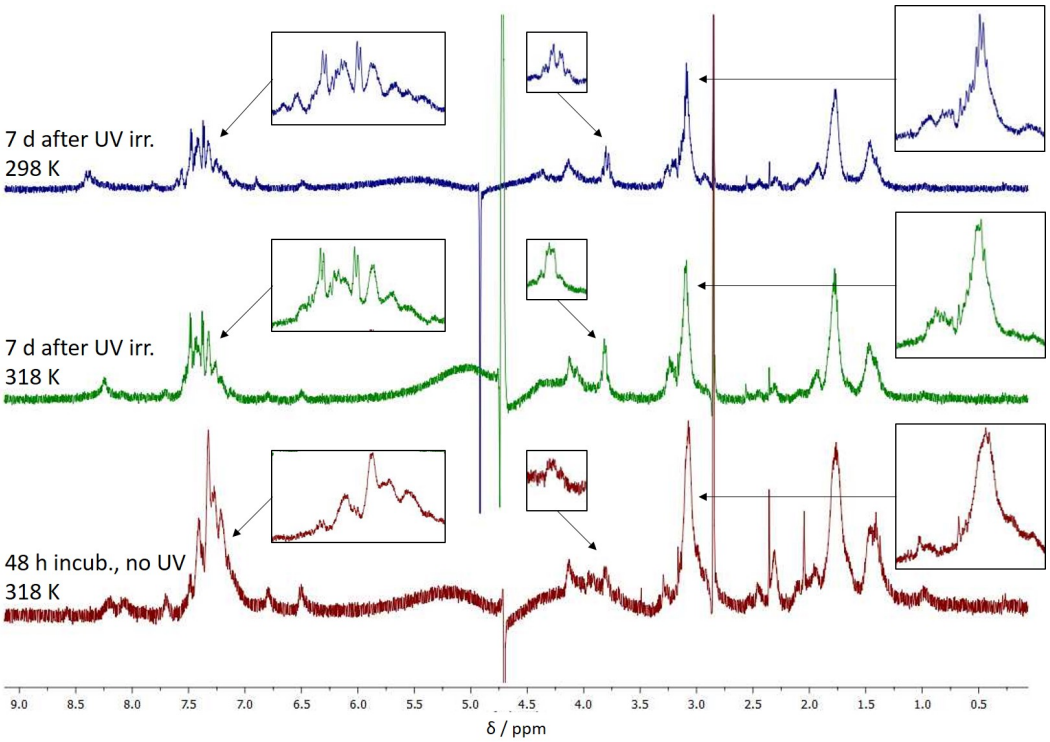

Figure 28: NMR spectra of CKFK-PCL-FQF fibrils 1 week after irradiation. The peaks at 4.701 ppm (318 K) and 4.922 ppm (298 K) are a result of water suppression. Zoomed cut-outs of significant peaks (with changes in sharpness) were added. Stacked cut-outs all respresent the same ppm range, respectively.

3.4.2 Investigation of Disassembly Kinetics on Microscopic Scale

After investigation of underlying nanoscopic structures, the system was examined on microscopic scale. This included imaging methods TEM and AFM. Based on findings from the previous analyses it was expected that the fibrils would disassemble after irradition on a larger timescale (days). Furthermore, non-irradiated samples should be stable for at least 72 h in a 1 mg mL^{-1} aqueous solution.

3.4.2.1 TEM Imaging

The TEM study was set up similarly to previous 4-day measurements: t_0 and 72 h without irradiation, t_0 after irradiation and 24 h, 48 h and 72 h incubation after the irradiation. Samples were incubated and irradiated in aqueous 1 mg mL^{-1} solution and stained with 1 % uranyl acetate in EtOH on the grids. Figure 29 shows the non-irradiated samples. Similar to the expectations, both samples show a net of fibers on the micrometer scale. This proves that not only the single molecules but also their superstructure is stable over the course of 3 days. Additionally, the sample incubated for further 72 h following the standard fibrillation procedure (see subsection 4.2.1) developed a dense, rug-like network of fibrils. This indicates that the system was not in its equilibrium state after the first 24 h of incubation from the procedure, but continued to form fibers for an unknown amount of time. These findings agree with observations from CD and FTIR spectroscopy, where the non-irradiated 72 h incubated sample indicated a much higher β-sheet content than the non-irradiated t_0 sample (though it has to be kept in mind that no DMSO was used for CD measurements).

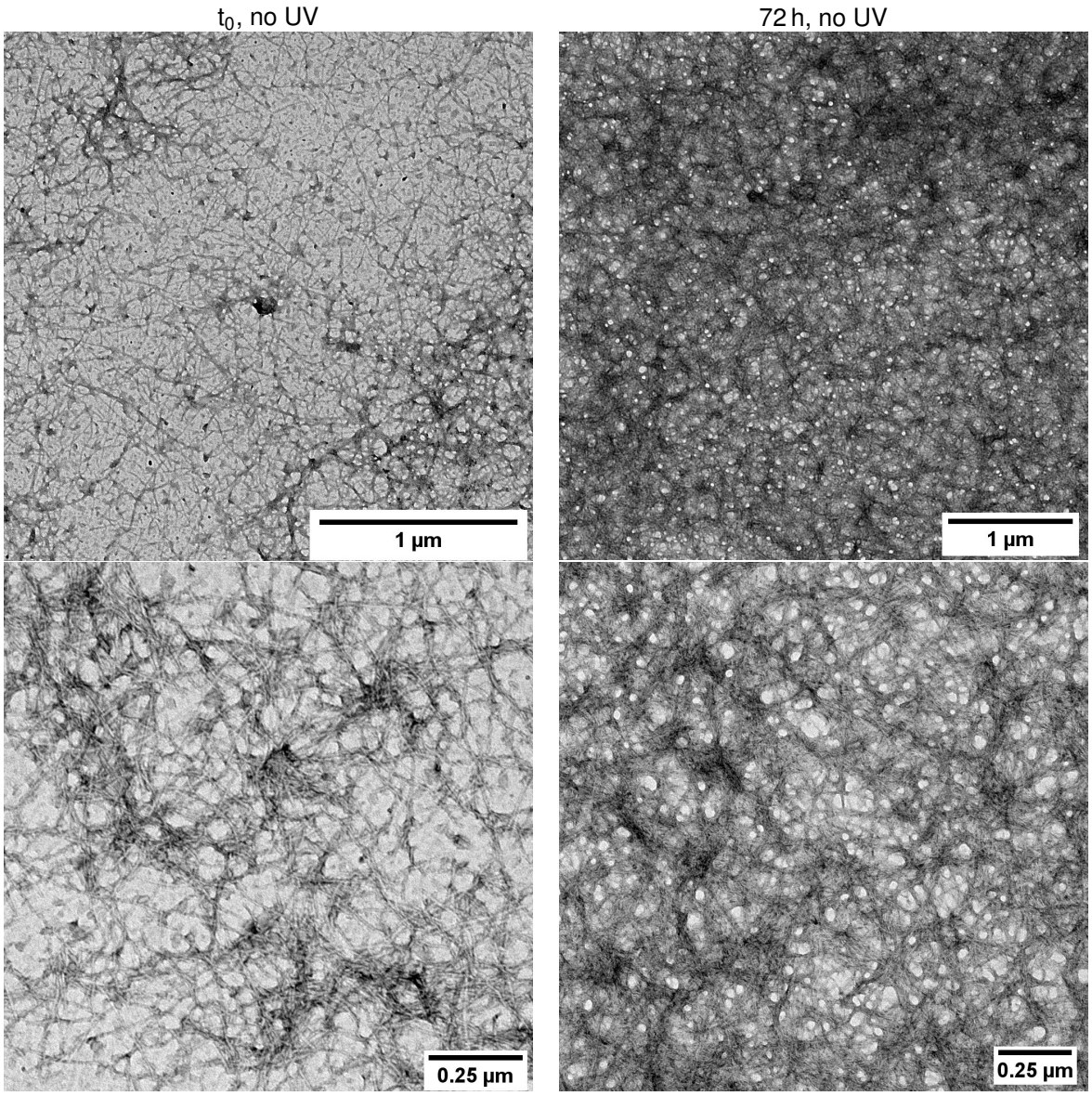

Figure 29: Recorded TEM images for the non-irradiated samples. Images on the left: t_0 without irradiation; Images on the right: 72 h without irradiation.

Figure 30 shows the first two measuring points after irradiation with UV light for 10 min, t_0 +UV and 24 h +UV. Previous analyses showed that despite breakage of the backbone, higher structures stay intact for a certain amount of time. A first glance at the images supported this observation: Directly after the irradiation, intact fibrils could still be found on the grid, the only difference being the area coverage. Prior to irradiation, the fibrous network was very homogenous (Figure 29, left), while the sample measured immediately after irradiation showed gaps of approx. 0.5 µm in diameter (see Figure 30, bottom left) as well as partial aggregation of the fibrils. The same applies for the sample that was prepared 24 h after irradiation. Still, fibrous structures were observed on the grid – now with even larger gaps between the aggregated areas (see Figure 30, bottom right). Additionally, the fibrils seemed to grow less sharp, possibly indicating a weakening of the fibril core structure and therefore a change in morphology (see Figure 30, top right).

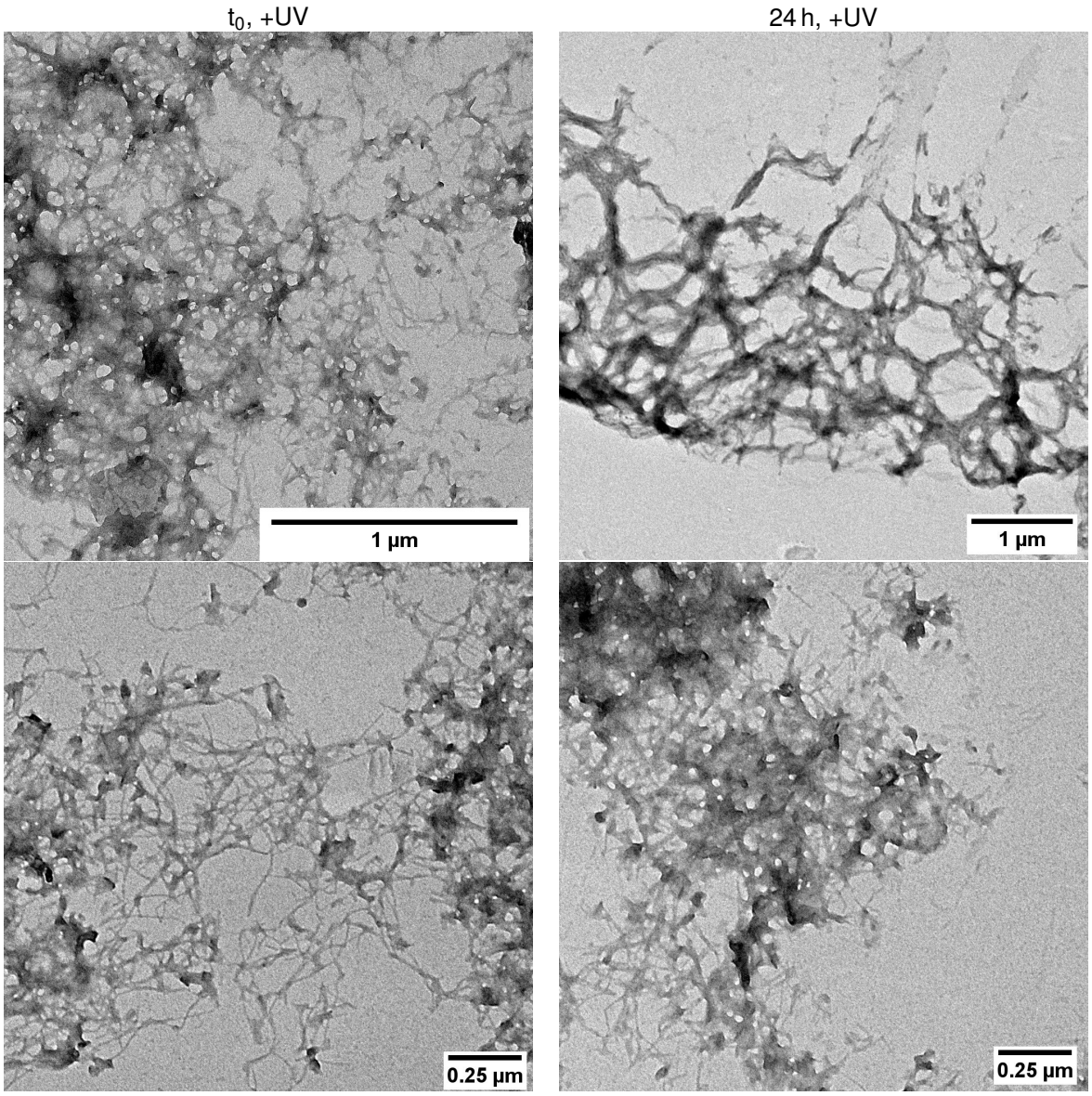

Figure 30: Recorded TEM images for the irradiated samples at t_0 and after 24 h. Images on the left: t_0 with irradiation; Images on the right: 24 h after irradiation.

After 48 h the suspected change in morphology from fibrils to ribbon-like structures was observed (see Figure 31, left). Hints towards a change in morphology after 48 h have already been present for the FTIR measurements. The TEM images could indicate unwinding of the fibrillar structure. Aggeli *et al.* suggested that formation of mature amyloid fibrils of a peptide alternating between hydrophilic and hydrophobic residues is preceded by formation of helical tapes and ribbons. [50] The findings during this study suggest that upon photocleavage of the peptide, this process is reversed. Alternatively, these structures were a result of usage of a broken grid for sample preparation. Repetition of the measurement would be required to safely determine the morphology at this point.

After 72 h of incubation following the irradiation, almost no fibrils could be observed on the grid. The few that could be measured were only present in the form of plaques (see Figure 31, right), indicating that the superstructure almost completely disassembled at this point. It should be noted however, that the 10 min irradiation did not cleave all photolabile linkers (as findings during the HPLC study

suggested), which might explain the few fibers left on the grid.

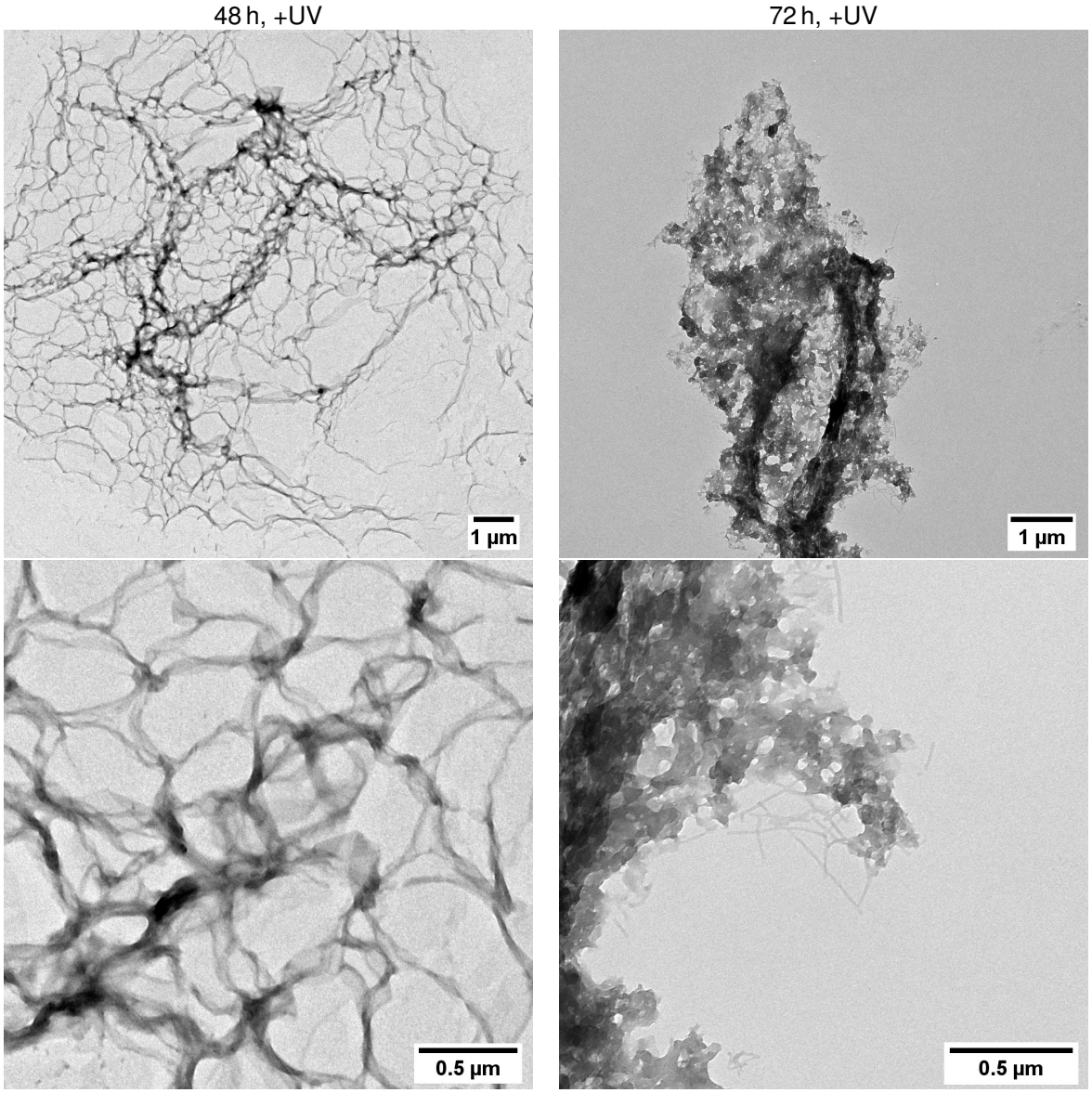

Figure 31: Recorded TEM images for the irradiated samples after 48 h and 72 h. Images on the left: 48 h after irradiation; Images on the right: 72 h after irradiation.

Following the previous findings, two more grids were prepared where the samples were heated to 60 °C for 30 min before or after UV irradiation and measured immediately after. Figure 32 shows the respective images. The sample that was heated prior to irradiation shows a dense network of fibers (see Figure 32, left) as observed for the non-heated and non-irradiated sample that was incubated for 72 h in the dark. This suggests that the elevated temperature and therefore the increased mobility of the peptides accelerated fibril formation. The sample that was heated after the UV irradiation shows almost no fibers on the grid, creating a comparable outcome to the non-heated irradiated 72 h sample. Again, the exposure to heat seemed to have accelerated the process, in this case of the disassembly. Interestingly, the intermediate step of aggregation into plaques seemed to have been skipped, since no such structures but only distinguishable fibrils were observed (see Figure 32, right). This observation might indicate that the energy barrier for the disassembly (i. e. the disruption

of attractive forces) at room temperature is too high and competition with repulsive forces between the fibers (triggered by e. g. the additional charge upon photocleavage) promote a change in morphology as an intermediate step towards full disassembly. Upon heating, the attractive forces may pose less influence due to the increased mobility and the competing repulsive forces cause facile breakdown of the fibrous nanostructure.

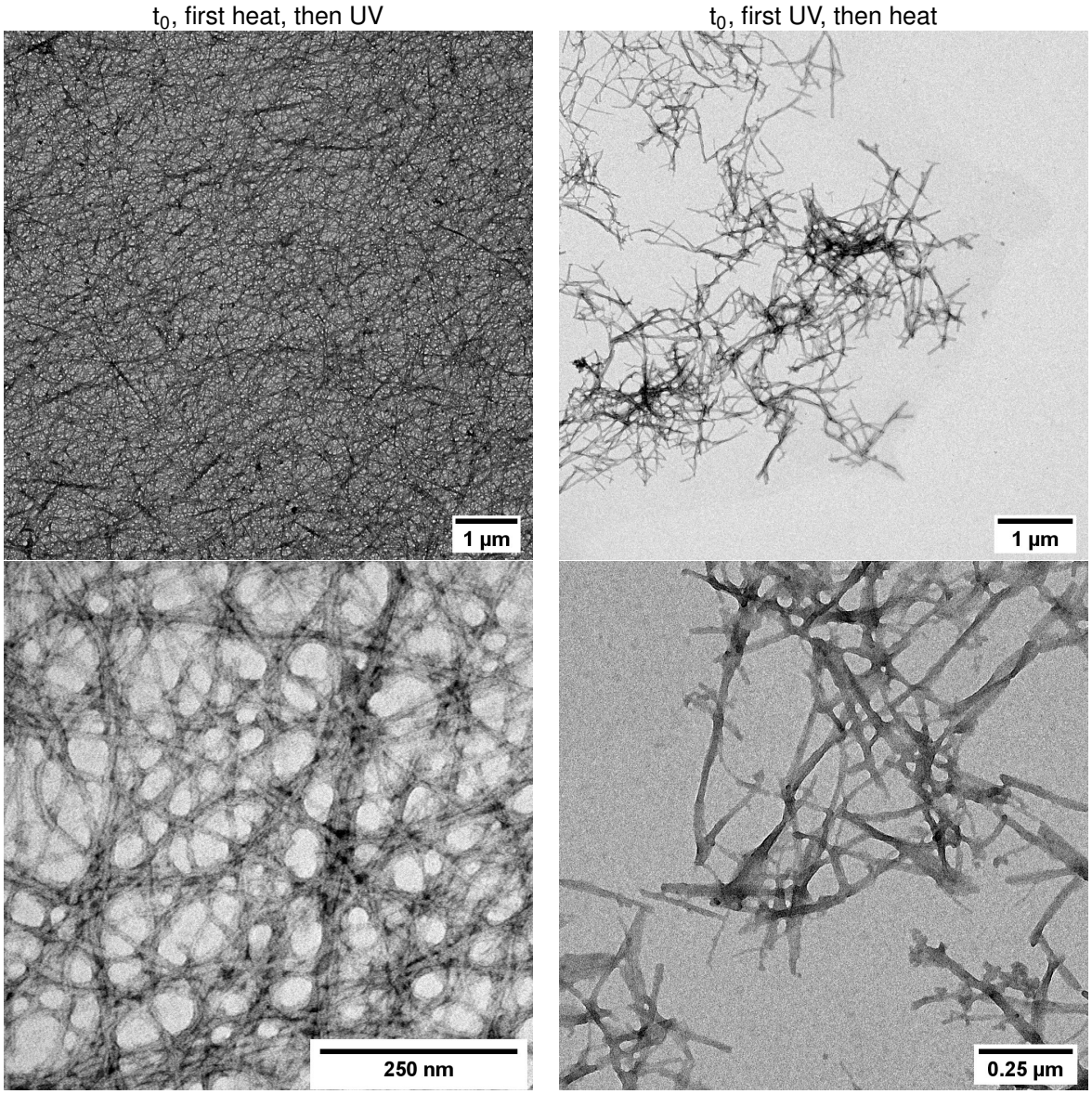

Figure 32: Recorded TEM images for the irradiated samples with heat treatment. Images on the left: first heated then irradiated; Images on the right: first irradiated then heated.

3.4.2.2 AFM Imaging

AFM is another useful tool to investigate fiber disassembly. Images were acquired by Pia Winterwerber. Samples were prepared according to the standard fibrillation procedure (see subsection 4.2.1) and diluted to 0.1 mg mL^{-1} before each measurement. Irradiation was conducted with the 1 mg mL^{-1} solution. The samples were measured in tapping mode in a water droplet. Due to the large timescale observed in the previous analyses, heating of the samples prior to and after UV irradiation was con-

ducted.

Figure 33 shows the recorded images. For the non-irradiated samples (a, b, c), fibers of up to multiple micrometers length and 10 nm–15 nm height were observed. One of the non-irradaited samples was heated to 60 °C for 30 min before dilution and measurement (c). It was assumed that the increased mobility might promote faster formation of a stronger network of fibers as already observed during TEM experiments. However, no significant difference in fiber length or height was observed. Additionally, no significant difference was observed between the t_0 (a) and 48 h sample, which again proves fiber stability in solution.

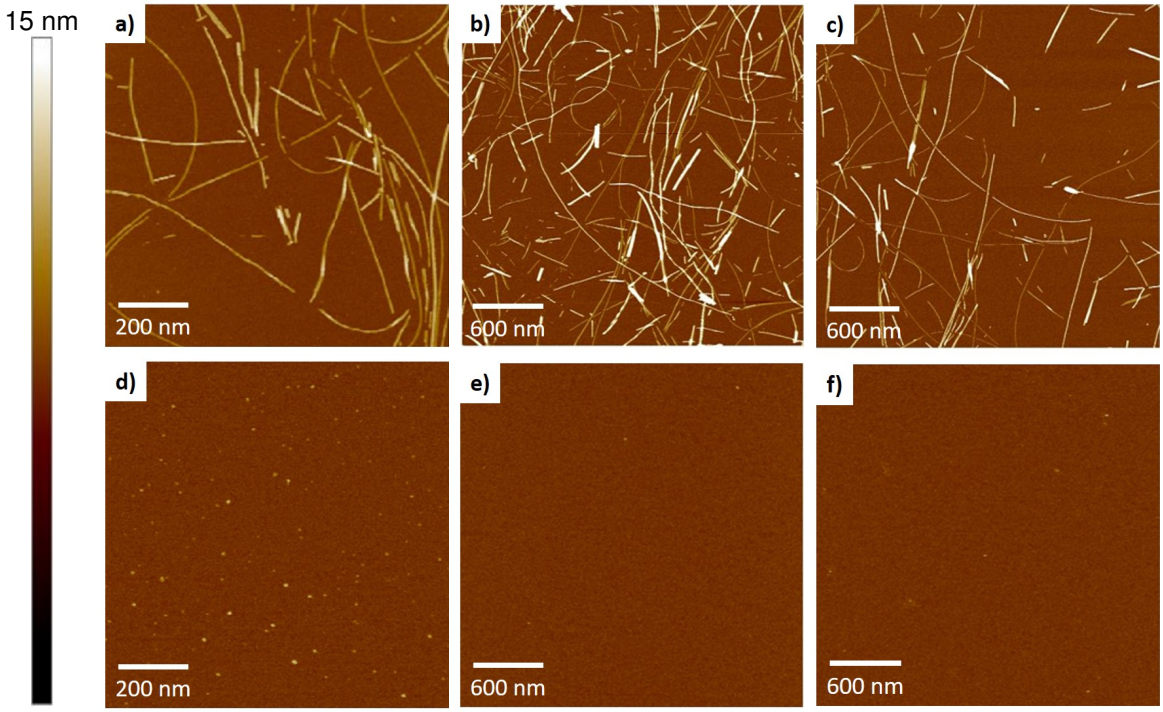

Figure 33: Recorded AFM images in dependence of heat and UV irradiation: a) t_0, no heat, no UV; b) 48 h, no heat, no UV; c) no UV, heat; d) UV, no heat; e) first UV, then heat; f) first heat, then UV.

Immediately after irradiation of the 1 mg mL^{-1} sample solution, no more fibers were found in either one of the samples (d, e, f). Only for the non-heated sample (e), tiny fragments of the same height as the fibers were observed in larger numbers. This contradicts the observation during TEM measurement where even after 24 h fibers were still present on the grid. It was therefore assumed that the photoinduced cleavage prevented adhesion of the fibers to the mica sheet's surface. The surface of the sheet is negatively charged over a wide pH range. [51] Due to its lysine residues, the CKFK-PCL-FQF peptide is overall positively charged and therefore shows a facile adhesion to the surface (as observed for the non-irradiated samples). Upon photocleavage, a carboxylic acid group is uncaged within the backbone of the peptide. A pK_a value of 3.52 was calculated for this group (using *MarvinSketch* Protonation Plugin), showing that the group is negatively charged at pH 7.4. Assuming the *N*- and *C*-terminal groups are charged as well, the overall net charge of the fibril should still be positive. However, the additional negative charge still seems to interfere with adhesion of the fibrils. Therefore, another sample was diluted to 0.1 mg mL^{-1} in a 100 mM $MgCl_2$ buffer to mask negative charges. The resulting picture is shown in Figure 34 (g). Still, no peptide fibrils

could be observed for the irradiated sample, although it should be noted that the influences of the respective buffer on the fibrillation (and already existing fibrils) was not studied during the course of this project. Since salt concentration in general is also an influencing factor in fibril formation and retention, the buffer might have promoted other side-effects (e. g. faster disassembly), which alter the observable image.

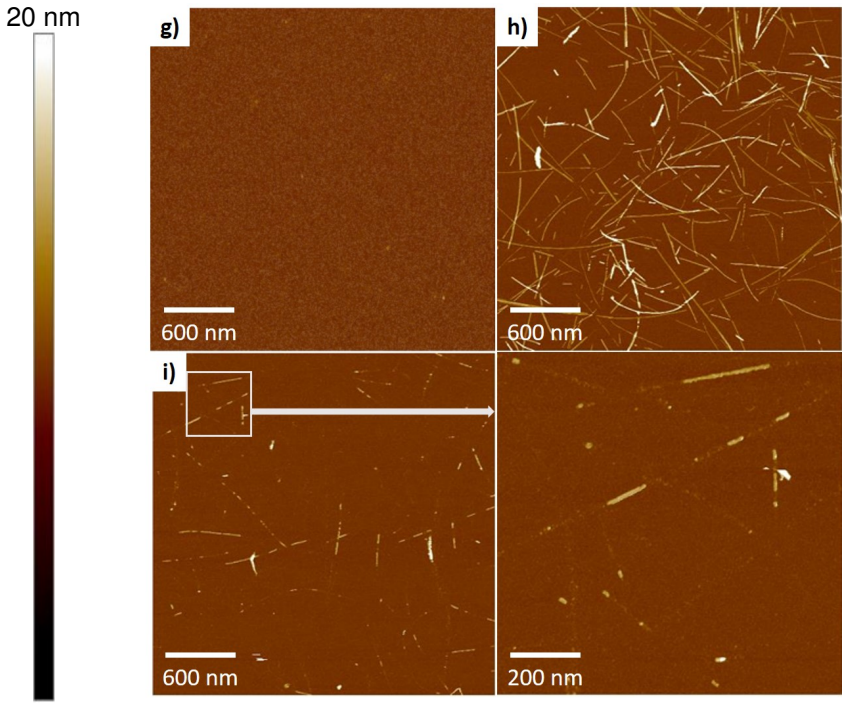

Figure 34: Recorded AFM images in dependence of sample preparation: g) irradiated sample diluted with 100 mM $MgCl_2$ buffer, no heat; h) mica surface before irradiation, no heat; i) sample irradiated directly on mica surface, no heat.

The next step was to irradiate an already measured sample directly on the mica surface. Since the fibrils were already adhered to the mica surface, the interaction might cause further adhesion even after irradiation. Figure 34 shows the resulting images before (h) and after (i) irradiation. Before irradiation, an image similar to other non-irradiated samples could be observed, indicating fibril formation and successful adhesion to the mica sheet as already expected. After irradiation, the fibrils seem to remain attached to the surface only partially. The fibril structure can still be observed, but only as "shadows" of lower height and only some fragments of the fibril height as previously observed. These findings fortify the assumption that the photocleavage hindered adhesion of the fibers, or in this case caused separation from the surface.

Due to the previous observations, the probable change in pH of a sample after incubation and irradiation was briefly investigated. A sample prepared according to the standard fibrillation procedure (see subsection 4.2.1) – initially adjusted to pH 7.41 – showed a drastic decrease in pH by 1.38 to 6.03 after 96 h. The reason behind this might have been the already observed formation of disulfide bonds by the cystein residues in the presence of DMSO. Immediately after 10 min of irradiation, the pH went further down to 5.21, indicating deprotonation of the free carboxylic acid group of fragment CKFKG.

Since fibrils seemed to detach from the mica surface during wet measurements, another sample

was prepared and irradiated by Pia Winterwerber for dry measurements. The 1 mg mL^{-1} samples were diluted to 0.1 mg mL^{-1} with *Milli-Q* H_2O, placed on the mica surface and measured after all solvent evaporated. Subsequently, the 1 mg mL^{-1} solution was irradiated for 10 min and prepared likewise. It has to be noted that during this last sample preparation, a differing setup for irradiation with decreased intensity was used. Thus, comparability to irradiated samples from other measurements is not necessarily given. Figure 35 shows the recorded images before and after irradiation. In contrast to the wet measurements, fibrils were observed for both samples as already observed during the TEM measurements. Additionally, different areas of both samples showed differences in fibril density. This inhomogenous distribution is a typical result of drying effects: as the solvent evaporates, clusters of molecules or nanostructures form within the remaining solvent and only little amounts remain dried on the surface. A very dense fibril network resembling the non-irradiated TEM images (see Figure 29) was observed for the irradiated sample. Due to the differing setup used for irradiation, it cannot be determined whether the observed fibril network is composed of mainly intact or cleaved peptides. Repetition of the measurements with the same irradiation setup as for previous measurements would be required, but could not be conducted within the given timeframe.

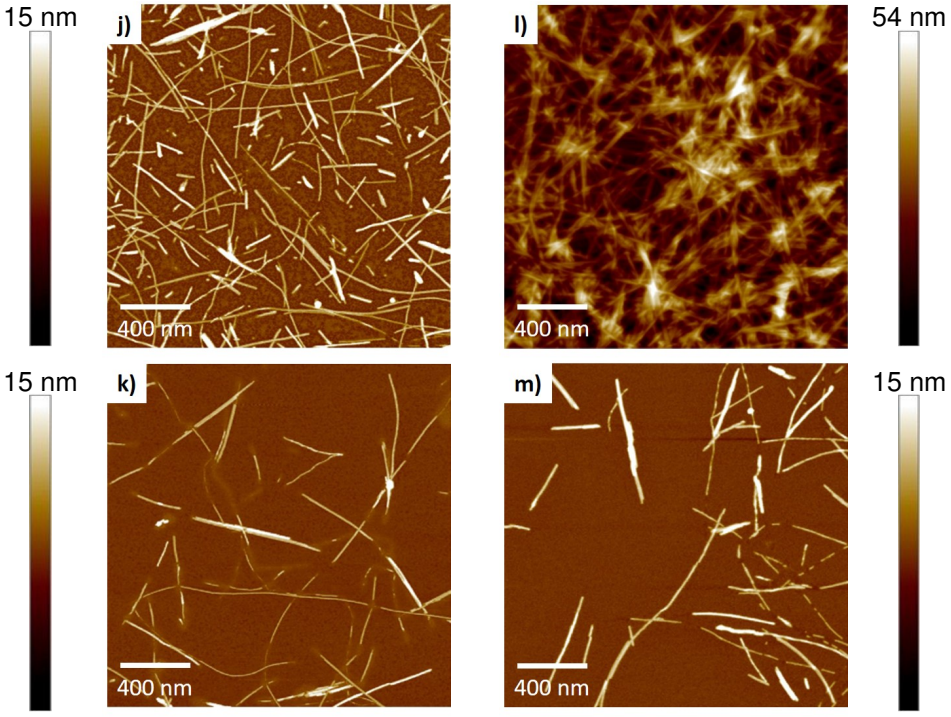

Figure 35: Recorded AFM images in dry measuring mode: j,k) different areas on same non-irradiated sample; l,m) different areas on same irradiated sample.

3.5 Influence on Cellular Adhesion and Toxicity

Due to their ECM-mimicking properties, PNFs are an interesting scaffold for cellular environments, especially when triggermechanisms for assembly and/or disassembly of the scaffolds are available. Thus, the PNF forming peptide CKFK-PCL-FQF was investigated with regard to its influences on cells by Adriana Sobota and the results will be discussed in the following.

3.5.1 Cellular Adhesion on CKFK-PCL-FQF Fibrils

To test cellular adhesion properties, glass slides were dip-coated with agarose and subsequently spray-coated with an 1 mg mL^{-1} fibril solution of CKFK-PCL-FQF. One of the samples was kept in the dark and a second irradiated to observe adhesive properties of the photoinduced fragments. Additionally, another sample was half covered during irradiation to investigate the transition area between irradiated and non-irradiated fibrils. A non-spraycoated agarose slide served as negative control. Adenocarcinomic human alveolar basal epithelial cells (A549 cells) were seeded on the slides and incubated for 24 h at 37 °C. The surfaces were washed with fresh culture medium and imaged with a microscope.

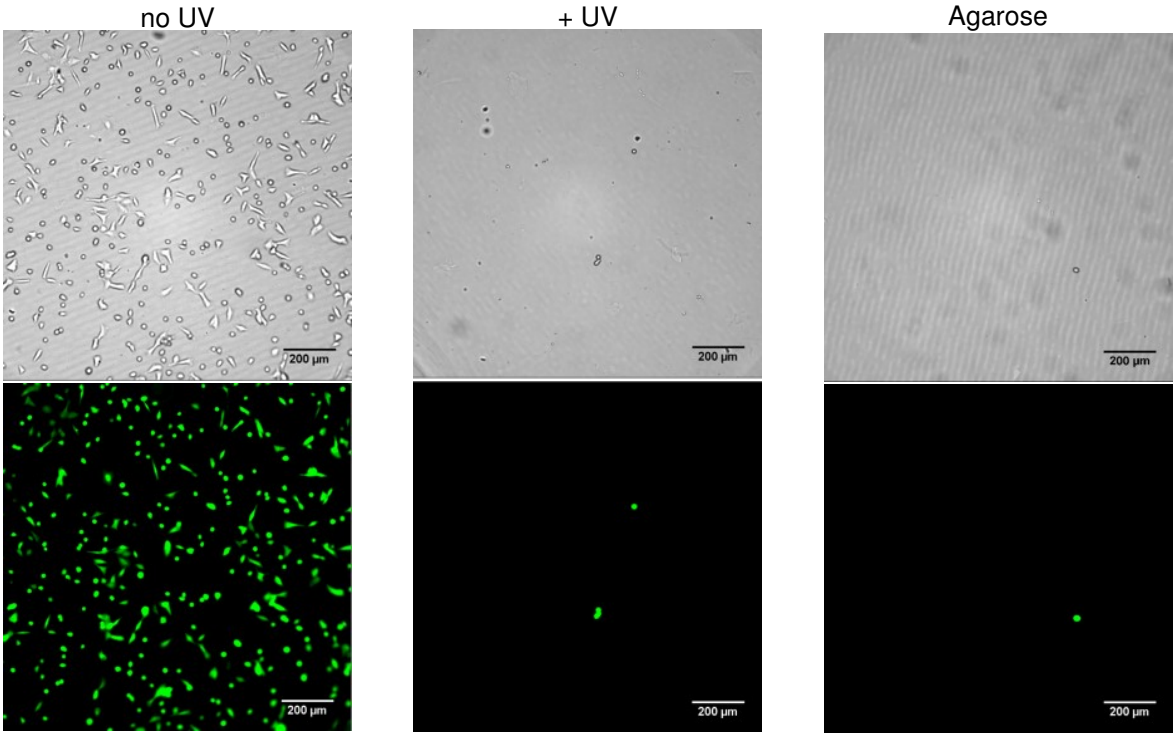

Figure 36: Results of the cell adhesion tests of A549 on CKFK-PCL-FQF fibrils. Left: non-irradiated slides in brightfield (top) and calcein stained (bottom); middle: irradiated slides in brightfield (top) and calcein stained (bottom); right: pure agarose in brightfield (top) and calcein stained (bottom).

Figure 36 shows the recorded images of the cellular adhesion test. As expected, the amyloid fibers of the non-irradiated sample promoted adhesion of A549 cells. This effect of amyloid fibers on peripheral nervous system cells has been studied among the group on various peptides, including CKFKFQF. [12] Some of the cells even showed spreading behaviour, indicating that the CKFK-PCL-FQF fibers provide a suitable surface for the cells. On the other hand, the irradiated slides did not show a significant amount of attached A549 cells. This indicates a rapid breakdown of fibrillar structures, presumably due to the increased mobility at 37 °C during cell incubation (24 h), as previous analyses showed an acceleration in fibril disassembly upon heating to 60 °C for 30 min. A following toxicity test of fibrils and their fragments as well as the single peptides and their fragments was conducted to prove that the cells detached from the surface not due to apoptosis and will be discussed in the next paragraph. The sample that was only partially irradiated (see Figure 37) showed a clear cut between the irradiated and non-irradiated sides, proving that precise control over

the disassembly is given. As expected, the negative control without peptide coating did not show any cellular adhesion.

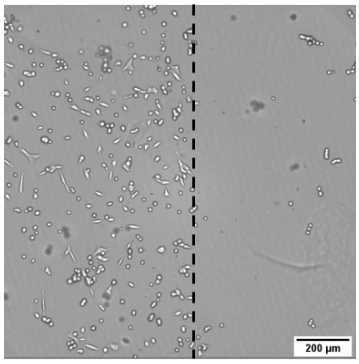

Figure 37: Results of cellular adhesion tests of A549 on CKFK-PCL-FQF fibrils with differing illumination areas in brightfield imaging mode. The left area was covered and the right area uncovered during irradiation.

3.5.2 Cellular Toxicity of Peptides and Fibrils and their Fragments

Cellular toxicity of the preformed fibrils as well as the single molecules and respective fragments was tested *via* a *CellTiter-Glo Assay*. 1 mg mL^{-1} peptide solution (freshly prepared, irradiated and non-irradiated) as well as 1 mg mL^{-1} fibril solution (incubated for 24 h, irradiated and non-irradiated) were diluted to a final concentration of 0.1 mg mL^{-1} in the wells of a 96-well plate (preincubated with cells for 24 h) and incubated for 24 h at 37 °C. Pure culture medium served as positive control, the negative control was prepared with added 1 µM staurosporine to induce apoptosis. The results are displayed in Figure 38.

The high values obtained for all samples except the negative control with 1 µM staurosporine indicate that no cytotoxic behaviour of the intact peptide, its fibrils or respective fragments were existent. Thus, CKFK-PCL-FQF poses a suitable candidate for further tests with regard to bioapplications.

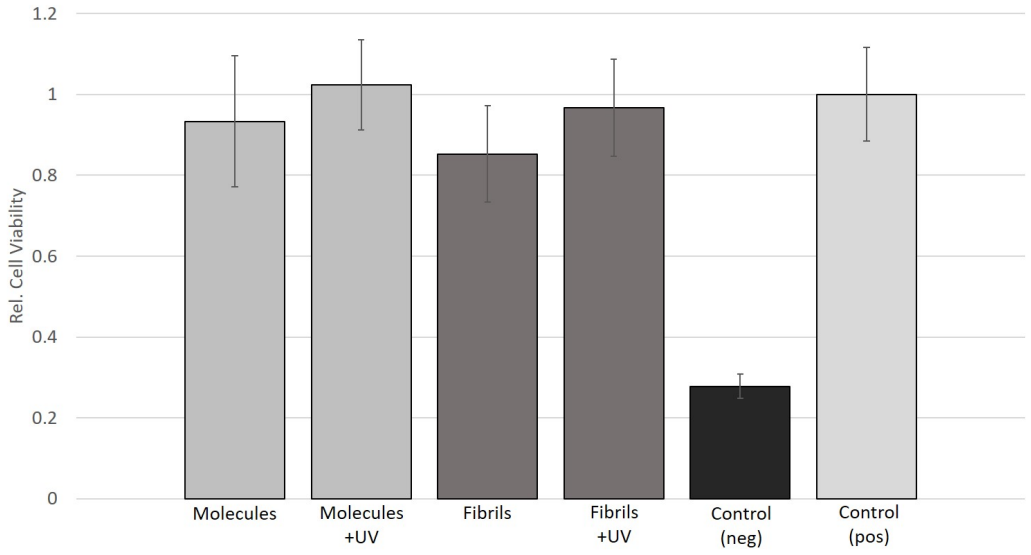

Figure 38: Results of cell viability test of the CKFK-PCL-FQF peptide, its fibrils and respective photocleavage fragments. Results were normalised to the positive control (pure culture medium). Added 1 µM staurosporine was used as negative control.

3.6 Conclusion and Outlook

Kinetics of single molecule cleavage upon irradiation have hinted at a first order decay mechanism with a half-life of 2.8 min for the employed setup. Compared to previous work (irradiation in DMSO, different lamp), the cleavage occured at a significantly slower rate, possibly caused by the differing lamp as well as absorption coeffients of the solvents.
Following investigations of the disassembly behaviour of preformed fibrils in a 1 mg mL^{-1} solution using ThT assays, CD and FTIR spectroscopy as well as TEM imaging indicated stability of the fibrils until at least 24 h after irradiation and a shift in morphology of the fibrils after approx. 48 h. Repetition of the study is required to confirm this morphological shift. Almost complete degradation of the fibrils was observed after 72 h. Furthermore, TEM images showed a further increase in fibril density after 72 h without irradiation, indicating that equilibrium of the assembly was not reached after the initial 24 h incubation period. A deeper investigation of the assembly and its differing states (nucleation/elongation) as well as the respective timeframe could provide information for future measurements. A similar starting point for all methods set to the equilibrium state of fibril assembly would provide reliable and reproducible data. Additional measurements employing heat treatment at 60 °C for 30 min showed that 1) this equilibrium could be reached faster upon heating and 2) the disassembly occured more readily as well. AFM measurements indicated a differing attachment behaviour towards the mica sheet immediately after irradiation, presumably due to an additional charge caused by the cleavage (free carboxylic acid). Measurement of the zeta-potential before and after irradiation as well as imaging in buffer solutions (due to the observed pH changes) would provide additional insight. Another possible cause might be that intact fibrils are needed for attachment. This assumption could be tested by measurements of samples irradiated for e. g. 3 min (close to half-life). Dry measurements resembled the findings in TEM imaging where fibrils stayed intact even after irradiation, though it has to be noted that a differing setup was used.
For higher concentrations in NMR spectroscopy (5 mg mL^{-1}), no disassembly was observed during 96 h following UV irradiation. Some shifts in peak locations could be observed and were interpreted as proof of the disassembly in combination with the yellow colouring of the solution. Presumably, the increased peptide concentration aided in trapping of the fibrils in their intact state. Upon heating the one week old sample to 45 °C, changes in peak sharpness and chemical shift were observed that may be related to disassembly of the fibrils. These findings further strengthened the assumption that a higher concentration slowed the disassembly rate massively. However, additional methods using similar sample concentrations are required to confirm the assumptions and determine the state of the system at the already observed measuring points.

Investigation of the peptide's influence on cellular adhesion showed that CKFK-PCL-FQF fibril-covered agarose slides pose a good attachment ground for A549 cells. Upon irradiation, fibrils broke down rapidly within 24 h of incubation and almost no cellular attachment was observed. The increased disassembly rate was attributed to 1) the increased mobility during incubation with the cells at 37 °C (main contriubution) and 2) the possibly accelerated photocleavage caused by irradiation directly on a surface, leaving no uncleaved linkers. Furthermore, irradiation of only one half of a slide showed a precise cut between irradiated and non-irradiated areas, indicating that fibril disassembly can be precisely controlled depending on the location. Further studies on irradiation

gradients may even show a time-resolved control.
Investigation of the toxicity of CKFK-PCL-FQF, its fibrils and the respective cleavage products showed no negative effects on A549 cells for the employed concentration of 0.1 mg mL^{-1}.

Regarding reproducibility of the used methods and conducted experiments, only few were conducted in multiplicates. Repetition of TEM, AFM, CD, FTIR and NMR measurements was not conducted within the given timeframe and would be required to make a statement on reproducibility. This applies especially to e. g. the TEM image recorded 48 h after the irradiation to confirm the structural change. Regarding reliability, errors for the imaging methods (i. e. TEM and AFM) arise from interpretation of the data rather than fluctuations during the measurements. Since multiple areas of the sample were scanned and showed similar results and the sample preparation was kept consistent throughout the study, the imaging methods are expected to be the most reliable. For FTIR measurements differing coverage of the ATR crystal could have caused differing absolute absorbances, which can complicate correct interpretation of the spectra. Additionally, frequencies of vibrational modes can overlap each other and correct assignment of bands can therefore be difficult. CD specta represent mixed contributions of all secondary structure elements and need to be deconvoluted for determination of precise secondary structure ratios. Since it is not known which influence the photocleavable linker had on the spectrum and deconvolution *via* respective software led to unrealistic results (e. g. 127 % β-sheet content), the spectra were only interpreted qualitatively and are not as reliable as other methods.
ThT measurements of the setup without heat treatment were conducted twice (and both times in triplicates) with similar results, showing reproducibility of the method. However, regarding reliability of the assay, the variation in fluorescence resulting in large error bars (up to 21 % relative error) indicated that the method is rather unreliable and requires additional methods for validation. Slides for the adhesion of A549 cells were prepared in biological quadruplicates and the viability assay in sextuplicates, all of which produced similar results, respectively. Thus, the cell experiments show a high reproducibility and therefore a good reliability.

A deeper investigation of the association and dissociation mechanics of the fibrils presented during this work may be required to pave the way for possible applications. Due to the differences in fibrillation behaviour in presence of DMSO, CD and NMR cannot be directly compared to the other methods and would require supplemental measurements without DMSO. Addition of e. g. dithiothreitol (DTT) to prevent formation of disulfide bridges in presence of DMSO could be used to prove whether this mechanic is essential for fibril formation. Additionally, dynamic light scattering (DLS) may pose an interesting tool for the investigation of higher-order structures in solution and the solvent-related differences.
The dissociation behaviour on surfaces has not been investigated thoroughly during this work and may provide additional insight on thermodynamics of the system. Scanning electron microscopy (SEM) and MALDI imaging as well as further dry AFM measurements (irradiation on the surface) may be used to investigate differing kinetics compared to solution.
Since cell tests already showed no toxic behaviour of CKFK-PCL-FQF as well as its fibrils and respective fragments, and cellular adhesion on surfaces coated with CKFK-PCL-FQF fibers was successful, alignment of the fibers may pose an interesting approach to direct cellular growth of e. g.

neurons. Orientation of the nanofibers along a common axis using different external forces (magnetic, thermal, ultrasonication) and methods (Langmuir deposition, zone casting) as well as fixation of these scaffolds would be needed to allow for further analyses. An easily accessible method for fixation is the already used deposition on surfaces thus creating an aligned 2D environment. Current work within the group of Prof. Dr. Tanja Weil focuses on alignment of PNF on surfaces *via* zone casting, which may be applicable for the peptide investigated during this work. Further on, it may be interesting to take a look at 3D immobilisation as it much more resembles the naturally occurring systems within organisms. 3D immobilisation would however involve differing setups like scaffolds that harden upon cooling (e. g. agarose gel). Still, it should as well be kept in mind that the photodegradation system investigated during this work requires some degree of movement to promote dissociation of the fibers, rendering 3D fixation a difficult task.

4 Experimental Part

4.1 General Methods and Materials

Unless stated otherwise, all chemical compounds used for synthesis were acquired commercially (*Sigma Aldrich, Thermo Fisher Scientific, Merck*) and used without further purification. The control peptide (CKFKFQF) was acquired commercially.

4.1.1 Thin Layer Chromatography

Purity and reaction progress were checked by TLC using ALUGRAM® Xtra SIL G/UV_{254} plates from *Macherey-Nagel GmbH & Co. KG* (detection at λ = 254 nm and 365 nm).

4.1.2 Column Chromatography

The synthesised compounds were purified *via* column chromatography using Silica 60 M (particle size 0.04 mm–0.063 mm) from *Machery-Nagel GmbH & Co. KG*. Solvents were acquired commercially in analytical reagent grade purity. The composition of the mobile phase is stated in volume shares (v:v) in the following.

4.1.3 High Performance Liquid Chromatography

HPLC was run with *Milli-Q*-water and acetonitrile (ACN) each with 0.1 vol% TFA. Gradients were applied according to the used device (see below). Commercially available solvents in HPLC grade purity were used.

Sample Preparation (Analytical HPLC): A 1 mg mL^{-1} *Milli-Q* H_2O solution of the peptide was prepared. Further incubation and irradiation of the samples was varied as required.

Analytical HPLC: Device by *Shimadzu* equipped with DGU-$20A_{5R}$, LC-20AP (2x), CBM-20A, SPD-M20A, SIL-10AP, FRC-10A.
Column: Agilent ZORBAX Eclipse XDB-C18, 80 Å, 5 µm, 9.4 x 250 mm; Agilent Safety Guard Kit
Flow rate: 4 mL/min

Sample Preparation (Preparative HPLC): The peptide was dissolved in *Milli-Q* H_2O + 0.1 % TFA and filtered through a syringe filter (Whatman® GD/X, ∅ 13 mm, 0.2 µm polyether sulfone (PES) membrane, non-sterile) before injection.

Preparative HPLC: Device by *Shimadzu* equipped with DGU-$20A_{5R}$, LC-20AT, CBM-20A, CTO-20AC, SPD-M20A, SIL-20AC, FRC-10A.
Column: Phenomenex Gemini® 5 µm NX-C18, 110 Å, 150 x 30 mm; Phenomenex® AJ0-8277 pre-column
Flow rate: 25 mL/min

Table 4: Gradients used during HPLC

Analytical		Preparative	
Time / min	**% ACN**	**Time / min**	**% ACN**
1.00	5	5.00	0
16.00	100	35.00	40
18.00	100	40.00	100
22.00	5	45.00	100
25.00	5	50.00	0
		55.01	0

4.1.4 Solid Phase Peptide Synthesis

The peptides were synthesised in a microwave-equipped *Liberty Blue Automated Peptide Synthesizer* by *CEM* from C to N terminus according to fluorenylmethyloxycarbonyl (Fmoc) SPPS strategy by *Merrifield*. *N,N'*-diisopropylcarbodiimide (DIC) and ethyl cyano(hydroxyimino)acetate (Oxyma) were used as activator and base, a piperidine solution (20 vol% in *N,N'*-dimethylformamide (DMF)) was used for deprotection and DMF as the main washing agent (see Table 5). The preloaded polystyrene (PS) based Fmoc-*L*-Phe-Wang resin (*Novabiochem*®, loading: 0.68 mmol/g, 100–200 mesh) and side-chain functionality protected *L*-amino acids were used for coupling. Depending on the reaction scale, reagents were prepared as suggested by *CEM* in the *Liberty Blue™ User Guide* (Revision 4, see Table 5).

Table 5: Concentrations of reagents used during automated peptide synthesis depending on the synthesis scale

Reagents	**0.05 mmol**	**0.1-5.0 mmol**
Wash Solvent	DMF	DMF
Deprotection Cocktail	20 % Piperidine in DMF	20 % Piperidine in DMF
Amino Acids	0.2 M in DMF	0.2 M in DMF
Activator	0.25 M DIC in DMF	0.5 M DIC in DMF
Base	0.5 M Oxyma in DMF	1.0 M Oxyma in DMF

Sample cleavage: To test progress of the reaction, a few resin beads were placed in TFA and shaken for 30 min. A few drops of *Milli-Q* H_2O were added until the solution turned colourless. The sample was then analysed *via* MALDI-TOF-MS.

Final cleavage: The resin was placed in a 10 mL polypropylene syringe reaction vessel and swelled in DMF for an hour prior to the cleavage. The solvent was removed by suction through the filter and cleavage of the peptide from the resin was conducted following the protocol provided by *Iris Biotech GmbH*: The resin was shaken for 2 h in a solution of TFA (95.0 %), triisopropyl silane (TIPS) (2.5 %) and *Milli-Q* H_2O (2.5 %). 5 mL cleavage cocktail were used on 0.1 mmol scale. Deprotection of the side-chains occured simultaneously.

4.1.5 Nuclear Magnetic Resonance Spectroscopy

The spectra were acquired using *Bruker Avance III 250*, *Bruker Avance 300* and *Bruker Avance III 700*. Deuterated solvents ($CDCl_3$, D_2O) were acquired commercially from *Sigma Aldrich*. For water suppression, samples were prepared in a 15 % D_2O in H_2O mixture.

4.1.6 Mass Spectrometry

Progress of the reaction (especially during peptide synthesis) was analysed with MALDI-TOF-MS using a *Waters MALDI SYNAPT G2-Si HDMS*.

Levels of purity were analysed by LC-MS using a *Shimadzu LCMS-2020 Single Quadrupole MS* equipped with a *Kinetex® EVO C18* column (2.6 µm, 100 Å) run with *Milli-Q*-water and ACN each with 0.1 vol% formic acid (FA) (5 %–95 % ACN, 20 min). Samples were prepared as 1 mg mL^{-1} solutions in *Milli-Q* H_2O and further diluted to 50 µg L^{-1} with 0.1 % formic acid in *Milli-Q* H_2O prior to the measurements.

4.2 Morphology Analyses

For the analyses, preformed fibril solutions were measured before irradiation and after 10 min of irradiation at t= 0, 24, 48 and 72 hours. An additional sample was measured after 72 h of incubation without irradiation.

4.2.1 Fibril Formation Standard Procedure

A stock solution of 10 mg mL^{-1} peptide in DMSO was prepared. The stock solution was diluted to a concentration of 1 mg mL^{-1} with *Milli-Q* H_2O and the pH was adjusted with aqueous 0.2 M NaOH and 0.1 M HCl solutions to 7.40$\pm$0.40. The solution was incubated at room temperature for 24 h while shaking to induce fibril formation.

4.2.2 Irradiation of Samples

The incubated 1 mg mL^{-1} fibril samples were irradiated for 10 min utilising a *LUMATEC SUPERLITE S04* lamp at a wavelength range of 320 nm–400 nm (2100 mW, 10 500 mW cm^{-2}) equipped with a THORLABS COP2-A Collimation Adapter for LEICA DMI (antireflection coating: 350 nm–700 nm). Open sample vials were placed 2.5 cm below the collimator.

4.2.3 Thioflavin T Assay

Device: *Spark 20M* (Application: *SparkControl* V2.3)

Sample preparation: Fibril Formation Standard Procedure

Well preparation: 10 µL of a 50 µM ThT solution were placed in wells of a *Greiner* 384-well black polystyrene microtiter plate. 2 µL of the sample were added to the wells. After 10 min–15 min of incubation the samples were measured at 488 nm (excitation at 440 nm, bandwidth: 10 nm). Samples were measured in triplicate.

4.2.4 CD Spectroscopy

Device: *JASCO J-1500 CD Spectrometer*, Detector: PM-539

Sample preparation: A 1 mg mL^{-1} solution of the peptide in *Milli-Q* H_2O was prepared, adjusted to a pH of 7.4 using 0.2 M and incubated for 24 h to induce fibril formation.

Measurement: Samples were further diluted to 0.2 mg mL^{-1} with *Milli-Q* H_2O before the measurements. 200 µL sample solution were added to a 1 mm quartz cuvette and measured at room temperature from 180 nm–260 nm. Bandwidth was set to 1.00 nm with a response at 4 s. Standard sensitivity with 0.2 nm data pitch and 100 nm min^{-1} scanning speed was used. Data was accumulated over 3 runs.

4.2.5 FTIR Spectroscopy

Device: *Bruker Tensor II*

Sample preparation: Fibril Formation Standard Procedure. 200 µL (200 µg peptide) of the fibril solution were freeze-dried in 2.0 mL *Eppendorf* tubes at the selected measuring points.

Measurement: A few crystals of the dried samples were placed on the ATR diamond crystal of the device and covered and fixated with a glass slide. Spectra were collected at 2 cm^{-1} resolution within the range of 400 cm^{-1}–4000 cm^{-1} and averaged over 40 scans.

4.2.6 Transmission Electron Microscopy

Device: *JEOL 1400*

Sample preparation: Fibril Formation Standard Procedure

TEM grid preparation: The TEM grids (*plano* GmbH, art. no. S162-3, Formvar/coal film on 3.05 mm Cu grids, 300 mesh) were plasma cleaned prior to sample application. 4 µL of the prepared 1 mg/mL sample solution was pipetted onto the grid, incubated for 5 min and the exess liquid removed using a filterpaper. The grid was then placed on a drop of 1 % uranyl acetate solution, incubated for 2.5 min and subsequently washed with water (3x). The dried TEM grids were then analysed.

4.2.7 Atomic Force Microscopy

Device: *Bruker Dimension FastScan Bio* (PeakForce Mode)

Sample Preparation: Fibril Formation Standard Procedure

Measurement: AFM probes with a nominal spring constant of 0.25 N^{-1} m (FastScan-D, *Bruker*) were used. The samples were further diluted with *Milli-Q* H_2O to a concentration of 0.1 mg mL^{-1}. 30 µL of the sample solution was added onto a freshly cleaved mica substrate (circular, 15 mm diameter) and incubated for at least 15 min to allow deposition of the structures. 300 µL *Milli-Q* H_2O was added onto the mica surface to form a droplet for measuring in liquid. Alternatively, samples were left to dry for dry measurements. The samples were scanned with scan rates between 1.4 Hz–2.0 Hz and scan sizes between 1 µm–3 µm. Images were processed with *NanoScope Analysis 1.8*.

4.2.8 Cell Adhesion Test

Sample preparation: Fibril Formation Standard Procedure

Glass slides (diameter: 12 mm) were dip-coated with a 1 % agarose solution (0.3 g agarose in 30 mL *Milli-Q* H_2O, heated to boiling) and dried over night. 500 µL fibril solution (prepared according to standard procedure) were diluted to 0.1 mg mL^{-1} with *Milli-Q* H_2O. Approx. 40 agarose-coated slides were spray-coated (airbrush gun) with the fibril solution (0.3 mg peptide on 2 petridishes). 4 slides were irradiated for 10 min, 4 kept in the dark and 4 non-spray-coated slides were kept as a negative control. 6 mL of a 100000 cells/mL A549 cells solution were added to the slides and incubated for 24 h at 37 °C. Glass slides were transferred into fresh cell culture medium (4.5 g L^{-1} Glucose/Glutamin supplemented with 1 % penicillin/streptavidin, 10 % FBS, 1 % MEM NEAA) after the incubation and incubated for 10 min–15 min with calceine solution. The samples were viewed on a *Leica* DM2500 Microscope coupled to a *Leica* DFC2000GT camera (brightfield). Calceine staining was conducted by addition of 1 mL of a 1 mg mL^{-1} Calceine AM solution to the medium and subsequent incubation for 30 min. Images were recorded using a FITC filter (emission: 527/30 nm, excitation: 480/40 nm) and processed with ImageJ.

4.2.9 Cell Viability Assay

Sample Preparation: Fibril solution: Fibril Formation Standard Procedure; Molecule solution: A 10 mg mL^{-1} stock solution of the peptide in DMSO was diluted with *Milli-Q* H_2O to a concentration of 1 mg mL^{-1}. The pH was adjusted to 7.4. The sample was used without further incubation. Samples were irradiated for 10 min as required.

Cell viability in presence of peptide nanofibers was tested using a *CellTiter-Glo Assay* (Promega G7571). Cells were seeded with a density of 18000 cells/mL in 96-well plates before treatment and incubated for 24 h. 5 µL of the prepared samples were added to 45 µL cell culture medium to a final concentration of 0.1 mg mL^{-1}. 1 µM staurosporine was added for a negative control, pure cell culture medium served as positive control. The plates were incubated for 24 h at 37 °C. The wells were washed with DPBS and the *CellTiter-Glo Assay* was performed according to manufacturer's instructions. Luminescence was detected using a *GloMax* Multi 96-well plate reader (*Promega*). All samples were measured in sextuplicates.

4.3 Synthesis of photocleavable linker PCL-VII

The photocleavable linker was synthesised according to a procedure by Sur *et al.* [31].

4.3.1 Ethyl 4-(4-acetyl-2-methoxyphenoxy)butanoate (PCL-I)

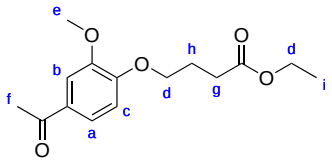

Ethyl-4-bromobutyrate (7.80 g, 40 mmol) was dissolved in DMF (50 mL). Acetovanillone (8.31 g, 50 mmol, 1.25 equiv.) and K_2CO_3 (13.13 g, 95 mmol, 2.4 equiv.) were added and the mixture was stirred overnight at room temperature. The solution turned yellow. Water (40 mL) was added and the mixture was extracted with EtOAc (2 $\times$ 40 mL). The combined organic layers were washed with water (4 $\times$ 25 mL), and brine (25 mL). Drying over $MgSO_4$ was followed by evaporation of the solvent under reduced pressure to afford a slightly yellow powder in 98 % (11.00 g, 39.2 mmol) yield.

^{1}H-NMR (300 MHz, $CDCl_3$): δ 7.59–7.48 (m, 2 H, a, b), 6.89 (d, J = 8.2 Hz, 1 H, c), 4.15 (td, J = 6.7 Hz,5.0 Hz, 4 H, d), 3.91 (s, 3 H, e), 2.59–2.48 (m, 5 H, f, g), 2.26–2.11 (m, 2 H, h), 1.25 ppm (t, J = 7.1 Hz, 3 H, i).

4.3.2 Ethyl 4-(4-acetyl-2-methoxy-5-nitrophenoxy)butanoate (PCL-II)

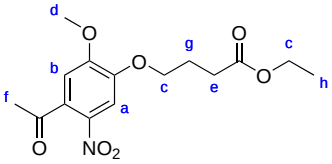

PCL-I (9.00 g, 32.11 mmol) was dissolved in acetic anhydride (150 mL) and cooled to 0 °C on an ice bath. 65 % HNO_3 (5.72 mL, 83.48 mmol, 2.6 equiv.) was added dropwise over the course of two minutes. The reaction was quenched by pouring into ice water (1500 mL) after the solution turned light brown and TLC showed conversion of the starting material (approx. 30 min). A light yellow percipitate crashed out and the mixture was stirred for further 30 min before filtration. The solid residue was taken up in dichloromethane (DCM) (200 mL) and washed with saturated aqueous $NaHCO_3$ solution (3 $\times$ 150 mL) and brine (150 mL). The organic phase was dried over $MgSO_4$ and the solvent was removed under reduced pressure to obtain a yellow-ish powder in 72 % (7.54 g, 23.18 mmol) yield.

^{1}H-NMR (300 MHz, $CDCl_3$): δ 7.61 (s, 1 H, a), 6.75 (s, 1 H, b), 4.25–4.07 (m, 4 H, c), 3.96 (s, 3 H, d), 2.54 (t, J = 7.2 Hz, 2 H, e), 2.49 (s, 3 H, f), 2.26–2.14 (m, 2 H, g), 1.27 ppm (t, J = 7.1 Hz, 3 H, h).

4.3.3 4-(4-acetyl-2-methoxy-5-nitrophenoxy)butanoic acid (PCL-III)

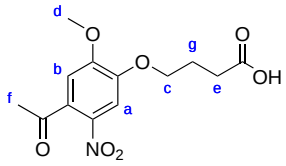

PCL-II (7.54 g, 23.18 mmol) was suspended in ethanol (100 mL). 1 M aqueous NaOH solution (35 mL, 35 mmol, 1.5 equiv.) was added and the solution was stirred at 40 °C for 1 h and changed color to a dark red. The solvent was removed under reduced pressure and the aqueous residue was taken up in saturated aqueous $NaHCO_3$ (50 mL) and washed with DCM (3 × 50 mL). The aqueous layer was acidified to pH 1 using concentrated aqueous HCl solution crashing out a light brown-ish precipitate. The mixture was extracted with DCM (3 × 200 mL) and the combined organic layers were washed with 0.5 M aqueous HCl solution (2 × 100 mL). The organic layer was dried over $MgSO_4$ and the solvent was removed under reduced pressure. Recrystallisation from MeOH/$CHCl_3$ afforded a light yellow powder in 66 % yield (4.55 g, 15.30 mmol).

^{1}H-NMR (300 MHz, $CDCl_3$): δ 7.62 (s, 1 H, a), 6.75 (s, 1 H, b), 4.18 (t, J = 6.1 Hz, 2 H, c), 3.96 (s, 3 H, d), 2.63 (t, 2 H, e), 2.50 (s, 3 H, f), 2.28–2.15 ppm (m, 2 H, g).

4.3.4 *tert*-Butyl 4-(4-acetyl-2-methoxy-5-nitrophenoxy)butanoate (PCL-IV)

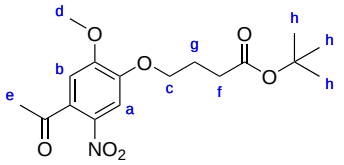

PCL-III (2.73 g, 9.19 mmol) was suspended in a *t*BuOH/THF solution (3:1 v/v, 80 mL). After addition of DMAP (337 mg, 2.76 mmol, 0.3 equiv.), Boc_2O (6.02 g, 27.58 mmol, 3.0 equiv.) was added portionwise over 1.5 h. When bubbling was observed, a septum pierced with a needle was placed on the flask. The mixture was left to stir overnight until TLC indicated complete conversion. The solvent was removed under reduced pressure and the orange residue was redissolved in DCM (50 mL). After washing with 0.2 M HCl (2 × 25 mL), saturated aqueous $NaHCO_3$ (3 × 25 mL) and brine (25 mL), the organic layer was dried over $NaSO_4$. Removal of the solvent under reduced pressure yielded an orange solid. Further purification by a plug of silica (2 % MeOH in DCM) afforded a yellow powder in 96 % (3.12 g8.82 mmol) yield.

^{1}H-NMR (250 MHz, $CDCl_3$): δ 7.61 (s, 1 H, a), 6.75 (s, 1 H, b), 4.19–4.04 (m, 2 H, c), 3.95 (s, 3 H, d), 2.53–2.40 (m, 5 H, e, f), 2.21–2.07 (m, 2 H, g), 1.46 ppm (s, 9 H, h).

4.3.5 *tert*-Butyl 4-(4-(1-hydroxyethyl)-2-methoxy-5-nitrophenoxy)butanoate (PCL-V)

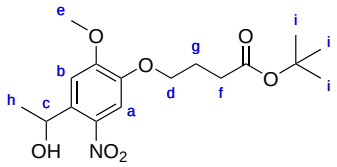

PCL-IV (3.00 g, 8.49 mmol) was suspended in EtOH (50 mL). $NaBH_4$ (652 mg, 17.23 mmol, 2.03 equiv.) was added and left to stir overnight under argon atmosphere. The mixture turned from orange to red colour. The reaction was quenched with aq. citric acid solution (600 mg mL^{-1}) until the pH reached 4. A yellow participate crushed out and the solution turned light brown. The mixture was diluted with DCM (70 mL) and water (35 mL) and the organic layer was washed with brine (50 mL) and dried over Na_2SO_4. The solvent was removed under reduced pressure to obtain a viscous orange oil in 99 % (2.99 g, 8.41 mmol) yield.

^{1}H-NMR (250 MHz, $CDCl_3$): δ 7.56 (s, 1 H, a), 7.29 (s, 1 H, b), 5.61–5.49 (m, 1 H, c), 4.09 (t, J = 5.0 Hz, 2 H, d), 3.97 (s, 3 H, e), 2.44 (t, J = 6.8 Hz, 2 H,f), 2.21–2.03 (m, 2 H, g) 1.55 (d, J = 5.4 Hz, 3 H, h) 1.46 ppm (s, 9 H, i).

4.3.6 *tert*-Butyl 4-(4-(1-(2-(Fmoc-amino)acetoxy)ethyl)-2-methoxy-5-nitrophenoxy)-butanoate (PCL-VI)

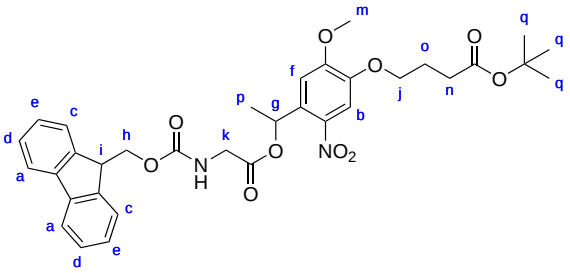

Fmoc-Gly-OH (3.89 g, 13.08 mmol, 1.55 equiv.) was suspended in dry DCM (25 mL). EDC · HCl (2.91 g, 15.19 mmol, 1.80 equiv.) and DMAP (103 mg, 544 µmol, 0.1 equiv.) were added and the solution was stirred for 5 minutes until it was clear. **PCL-V** (3.00 g, 8.44 mmol) was dissolved in DCM (15 mL), added to the solution and left to stir for 4 h at room temperature. After completion, the reaction mixture was washed with water (2 × 50 mL), sat. aq. $NaHCO_3$ (50 mL) and brine (50 mL). The organic layer was dried over $NaSO_4$ and the solvent was evaporated under reduced pressure. The crude product was purified by column chromatography (silica, Hexane/EtOAc 5/3, product eluted with 4 % MeOH in DCM) to obtain an orange oil in 32 % (2.66 g, 4.19 mmol) yield.

^{1}H-NMR (300 MHz, $CDCl_3$): δ 7.76 (d, J = 7.4 Hz, 2 H, a) 7.64–7.54 (m, 3 H, b, c), 7.38 (dd, J = 15.9, 8.6 Hz, 2 H, d), 7.35–7.24 (m, 2 H, e), 7.04 (s, 1 H, f), 6.58 (dd, J = 12.1, 5.8 Hz, 1 H, g), 4.46–4.31 (m, 2 H, h), 4.26–4.16 (m, 1 H, i), 4.12–4.00 (m, 4 H, j, k, l), 3.96 (s, 3 H, m), 2.47 (t, J = 7.1 Hz, 2 H, n), 2.20–2.09 (m, 2 H, o), 1.67 (d, J = 6.2 Hz, 3 H, p) 1.49 ppm (s, 9 H, q).

4.3.7 4-(4-(1-(2-(Fmoc-amino)acetoxy)ethyl)-2-methoxy-5-nitrophenoxy)butanoic acid (PCL-VII)

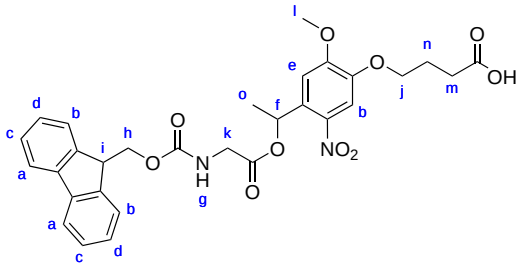

PCL-VII (2.66 g, 4.19 mmol) was dissolved in 15 % TFA in DCM (24 mL) and stirred for 4 h at room temperature. The solvent was removed in vacuo and the residue was taken up in DCM (18 mL) and washed with 0.5 M HCl (2 × 24 mL) and brine (24 mL). The organic layer was dried over Na_2SO_4 and the solvent was removed under reduced pressure to obtain a yellow powder in 90 % (2.18 g, 3.77 mmol) yield.

^{1}H-NMR (300 MHz, $CDCl_3$): δ 7.75 (d, J = 7.3 Hz, 2 H, a) 7.63–7.53 (m, 3 H, b), 7.39 (t, J = 6.9 Hz, 2 H, c), 7.35–7.22 (m, 2 H, d), 7.02 (s, 1 H, e), 6.62–6.51 (m, 1 H, f), 5.60 (d, J = 5.1 Hz, 1 H, g), 4.39 (d, J = 6.8 Hz, 2 H, h), 4.26–4.16 (m, 1 H, i), 4.13–4.00 (m, 4 H, j, k), 3.94 (s, 3 H, l), 2.69–2.49 (m, 2 H, m), 2.25–2.06 (m, 2 H, n), 1.66 ppm (d, J = 5.9 Hz, 3 H, o).
LC-MS (ESI+/-): $[M+NH_4]^+$ calcd. 596.22 found 596.25; $[M+Na]^+$ calcd. 601.18 found 601.20; $[2M-H]^-$ calcd. 1155.37 found 1155.45.

4.4 Synthesis of photocleavable peptide CKFK-PCL-FQF

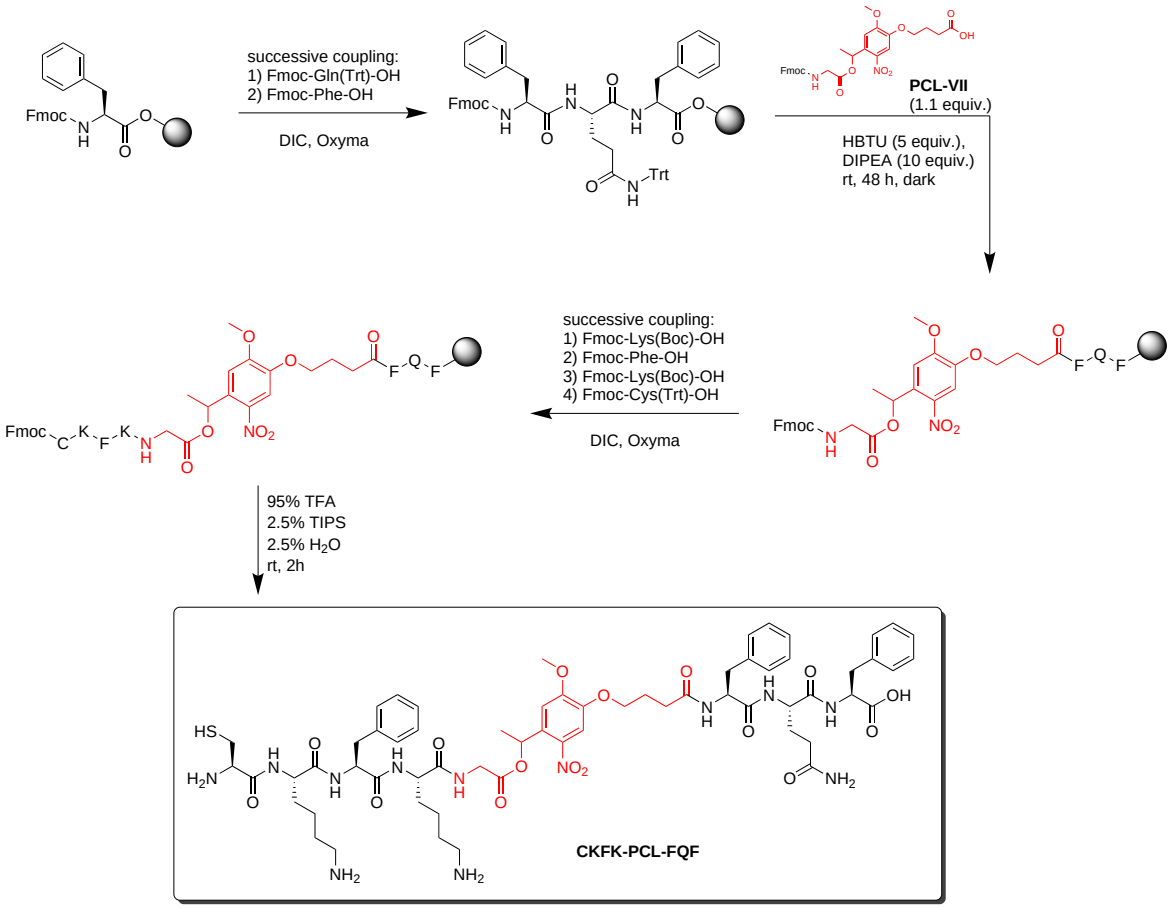

Scheme 6: Synthesis of photocleavable peptide CKFK-PCL-FQF

The synthesis was divided in three steps: (1) synthesis of FQF in automated SPPS; (2) coupling of **PCL-VII** to FQF-resin in a separate reaction vessel; (3) successive coupling of CKFK to PCL-FQF-resin in automated SPPS and subsequent cleavage from the resin.

After step 2 a Kaiser-Test was carried out according to manufacturer's instructions to assure complete coupling of **PCL-VII** to the peptide (using a Kaiser test kit by *Sigma Aldrich*). Cleavage from the resin in 0.1 mmol scale in step 3 was carried out in a 10 mL polypropylene syringe reaction vessel with 5 mL of cleavage solution after swelling the resin in DMF for 1 h.

HRMS (MALDI-TOF-MS, 1284.5849 g mol^{-1}): $[M+H]^+$ calcd. 1285.5922 found 1285.6202; $[M+Na]^+$ calcd. 1307.5741 found 1307.6017; $[M+K]^+$ calcd. 1323.5481 found 1323.5779; $[CKFKG+H]^+$ calcd. 582.3068 found 582.0468.

5 Summary

The CKFKFQF peptide – known for its formation of amyloid fibrils in aqueous solution among the group – was altered with a photolabile nitrobenzoyl linker with the aim to provide control over disassembly of fibrils. The photocleavable linker (PCL) was synthesised in 7 steps following a procedure by Sur *et al.* [31] and used in peptide synthesis to obtain photocleavable peptide CKFK-PCL-FQF. Kinetics of the cleavage on molecular scale were investigated *via* HPLC depending on irradiation time. The disassembly of preformed fibrils and the underlying β-sheet structure was investigated using ThT assays, CD, FTIR and NMR spectroscopy as well as TEM and AFM imaging. Suitability of the system for biological applications was tested with A549 cells regarding cell viability towards peptide, fibrils and fragments and attachment of cells to a fibril-coated surface depending on irradiation.

The findings showed that the rapid cleavage of the linker was not directly followed by fibril disassembly. Instead, structures stayed intact for 24 h before showing a morphology shift (48 h) and disassembly (72 h). Heating of irradiated samples promoted faster disassembly, while heating of non-irradiated samples previously incubated for 24 h in the dark showed increased fibril formation compared to samples only incubated for 24 h in the dark. Additionally, increased concentration was found to slow the disassembly rate rapidly.
Surfaces coated with the photocleavable peptide showed attachment and spreading of cells for non-irradiated slides. Irradiated slides did not show significant cellular attachment. No cellular toxicity was found for CKFK-PCL-FQF, its fibrils or the respective cleavage fragments.

References

[1] S. K. Maji, D. Schubert, C. Rivier, S. Lee, J. E. Rivier and R. Riek. 'Amyloid as a Depot for the Formulation of Long-Acting Drugs'. PLoS Biology, 6(2):e17, **2008**.

[2] F. Gelain, D. Bottai, A. Vescovi and S. Zhang. 'Designer Self-Assembling Peptide Nanofiber Scaffolds for Adult Mouse Neural Stem Cell 3-Dimensional Cultures'. PLoS ONE, 1(1):e119, **2006**.

[3] T. Scheibel, R. Parthasarathy, G. Sawicki, X.-M. Lin, H. Jaeger and S. L. Lindquist. 'Conducting nanowires built by controlled self-assembly of amyloid fibers and selective metal deposition'. Proceedings of the National Academy of Sciences, 100(8):4527–4532, **2003**.

[4] G. Whitesides, J. Mathias and C. Seto. 'Molecular self-assembly and nanochemistry: a chemical strategy for the synthesis of nanostructures'. Science, 254(5036):1312–1319, **1991**.

[5] F. Tantakitti, J. Boekhoven, X. Wang, R. V. Kazantsev, T. Yu, J. Li, E. Zhuang, R. Zandi, J. H. Ortony, C. J. Newcomb, L. C. Palmer, G. S. Shekhawat, M. O. de la Cruz, G. C. Schatz and S. I. Stupp. 'Energy landscapes and functions of supramolecular systems'. Nature Materials, 15(4):469–476, **2016**.

[6] R. J. Mart, R. D. Osborne, M. M. Stevens and R. V. Ulijn. 'Peptide-based stimuli-responsive biomaterials'. Soft Matter, 2(10):822, **2006**.

[7] D. L. Nelson and M. M. Cox. Lehninger Principles of Biochemistry. W. H. Freeman, New York, **2004**.

[8] S. Zhang. 'Emerging biological materials through molecular self-assembly'. Biotechnology Advances, 20(5-6):321–339, **2002**.

[9] R. Sarroukh, E. Goormaghtigh, J.-M. Ruysschaert and V. Raussens. 'ATR-FTIR: A "rejuvenated" tool to investigate amyloid proteins'. Biochimica et Biophysica Acta (BBA) - Biomembranes, 1828(10):2328–2338, **2013**.

[10] J. D. Sipe, M. D. Benson, J. N. Buxbaum, S. ichi Ikeda, G. Merlini, M. J. M. Saraiva and P. Westermark. 'Nomenclature 2014: Amyloid fibril proteins and clinical classification of the amyloidosis'. Amyloid, 21(4):221–224, **2014**.

[11] C. Yuan, W. Ji, R. Xing, J. Li, E. Gazit and X. Yan. 'Hierarchically oriented organization in supramolecular peptide crystals'. Nature Reviews Chemistry, 3(10):567–588, **2019**.

[12] C. Schilling, T. Mack, S. Lickfett, S. Sieste, F. S. Ruggeri, T. Sneideris, A. Dutta, T. Bereau, R. Naraghi, D. Sinske, T. P. J. Knowles, C. V. Synatschke, T. Weil and B. Knöll. 'Sequence-Optimized Peptide Nanofibers as Growth Stimulators for Regeneration of Peripheral Neurons'. Advanced Functional Materials, 29(24):1809 112, **2019**.

[13] R. Nelson, M. R. Sawaya, M. Balbirnie, A. Ø. Madsen, C. Riekel, R. Grothe and D. Eisenberg. 'Structure of the cross-β spine of amyloid-like fibrils'. Nature, 435(7043):773–778, **2005**.

[14] T. R. Jahn, O. S. Makin, K. L. Morris, K. E. Marshall, P. Tian, P. Sikorski and L. C. Serpell. 'The Common Architecture of Cross-β Amyloid'. Journal of Molecular Biology, 395(4):717–727, **2010**.

[15] R. Kodali and R. Wetzel. 'Polymorphism in the intermediates and products of amyloid assembly'. Current Opinion in Structural Biology, 17(1):48–57, **2007**.

[16] A. A. H. Zanjani, N. P. Reynolds, A. Zhang, T. Schilling, R. Mezzenga and J. T. Berryman. 'Amyloid Evolution: Antiparallel Replaced by Parallel'. Biophysical Journal, 118(10):2526–2536, **2020**.

[17] E. Cerf, R. Sarroukh, S. Tamamizu-Kato, L. Breydo, S. Derclaye, Y. F. Dufrêne, V. Narayanaswami, E. Goormaghtigh, J.-M. Ruysschaert and V. Raussens. 'Antiparallel β-sheet: a signature structure of the oligomeric amyloid β-peptide'. Biochemical Journal, 421(3):415–423, **2009**.

[18] M. Biancalana and S. Koide. 'Molecular mechanism of Thioflavin-T binding to amyloid fibrils'. Biochimica et Biophysica Acta (BBA) - Proteins and Proteomics, 1804(7):1405–1412, **2010**.

[19] C. Frantz, K. M. Stewart and V. M. Weaver. 'The extracellular matrix at a glance'. Journal of Cell Science, 123(24):4195–4200, **2010**.

[20] J. B. Matson and S. I. Stupp. 'Self-assembling peptide scaffolds for regenerative medicine'. Chem. Commun., 48(1):26–33, **2012**.

[21] M. Yolamanova, C. Meier, A. K. Shaytan, V. Vas, C. W. Bertoncini, F. Arnold, O. Zirafi, S. M. Usmani, J. A. Müller, D. Sauter, C. Goffinet, D. Palesch, P. Walther, N. R. Roan, H. Geiger, O. Lunov, T. Simmet, J. Bohne, H. Schrezenmeier, K. Schwarz, L. Ständker, W.-G. Forssmann, X. Salvatella, P. G. Khalatur, A. R. Khokhlov, T. P. J. Knowles, T. Weil, F. Kirchhoff and J. Münch. 'Peptide nanofibrils boost retroviral gene transfer and provide a rapid means for concentrating viruses'. Nature Nanotechnology, 8(2):130–136, **2013**.

[22] A. Chilkoti, M. R. Dreher and D. E. Meyer. 'Design of thermally responsive, recombinant polypeptide carriers for targeted drug delivery'. Advanced Drug Delivery Reviews, 54(8):1093–1111, **2002**.

[23] M. Pieszka, A. M. Sobota, J. Gačanin, T. Weil and D. Y. W. Ng. 'Orthogonally Stimulated Assembly/Disassembly of Depsipeptides by Rational Chemical Design'. ChemBioChem, 20(11):1376–1381, **2019**.

[24] S. C. Larnaudie, J. C. Brendel, K. A. Jolliffe and S. Perrier. 'pH-Responsive, Amphiphilic Core-Shell Supramolecular Polymer Brushes from Cyclic Peptide-Polymer Conjugates'. ACS Macro Letters, 6(12):1347–1351, **2017**.

[25] L. Zhang, Z. Wang, J. Das, M. Labib, S. Ahmed, E. H. Sargent and S. O. Kelley. 'Potential-Responsive Surfaces for Manipulation of Cell Adhesion, Release, and Differentiation'. Angewandte Chemie International Edition, 58(41):14 519–14 523, **2019**.

[26] S. J. Todd, D. Farrar, J. E. Gough and R. V. Ulijn. 'Enzyme-triggered cell attachment to hydrogel surfaces'. Soft Matter, 3(5):547, **2007**.

[27] T. T. Lee, J. R. García, J. I. Paez, A. Singh, E. A. Phelps, S. Weis, Z. Shafiq, A. Shekaran, A. del Campo and A. J. García. 'Light-triggered in vivo activation of adhesive peptides regulates cell adhesion, inflammation and vascularization of biomaterials'. Nature Materials, 14(3):352–360, **2014**.

[28] M. Clement, G. Daniel and M. Trelles. 'Optimising the design of a broad-band light source for the treatment of skin'. Journal of Cosmetic and Laser Therapy, 7(3-4):177–189, **2005**.

[29] A. Kaczmarek. 'Synthesis of a depsipeptide with photolabile protective group and fluorescence label', **2019**. Bachelor's thesis, Hochschule Fresenius, Idstein.

[30] K. Kaygisiz. Photogesteuerte Peptidmaterialien. Master's thesis, Johannes-Gutenberg-Universität, Mainz, **2019**.

[31] S. Sur, J. B. Matson, M. J. Webber, C. J. Newcomb and S. I. Stupp. 'Photodynamic Control of Bioactivity in a Nanofiber Matrix'. ACS Nano, 6(12):10 776–10 785, **2012**.

[32] C. G. Bochet. 'Photolabile protecting groups and linkers'. Journal of the Chemical Society, Perkin Transactions 1, (2):125–142, **2001**.

[33] P. Wang. 'Photolabile Protecting Groups: Structure and Reactivity'. Asian Journal of Organic Chemistry, 2(6):452–464, **2013**.

[34] A. Barth, J. E. T. Corrie, M. J. Gradwell, Y. Maeda, W. Mäntele, T. Meier and D. R. Trentham. 'Time-Resolved Infrared Spectroscopy of Intermediates and Products from Photolysis of 1-(2-Nitrophenyl)ethyl Phosphates: Reaction of the 2-Nitrosoacetophenone Byproduct with Thiols'. Journal of the American Chemical Society, 119(18):4149–4159, **1997**.

[35] H. LeVine. 'Thioflavine T interaction with amyloid β-sheet structures'. Amyloid, 2(1):1–6, **1995**.

[36] V. I. Stsiapura, A. A. Maskevich, V. A. Kuzmitsky, K. K. Turoverov and I. M. Kuznetsova. 'Computational Study of Thioflavin T Torsional Relaxation in the Excited State'. The Journal of Physical Chemistry A, 111(22):4829–4835, **2007**.

[37] M. Ilanchelian and R. Ramaraj. 'Emission of thioflavin T and its control in the presence of DNA'. Journal of Photochemistry and Photobiology A: Chemistry, 162(1):129–137, **2004**.

[38] M. Krebs, E. Bromley and A. Donald. 'The binding of thioflavin-T to amyloid fibrils: localisation and implications'. Journal of Structural Biology, 149(1):30–37, **2005**.

[39] C. Wu, Z. Wang, H. Lei, Y. Duan, M. T. Bowers and J.-E. Shea. 'The Binding of Thioflavin T and Its Neutral Analog BTA-1 to Protofibrils of the Alzheimer's Disease Aβ16–22 Peptide Probed by Molecular Dynamics Simulations'. Journal of Molecular Biology, 384(3):718–729, **2008**.

[40] S. M. Kelly, T. J. Jess and N. C. Price. 'How to study proteins by circular dichroism'. Biochimica et Biophysica Acta (BBA) - Proteins and Proteomics, 1751(2):119–139, **2005**.

[41] B. C. Smith. Fundamentals of Fourier Transform Infrared Spectroscopy. Taylor & Francis Ltd., **2011**. URL https://www.ebook.de/de/product/21176818/brian_c_smith_fundamentals_of_fourier_transform_infrared_spectroscopy.html.

[42] F. S. Parker. Applications of Infrared Spectroscopy in Biochemistry, Biology, and Medicine. Springer US, **1971**.

[43] G. Zandomeneghi, M. R. Krebs, M. G. McCammon and M. Fändrich. 'FTIR reveals structural differences between native β-sheet proteins and amyloid fibrils'. Protein Science, 13(12):3314–3321, **2009**.

[44] S. Krimm and Y. Abe. 'Intermolecular Interaction Effects in the Amide I Vibrations of Polypeptides'. Proceedings of the National Academy of Sciences, 69(10):2788–2792, **1972**.

[45] C. B. C. David B. Williams. Transmission Electron Microscopy. Springer-Verlag New York Inc., **2009**. URL https://www.ebook.de/de/product/7130081/david_b_williams_c_barry_carter_transmission_electron_microscopy.html.

[46] N. Marturi. Vision and visual servoing for nanomanipulation and nanocharacterization in scanning electron microscope. Ph.D. thesis, Université de Franche-Comté, **2013**.

[47] B. Voigtländer. Atomic Force Microscopy. Springer-Verlag GmbH, **2019**. URL https://www.ebook.de/de/product/37055102/bert_voigtlaender_atomic_force_microscopy.html.

[48] Z. Papanyan and S. Markarian. 'Detection of Oxidation of L-Cysteine by Dimethyl Sulfoxide in Aqueous Solutions by IR Spectroscopy'. Journal of Applied Spectroscopy, 80(5):775–778, **2013**.

[49] A. L. Cloe, J. P. R. O. Orgel, J. R. Sachleben, R. Tycko and S. C. Meredith. 'The Japanese Mutant Aβ (ΔE22-Aβ1–39) Forms Fibrils Instantaneously, with Low-Thioflavin T Fluorescence: Seeding of Wild-Type Aβ1–40 into Atypical Fibrils by ΔE22-Aβ1–39'. Biochemistry, 50(12):2026–2039, **2011**. URL https://doi.org/10.1021/bi1016217. PMID: 21291268.

[50] A. Aggeli, I. A. Nyrkova, M. Bell, R. Harding, L. Carrick, T. C. B. McLeish, A. N. Semenov and N. Boden. 'Hierarchical self-assembly of chiral rod-like molecules as a model for peptide -sheet tapes, ribbons, fibrils, and fibers'. Proceedings of the National Academy of Sciences, 98(21):11 857–11 862, **2001**.

[51] M. V. Maslova, L. G. Gerasimova and W. Forsling. 'Surface Properties of Cleaved Mica'. Colloid Journal, 66(3):322–328, **2004**.

Appendix

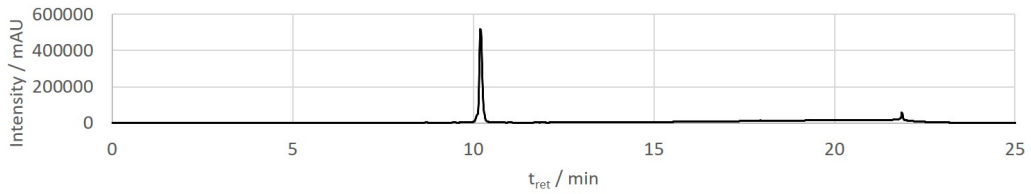

Figure A.1: Raw data of t_0 sample from HPLC kinetic study

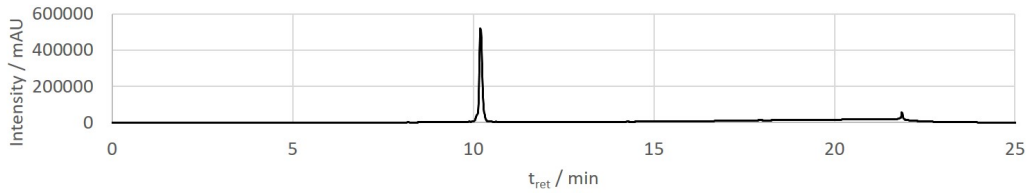

Figure A.2: Raw data of t_{UV}=15 s sample from HPLC kinetic study

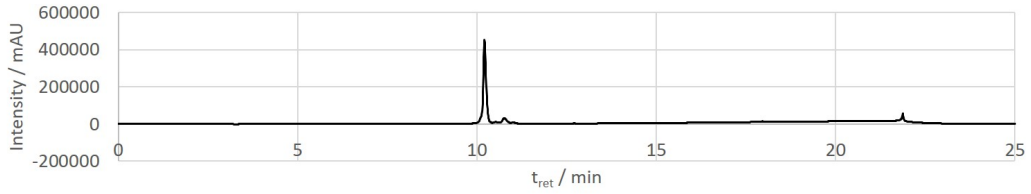

Figure A.3: Raw data of t_{UV}=30 s sample from HPLC kinetic study

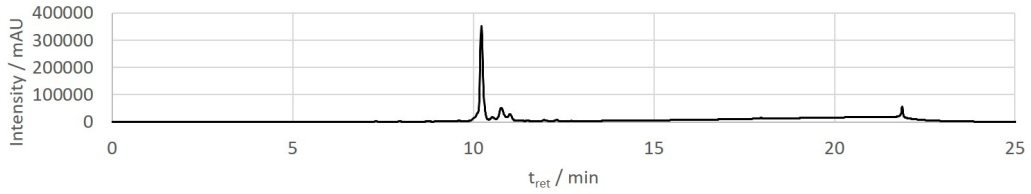

Figure A.4: Raw data of t_{UV}=60 s sample from HPLC kinetic study

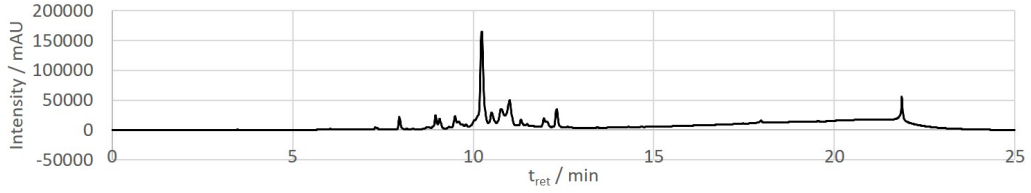

Figure A.5: Raw data of t_{UV}=5 min sample from HPLC kinetic study

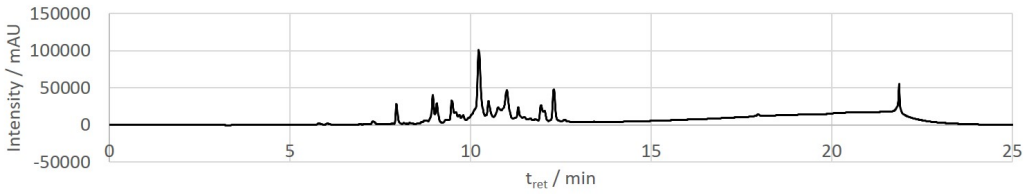

Figure A.6: Raw data of t_{UV}=6 min sample from HPLC kinetic study

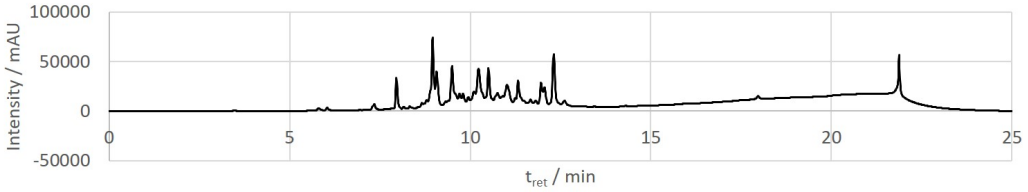

Figure A.7: Raw data of t_{UV}=10 min sample from HPLC kinetic study

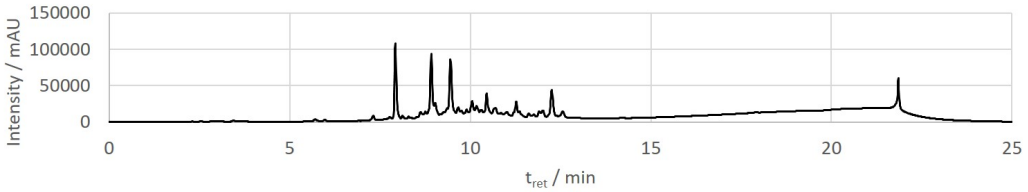

Figure A.8: Raw data of t_{UV}=20 min sample from HPLC kinetic study

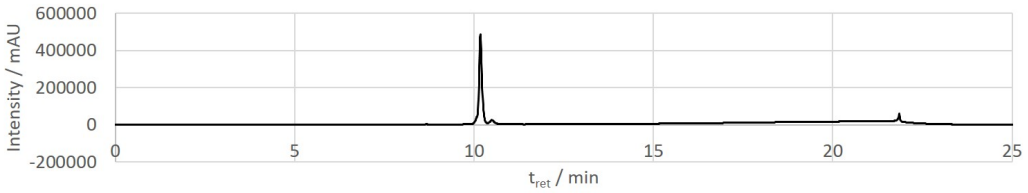

Figure A.9: Raw data of sample incubated for 72 h without UV irradiation from HPLC kinetic study

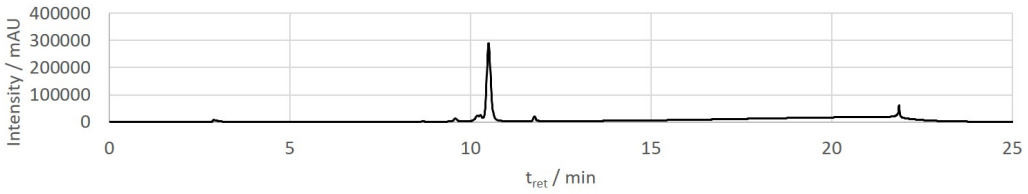

Figure A.10: Raw data of sample incubated for 96 h with 10 % DMSO without UV irradiation from HPLC kinetic study

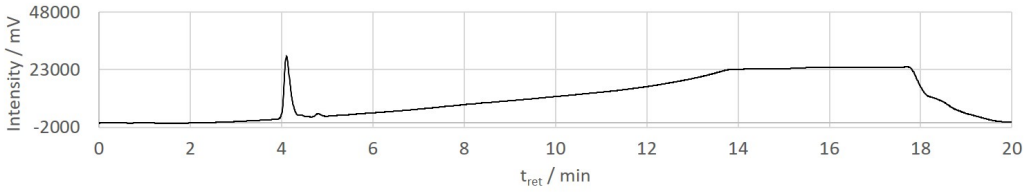

Figure A.11: Raw data of t_0 sample from LCMS kinetic study

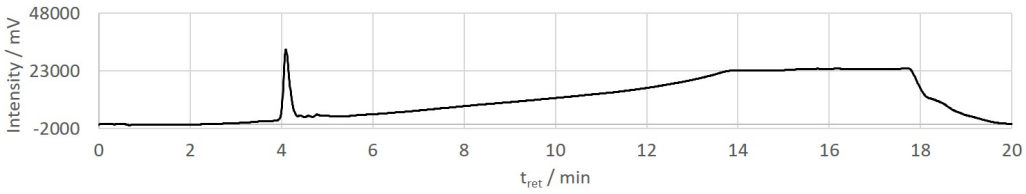

Figure A.12: Raw data of t_{UV}=15 s sample from LCMS kinetic study

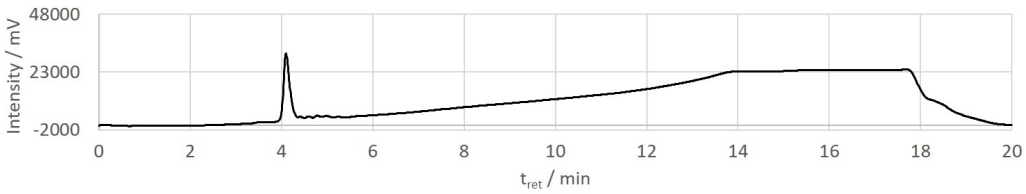

Figure A.13: Raw data of t_{UV}=30 s sample from LCMS kinetic study

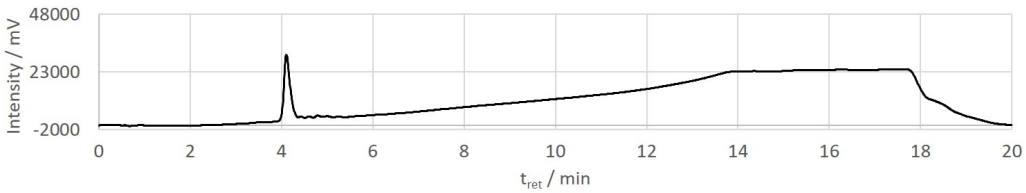

Figure A.14: Raw data of t_{UV}=60 s sample from LCMS kinetic study

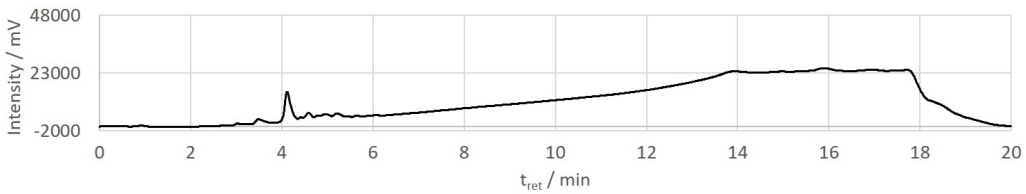

Figure A.15: Raw data of t_{UV}=5 min sample from LCMS kinetic study

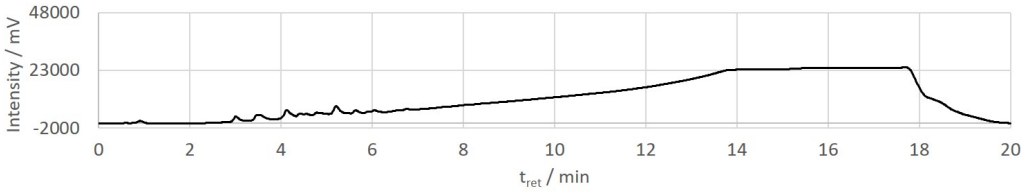

Figure A.16: Raw data of t_{UV}=6 min sample from LCMS kinetic study

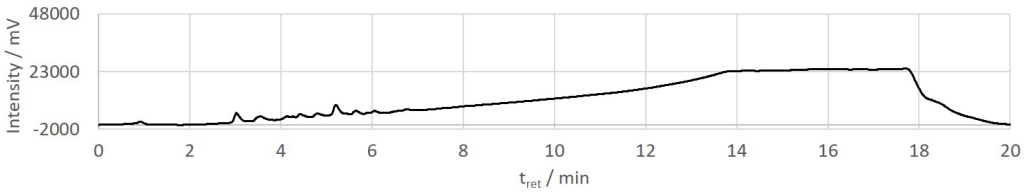

Figure A.17: Raw data of t_{UV}=10 min sample from LCMS kinetic study

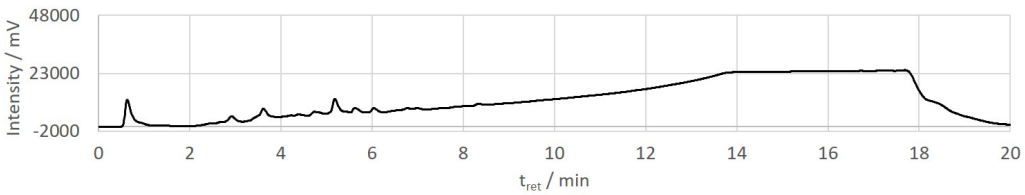

Figure A.18: Raw data of t_{UV}=20 min sample from LCMS kinetic study

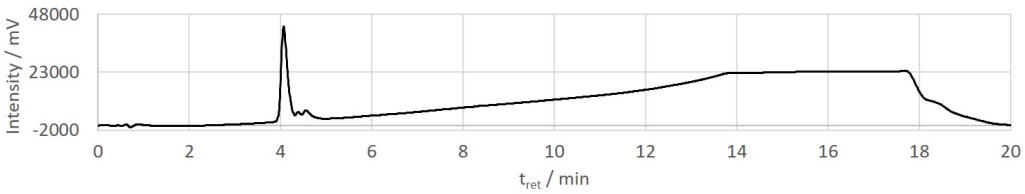

Figure A.19: Raw data of sample incubated for 72 h without UV irradiation from LCMS kinetic study

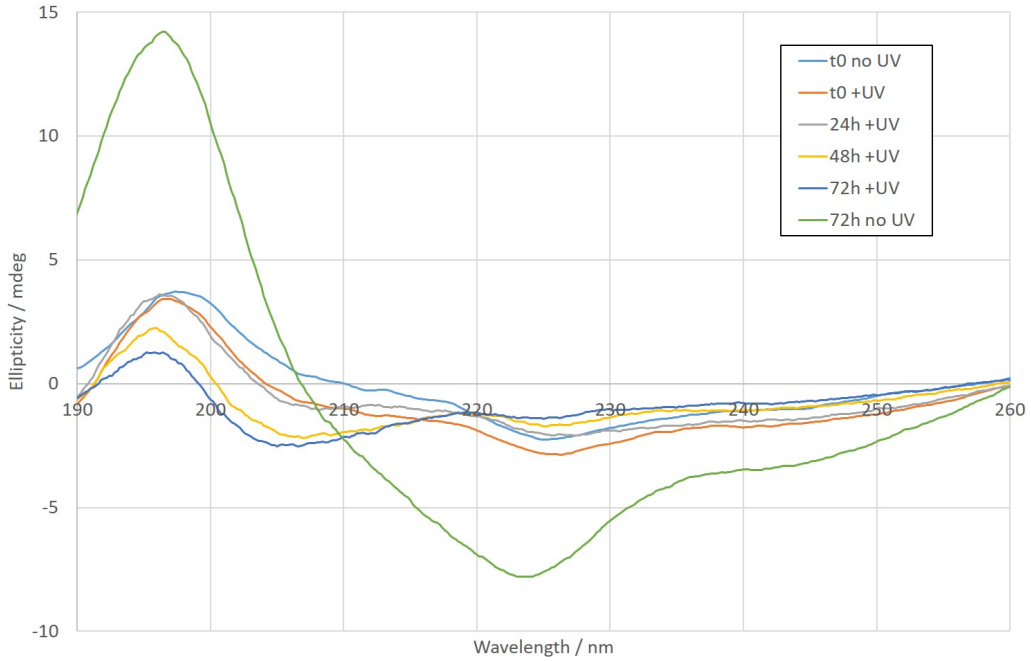

Figure A.20: Raw data of CD spectroscopy measurements of CKFK-PCL-FQF

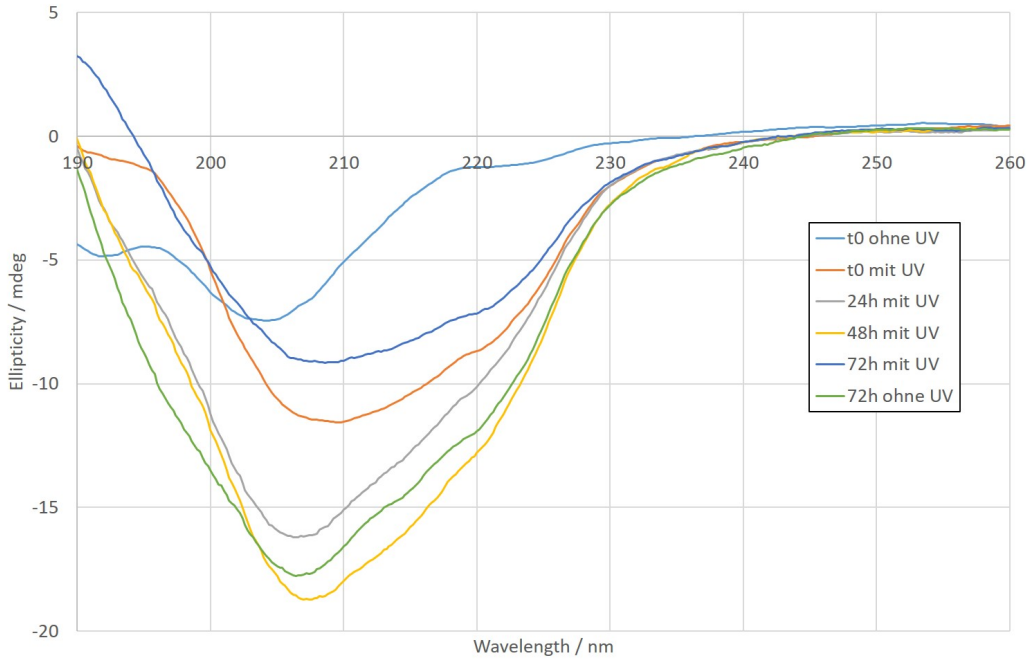

Figure A.21: Raw data of CD spectroscopy measurements of CKFKFQF

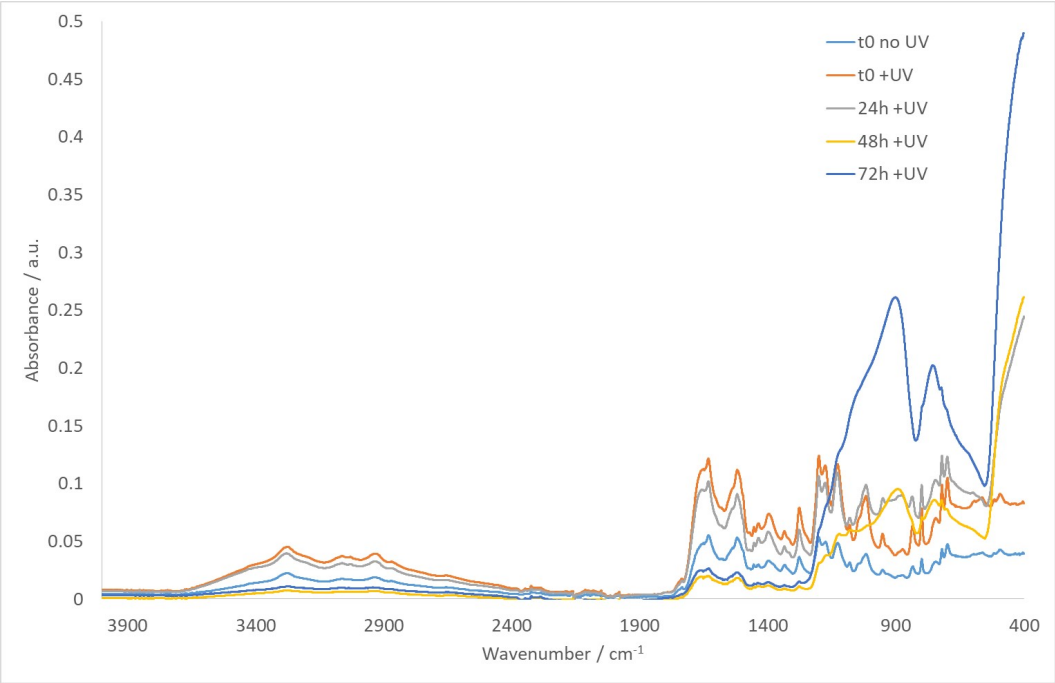

Figure A.22: Raw data of FTIR spectroscopy measurements of CKFK-PCL-FQF

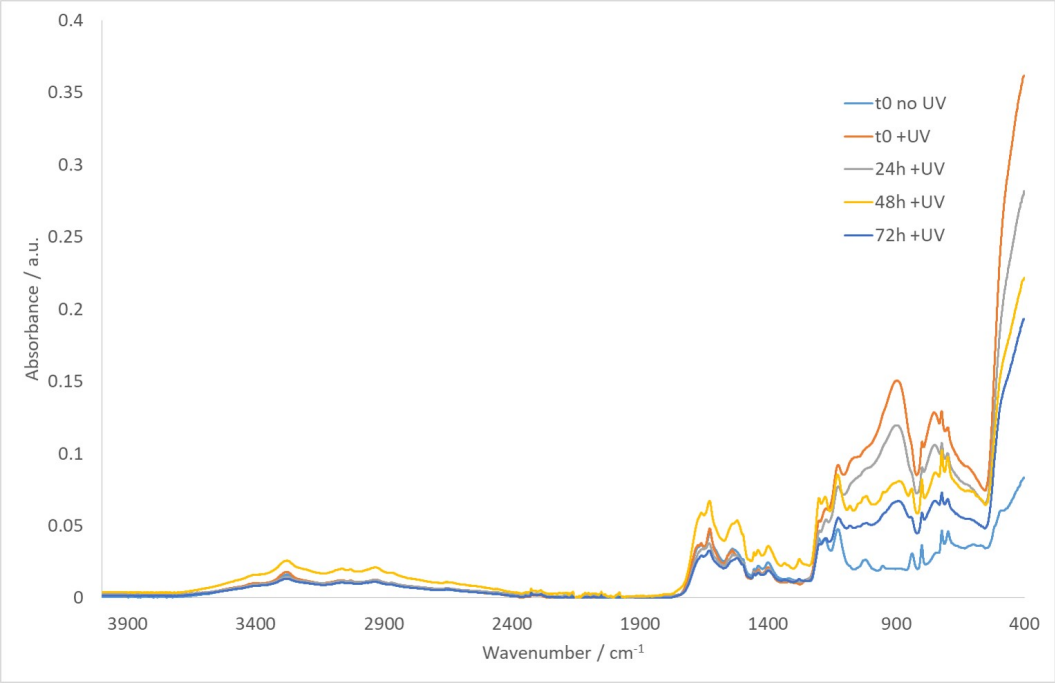

Figure A.23: Raw data of FTIR spectroscopy measurements of CKFKFQF

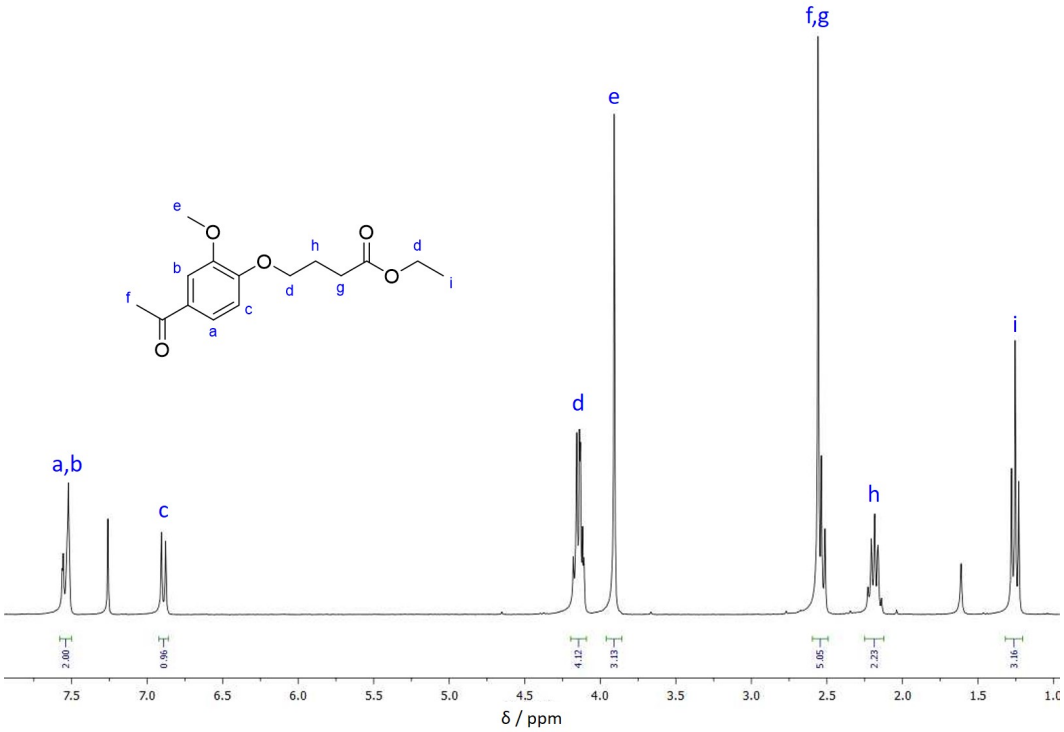

Figure A.24: ^{1}H-NMR of **PCL-I** (300 MHz, $CDCl_3$): δ [ppm] 7.59–7.48 (m, 2 H, a, b), 6.89 (d, J = 8.2 Hz, 1 H, c), 4.15 (td, J = 6.7 Hz,5.0 Hz, 4 H, d), 3.91 (s, 3 H, e), 2.59–2.48 (m, 5 H, f, g), 2.26–2.11 (m, 2 H, h), 1.25 (t, J = 7.1 Hz, 3 H, i).

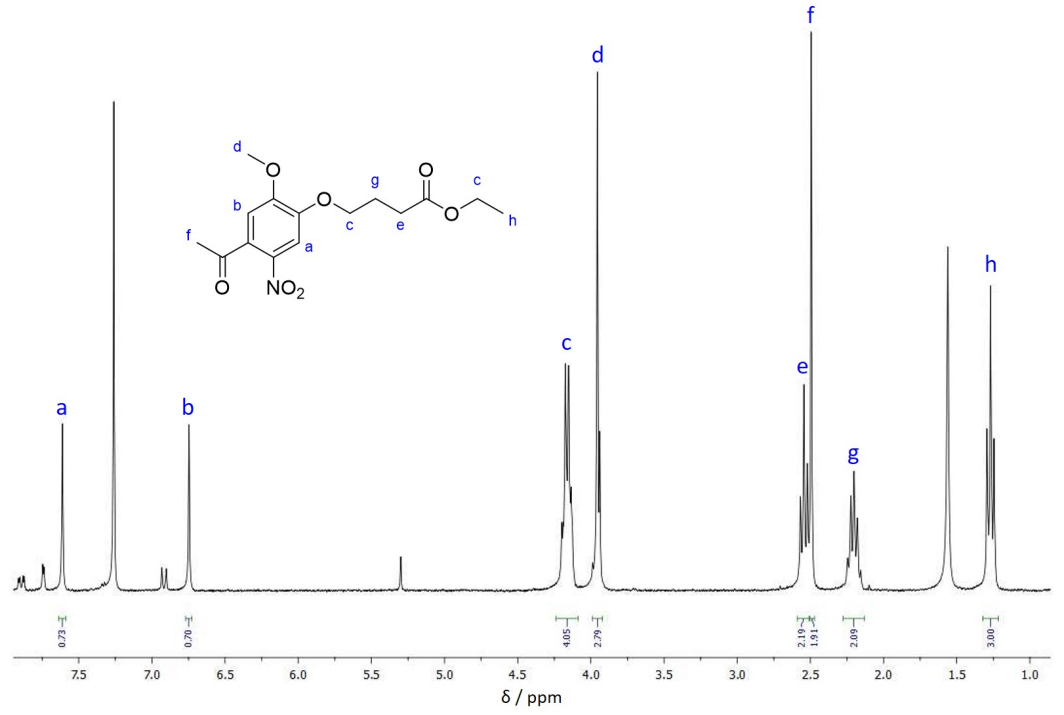

Figure A.25: ^{1}H-NMR of **PCL-II** (300 MHz, $CDCl_3$): δ [ppm] 7.61 (s, 1 H, a), 6.75 (s, 1 H, b), 4.25–4.07 (m, 4 H, c), 3.96 (s, 3 H, d), 2.54 (t, J = 7.2 Hz, 2 H, e), 2.49 (s, 3 H, f), 2.26–2.14 (m, 2 H, g), 1.27 (t, J = 7.1 Hz, 3 H, h).

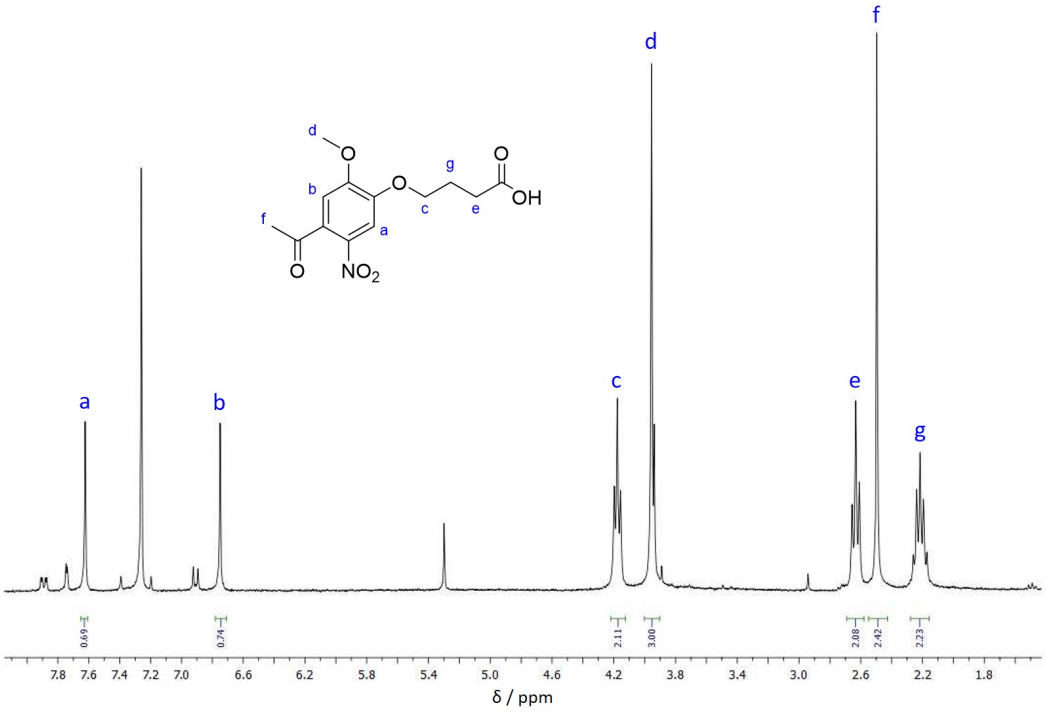

Figure A.26: ^{1}H-NMR of **PCL-III** (300 MHz, $CDCl_3$): δ [ppm] 7.62 (s, 1 H, a), 6.75 (s, 1 H, b), 4.18 (t, J = 6.1 Hz, 2 H, c), 3.96 (s, 3 H, d), 2.63 (t, 2 H, e), 2.50 (s, 3 H, f), 2.28–2.15 (m, 2 H, g).

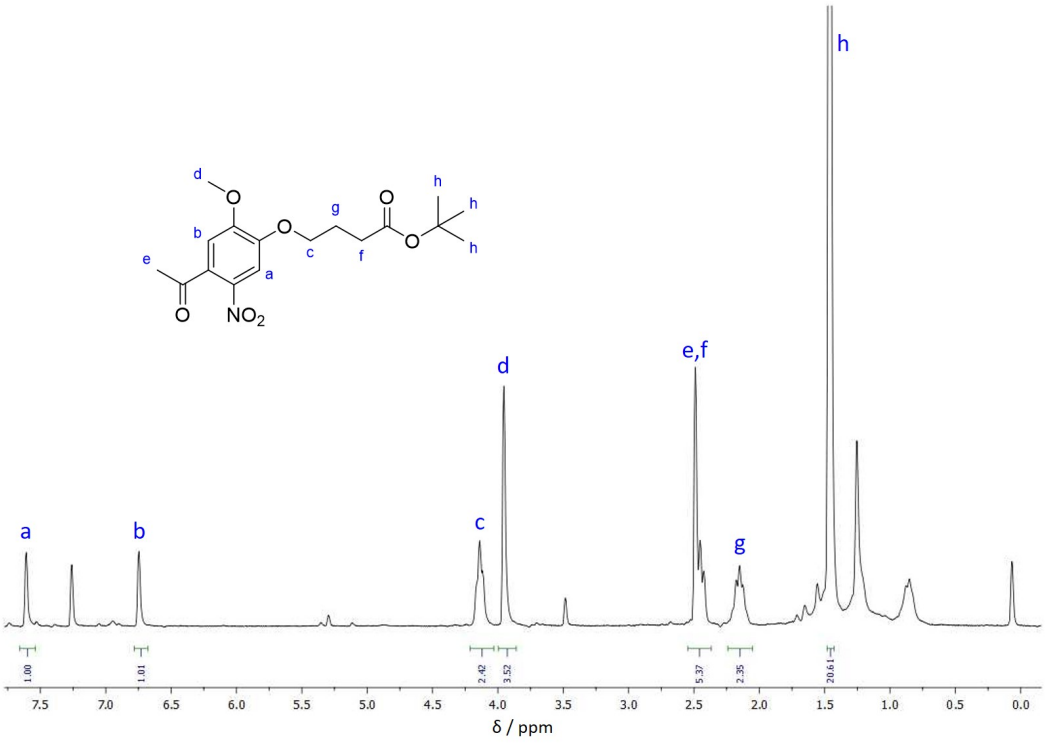

Figure A.27: ^{1}H-NMR of **PCL-IV** (250 MHz, $CDCl_3$): δ [ppm] 7.61 (s, 1 H, a), 6.75 (s, 1 H, b), 4.19–4.04 (m, 2 H, c), 3.95 (s, 3 H, d), 2.53–2.40 (m, 5 H, e, f), 2.21–2.07 (m, 2 H, g), 1.46 (s, 9 H, h).

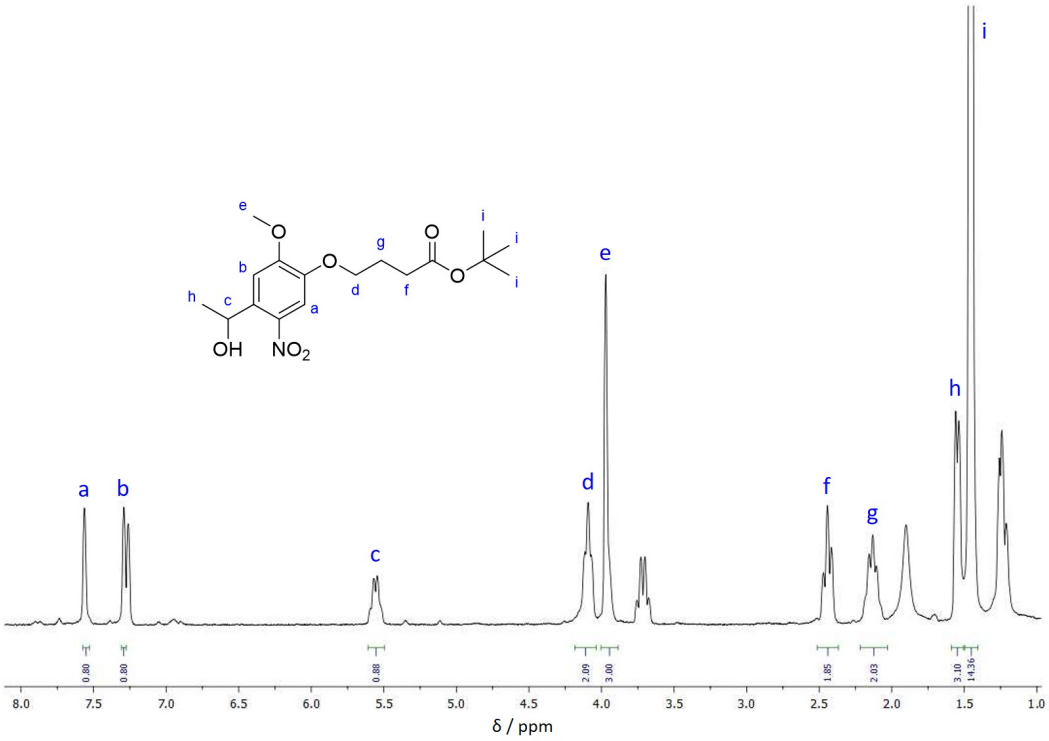

Figure A.28: ^{1}H-NMR of **PCL-V** (250 MHz, $CDCl_3$): δ [ppm] 7.56 (s, 1 H, a), 7.29 (s, 1 H, b), 5.61–5.49 (m, 1 H, c), 4.09 (t, J = 5.0 Hz, 2 H, d), 3.97 (s, 3 H, e), 2.44 (t, J = 6.8 Hz, 2 H,f), 2.21–2.03 (m, 2 H, g) 1.55 (d, J = 5.4 Hz, 3 H, h) 1.46 (s, 9 H, i).

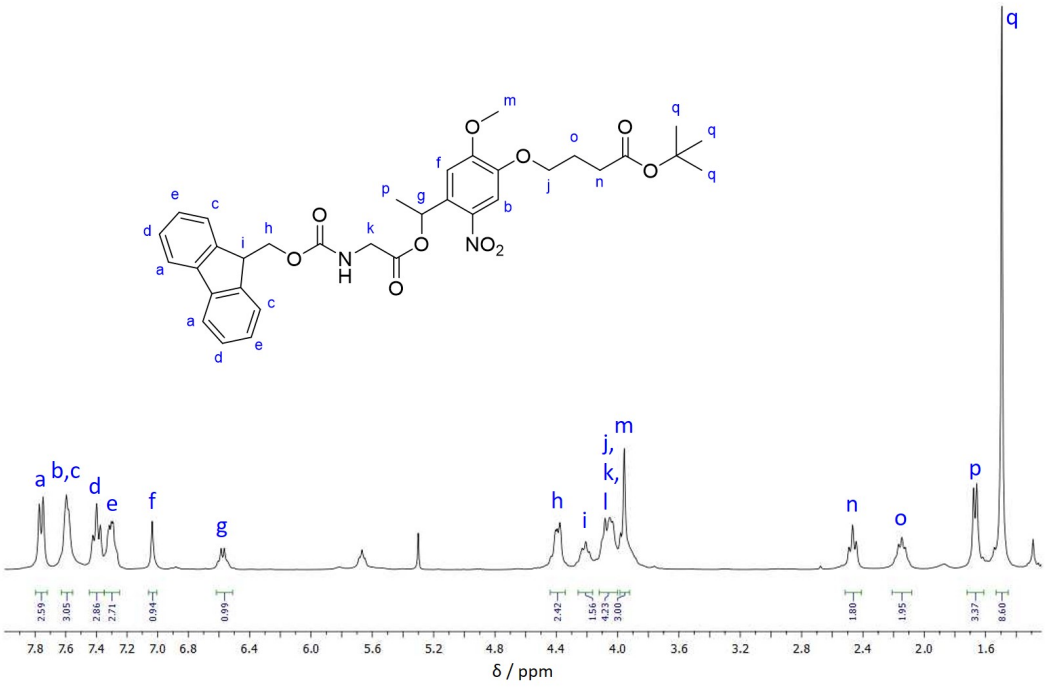

Figure A.29: ^{1}H-NMR of **PCL-VI** (300 MHz, $CDCl_3$): δ [ppm] 7.76 (d, J = 7.4 Hz, 2 H, a) 7.64–7.54 (m, 3 H, b, c), 7.38 (dd, J = 15.9, 8.6 Hz, 2 H, d), 7.35–7.24 (m, 2 H, e), 7.04 (s, 1 H, f), 6.58 (dd, J = 12.1, 5.8 Hz, 1 H, g), 4.46–4.31 (m, 2 H, h), 4.26–4.16 (m, 1 H, i), 4.12–4.00 (m, 4 H, j, k, l), 3.96 (s, 3 H, m), 2.47 (t, J = 7.1 Hz, 2 H, n), 2.20–2.09 (m, 2 H, o), 1.67 (d, J = 6.2 Hz, 3 H, p) 1.49 (s, 9 H, q).

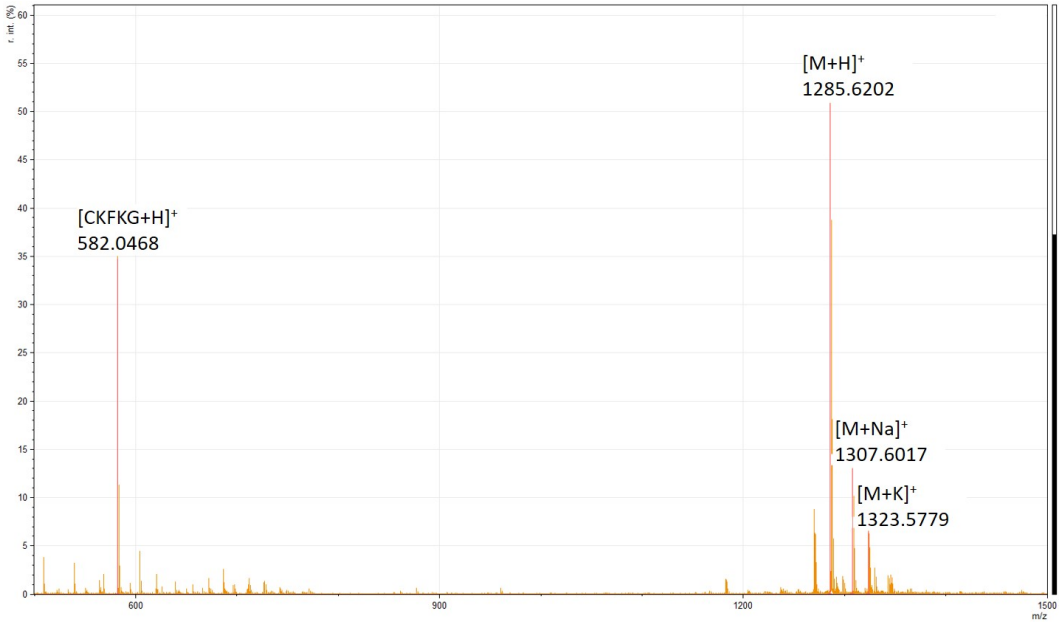

Figure A.30: MALDI-TOF-MS spectrum of CKFK-PCL-FQF (exact mass: 1284.5848 g mol^{-1}) after purification on preparative HPLC

Affirmation in lieu of an oath

I hereby affirm that the thesis entitled: *Triggered Disassembly of Peptide Nanofibers in Solution and on Surfaces* is my own work, written independently and without assistance other than the resources cited.

I have indicated the bodies of work, including tables and illustrations, which originate from earlier work of other authors. In each case I have quoted the origin thereof.

This thesis has not been submitted, in either identical or similar form, to any other examination authority or university, and has not yet been published.

I did not invent nor falsify the data presented in this thesis. The data have been acquired by myself or were made available for this analysis from reliable sources as indicated. I am obliged to give the 1st reviewer access to all original data until the examination procedure is completed.

Idstein, August 18, 2020